Dual effects of microglia on blood brain barrier permeability induced by systemic inflammation

Haruwaka, Koichiro

Doctor of Philosophy

Department of Physiological Sciences
School of Life Science
The Graduate University for Advanced Studies,
SOKENDAI

Index

Summary

Microglia are the sole immune cells that reside in the central nervous system in embryonic stage. Microglia are activated in neurological diseases such as multiple sclerosis, Alzheimer's disease, and epilepsy, and are involved in the pathology by releasing neurotrophic factors and cytokines that act on neurons, glia and blood vessels. Production of inflammatory cytokines from activated microglia increases blood-brain barrier (BBB) permeability and may promote immune cell infiltration and brain inflammation. On the other hand, in autoimmune diseases such as systemic lupus erythematosus (SLE) and severe infections are known to increased BBB permeability, activated microglia and associate with psychiatric symptoms such as cognitive impairment, anxiety and depression. However, it is not clear how the activation of the immune system in these diseases acts on microglia and causes abnormalities in the central nervous system. Therefore, the purpose of this study was clarifying how microglia reacts to systemic inflammation separated by BBB and how it affects the change in permeability of BBB.

I observed the response of microglia to systemic inflammation using MRL/lpr mice, known as autoimmune model mice, and LPS-treated mice in which inflammation was induced by intraperitoneal injection of lipopolysaccharide (LPS). *In vivo* imaging using a two-photon microscope revealed that microglia migrated and accumulated around the cerebral blood vessels with systemic inflammation. Chemokine signal inhibition by chemokine receptor inhibitors revealed that CCL5-CCR5 signal pathway plays a crucial role in the migration of microglia to the vessels. Visualization of BBB permeability by intravenous administration of fluorescent dextran tracer revealed that the contact between microglia and vessels plays an important role in BBB permeability changes. It was found that daily injection of LPS promoted the leakage of the 10-kDa fluorescein dextran into the brain parenchyma. It was also found that microglial accumulation around blood vessels occurred before permeability changes. In addition, transgenic mice that can induce microglia-specific expression of diphtheria toxin by the withdrawal of doxycycline were used to evaluate BBB permeability during microglia ablation. Microglia ablation increased leakage in the early phases of systemic inflammation, and conversely suppressed leakage during prolonged inflammation. These results suggest that microglia protect leakage at the early phase of inflammation and worsen leakage during chronic inflammation. To clarify the details of microglia functions, microglia were

isolated and collected from MRL/lpr mice, and gene expression was comprehensively analyzed. As a result, I found increased expression of phagocytosis-related genes and tight junction genes. The observation of microglia and vessels in MRL/lpr mice with an electron microscope revealed that microglial processes expressing tight junction molecule CLDN5 were in direct contact with vascular endothelial cells. Furthermore, immunostaining the formalin-fixed brain slices of mice with daily LPS injection showed that CLDN5 was transiently expressed during early phases of inflammation and that the expression of CD68, a phagocytic marker, increased during prolonged inflammation. In addition, it was found that AQP4, which is a constituent molecule of BBB, was included into the microglia phagocytic vesicles. This result suggests that microglia are involved in the failure of the BBB structure by phagocytosing astrocyte end-feet. Moreover, it was found that leakage during prolonged inflammation was significantly suppressed by administering minocycline that inhibits microglia activation.

In conclusion, I found that microglia have two functions for BBB integrity. One is the BBB protective effect of early systemic inflammation, and the other is the BBB injury effect during chronic systemic inflammation. During the early phases of systemic inflammation, microglia expressed CLDN5 and accumulated around the vessels to suppress the increased BBB permeability. In contrast, microglia became a phagocytic phenotype in prolonged inflammation, and they disrupt BBB structure by phagocytosing the astrocyte end-feet. In addition, the CCL5-CCR5 pathway was identified as an important signal for migration of microglia to the vessels and BBB protection during early phases of inflammation. From the results of this study, vessel-associated microglia are expected as a therapeutic target for central nervous system symptoms caused by systemic inflammation.

Introduction

Microglia: immune cells in central nervous system

Microglia are resident immune cells in central nervous system (CNS). In 1919, Pio del Rio-Hortega firstly reported microglia morphology. Microglia observed by reticulin silver impregnation have highly branched processes in the adult brain, and they are distributed evenly in the brain (Kettenmann, et al., Physiol. Rev., 2011). They transform into an amoeba-like form at the damaged tissue, and these cells were thought to have the ability to migrate and phagocytose. In 1930, Isaac Costero first reported the cultivation of human-derived microglia. Later, *in vitro* cell culture methods were improved, and the method of separating microglia by shaking from a co-culture system derived from rat or mouse neonatal have been used in microglia research (Giulian and Baker, J. Neurosci., 1986). Furthermore, research on microglia have been developed by the production of an antibody against ionized calcium-binding adapter molecule 1 (IBA1, also called AIF1) which is a macrophage-specific marker (Imai, et al., Biochem. Biophys. Res. Commun., 1996). The origin of microglia, the sole immune cell in the central nervous system, has been debated. Several studies proposed that macrophages and monocytes infiltrate into the brain and differentiate into microglia (Perry, et al., Neuroscience, 1985; Raivich and Banati, Brain Res. Brain Res. Rev., 2004; Guillemin and Brew, J. Leukoc. Biol., 2004). On the other hand, several studies proposed that microglia were derived from the ectoderm same as other glial cells such as astrocytes and oligodendrocytes (Fujita and Kitamura, Acta Neuropathol. Suppl., 1975; Ginhoux, et al., Front. Cell. Neurosci., 2013). Recent observations using the Iba1-EGFP mouse revealed that the yolk sac express EGFP, and microglia were mesodermal cells derived from the yolk sac (Chan, et al., Brain Res Rev, 2007). In addition, specific cell labeling using runt-related transcription factor 1 (Runx1), which is specifically expressed in the embryonic yolk sac, revealed that microglia enter in the brain from the yolk sac via blood vessels at early embryonic stage (Ginhoux, et al., Science, 2010). This suggests that microglia have a different origin from neurons and astrocytes. The transcription factor Myb has been considered essential for the development of all bone marrow hematopoietic stem cell-derived macrophages and monocytes, but it is not necessary for the development of yolk sac-derived macrophages (Schulz, et al., Science, 2012). It became clear that myeloid-derived macrophages and yolk sac-derived macrophages were can be distinguished. Some tissue-resident macrophages with embryonic origins can renew itself, while bone

marrow-derived monocytes are thought to be able to infiltrate each organ and replace with tissue-resident macrophages in adulthood (Zhao, et al., J. Cell. Physiol., 2018). However, debate has continued regarding whether circulatory macrophage can differentiate into microglia in the brain. Bone marrow-derived cells transferred to irradiated mice have been reported to have engrafted (Krall, et al., Blood, 1994). Macrophages labeled with a retrovirus-introduced gene were transferred from the vein to the mouse, and after 3-4 months, the percentage of brain microglia was examined. As a result, 20% of the total microglia were replaced with donor-derived cells. Contrary to this, it has been reported by experimental autoimmune encephalomyelitis (EAE) and parabiosis in Cx3cr1-GFP mice that infiltrating macrophages do not engraft as microglia. These experiments concluded that monocytes do not differentiate into resident microglia because monocytes infiltrate the spinal cord and then disappear with the end of inflammation (Ajami, et al., Nat. Neurosci., 2011). It has been reported that microglia begin to grow rapidly within 2-3 days after temporarily microglia ablation using by an inhibitor against the colony stimulating factor receptor (CSF1R), and the cell density is restored (Elmore, et al., Neuron, 2014). In addition, there are cells called perivascular macrophages (PVM) around the cerebral blood vessels, and it has been reported by transplantation experiments that their origin is myeloid cells Kennedy and Abkowitz, Blood, 1997; Thomas, Brain Res. Brain Res. Rev., 1999; Ransohoff and Cardona, Nature, 2010; Prinz and Priller, Nat. Rev. Neurosci., 2014). However, recent fate-mapping studies have pointed out that PVM may originate from yolk sac the same as microglia (Goldmann et al., Nat. Immunol., 2016), and the discussion continues (Faraco, et al., J. Mol. Med. (Berl.), 2017).

Microglial functions and morphology

Microglia in the healthy brain exist in a ramified form in which small cell bodies and branched processes (also called “resting microglia”). Activated microglia, accumulated at damaged tissue due to neurodegenerative diseases, multiple sclerosis, cerebral infarction and trauma, show macrophage-like morphology without branches with enhanced migration and phagocytic ability (also called “amoeboid microglia”) (Kettenmann, et al., Physiol. Rev., 2011). The analysis of the physiological functions of microglia has developed dramatically in recent years. Recent advances in microscopic techniques and the establishment of mice with genetically labeled microglia-specific fluorescent markers have revealed the active movement of ramified microglia by imaging.

Transgenic mice expressing green fluorescent protein (EGFP) downstream of the promoter region of Iba1 gene (Hirasawa, et al., J. Neurosci. Res., 2005) or knock-in mice which are inserted EGFP into the region of Cx3cr1 gene (Jung, et al., Mol. Cell. Biol., 2000) have been used for *in vivo* observation of microglia. As a result of *in vivo* imaging using a two-photon microscope, it was revealed that the ramified microglia, which was regarded as resting microglia, rapidly moved their processes even under healthy conditions (Nimmerjahn, et al., Science, 2005). It has reported that laser injury induces microglial process accumulation at the damaged site depending on P2Y receptors and extracellular adenosine triphosphate (ATP) (Davalos, et al., Nat. Neurosci., 2005). Furthermore, the movement of microglial processes is related to the synapse maintenance. It has been shown by simultaneously observing synapse and microglia that microglial processes are directly contact with synapses in static period (Wake, et al., J. Neurosci., 2009). In the ischemic area, the duration of microglia-synapse contacts was prolonged, and then synapse removal occurred. Direct contact between microglial processes and synapses was confirmed by electron microscopic image analysis, which was in contact with both presynaptic and postsynaptic junctions (Wake, et al., J. Neurosci., 2009; Tremblay, et al., PLoS Biol., 2010). Synapses are the connections between neurons and play an important role in information transmission. Meanwhile they are formed excessively during development, and only important synapses remain, depending on neural activity. Neural circuits are constructed not only by forming synapses, but also by removing synapses with low activity. Microglia involve in both synapse formation and removal. It has been reported that microglia contact with the dendrites of neurons at the early stage of development. Filopodia, the spine precursor, was formed at those contact sites (Miyamoto, et al., Nat Commun, 2016). In addition, genetic ablation of microglia during development showed a decrease in the number of spines and the frequency of miniature excitatory postsynaptic current (mEPSC) in pyramidal cells of the cerebral cortex 2/3 layer. These results suggest that microglia play an important role in the formation of functional spines. On the other hand, it has been reported that knockout of CX3CR1, a chemokine receptor expressed in microglia, suppresses synapse removal (Paolicelli, et al., Science, 2011). Other studies have also shown that the synapses are eliminated by microglia via the complement system, including C1q and C3a (Schafer, et al., Neuron, 2012). The removal of synapses by microglia has been verified by analysis using a stimulated emission depletion (STED) microscope, a super-resolution microscope.

The presence of postsynaptic density protein 95 (PSD95), one of the major postsynaptic scaffolding proteins, in microglial phagosome suggests that synapses have been removed by phagocytosis (Paolicelli, et al., Science, 2011). Thus, it was revealed that microglia play an important role in brain function. In addition to surveillance of environmental changes, microglia are also actively involved in the formation of neural circuits through the movement of processes and phagocytosis even though resting microglia. Gene expression profile of microglia is similar to that of macrophages (Guillemin and Brew, J. Leukoc. Biol., 2004). It is known that microglia express molecules common to macrophage: surface antigen markers such as integrin CD11b and F4/80; pattern recognize receptor such as Toll-like receptors (TLRs) (Lehnardt, Glia, 2010; Fiebich, et al., Front. Cell. Neurosci., 2018); lysosomal marker CD68; chemokine receptor such as CX3CR1 and CCR5; and major histocompatibility complex class II (MHC class II) (Aloisi, Glia, 2001). The CD11b, CX3CR1 and CD68 are characteristic molecules expressed specifically in microglia in the brain. Although there are functional similarities of gene expression pattern and high phagocytic ability between macrophages and microglia, differences of gene expression have been found in recent comprehensive analysis (Bennett, et al., Proc. Natl. Acad. Sci. U. S. A., 2016; Zeisel, et al., Science, 2015; Butovsky, et al., Nat. Neurosci., 2014). Microglia-specific genes that are not expressed on monocytes and macrophages have been discovered, such as Tmem119 (Bennett, et al., Proc. Natl. Acad. Sci. U. S. A., 2016) and Sall1 Buttgereit, et al., Nat. Immunol., 2016). In addition, among the resident microglia, it has been shown that gene expression varies depending on the brain region and the phases of development (Ayata, et al., Nat. Neurosci., 2018; De Biase, et al., Neuron, 2017; Li, et al., Neuron, 2019). Thus, much attention has been focused on diversity and function of microglia.

CNS diseases and microglia

Microglia recognize tissue damage and pathogen invasion and they are activated through P2Y receptor and pattern recognition receptor signals (Gulke, et al., Ther. Adv. Neurol. Disord., 2018; Barichello, et al., Mol. Neurobiol., 2016). Activated microglia are known not only to phagocytose pathogens, but also to act both protectively and toxically on neurons by producing neurotrophic factors and cytokines (Kim and de Vellis, J. Neurosci. Res., 2005). Alzheimer's disease is known to be associated with accumulation of amyloid beta (Aβ). It has been reported that microglia are

neuroprotective by phagocytosis of Aβ and activated by amyloid precursor protein, and acts neuropathically by the production of IL-1β (Barger and Harmon, Nature, 1997; Akiyama, Neurobiol. Aging, 2000). In Parkinson's disease, active microglia are known to accumulate around the substantia nigra dopaminergic neurons (McGeer, et al., Neurology, 1988; Lecours, et al., Front. Cell. Neurosci., 2018). It has been pointed out that inflammatory cytokines due to aging and chronic stress activate microglia and are involved in the onset and progression of pathology. Active microglia are also observed in the lesions of multiple sclerosis, and it is known that the cell death of oligodendrocytes that form myelin sheath is induced by the production of nitric oxide (NO) and cytokines from activated microglia (Jack, et al., J. Neurosci. Res., 2005). Microglia also interact with cerebral blood vessels. During ischemia, microglia are involved in angiogenesis by producing vascular endothelial growth factor (VEGF) and insulin-like growth factor-1, IGF-1 (Xie, et al., Vasc Cell, 2013; Lalancette-Hebert, et al., J. Neurosci., 2007), and reported to be toxic by the production of inflammatory cytokines (Lambertsen, et al., J. Cereb. Blood Flow Metab., 2012; Patel, et al., Int. J. Physiol. Pathophysiol. Pharmacol., 2013). However, there are many unclear points how it is involved in the maintenance and control of the blood-brain barrier (BBB), which separates the circulatory system from the central nervous system (Zhao, et al., Dev. Neurobiol., 2018).

Blood-brain barrier (BBB) and microglia

BBB plays an important role in maintaining homeostasis of the brain environment through the selective permeability of molecules. BBB restricts the movement of molecules into and out of the brain parenchyma and selectively transporting substances. BBB consists of tight junctions between endothelial cells, basement membranes surrounding vessels, transporters and receptors (Zlokovic, Neuron, 2008). The function of the BBB is regulated and maintained by the interaction between the cells surrounding the vessels, and the entire system including the basement membrane and those cells is also called a neurovascular unit (NVU) (Iadecola, Nat. Rev. Neurosci., 2004; Hawkins and Davis, Pharmacol. Rev., 2005). Therefore, BBB dysfunction occurs when gene expression and structural changes in BBB constituent cells are caused by inflammation (Banks, et al., J. Neuroinflammation, 2015). As the basic structure of BBB, endothelial cells express molecules such as Claudin5, Occludin, and Zonula occludens-1 (ZO-1) to form tight junctions between cells to prevent paracellular diffusion of water-

soluble substances. Tight junctions play a central role in BBB function (Abbott, et al., Neurobiol. Dis., 2010). In the astrocytes, a part of their processes forms an end-feet that surrounds the vessels, and the water molecule channel Aquaporin4 (AQP4) and the potassium channel Kir4.1 are locally located on the vessel side of the end-feet. (Higashi, et al., Am. J. Physiol. Cell Physiol., 2001). Astrocyte end-feet have been reported to cover vessels without any gaps and provide a physical barrier that prevents free diffusion of water-soluble molecules (Mathiisen, et al., Glia, 2010). On the other hand, it has recently reported that there are gaps between the end-feet. Electron microscopic analysis shows that the end-feet do not completely cover the vessels (Korogod, et al., Elife, 2015). This analysis uses an improved method of sample preparation by freezing rather than conventional chemical fixation. In either case, the end-feet structure is a necessary component of the BBB. The structure of BBB is maintained by the expression of connexin molecules Cx43 and Cx30 that connect the end-feet, and lack of these results in loss of the polarity of the end-feet and increased permeability (Ezan, et al., J. Cereb. Blood Flow Metab., 2012). In addition, it has been reported by imaging with sliced brain and fluorescent tracers that astrocyte end-feet actually prevent the diffusion of molecules (Nuriya, et al., Cereb. Cortex, 2013). Furthermore, a study using experimental autoimmune encephalomyelitis (EAE) has shown that astrocytes activated by IL-1β act protectively on BBB by expressing tight junction-related molecules CLDN1 and CLDN4 (Horng, et al., J. Clin. Invest., 2017). Pericytes are present in the basement membrane so as to cover endothelial cells. Pericytes increase the expression of tight junction-related molecules in endothelial cells through the production of transforming growth factor-β (TGF β) and glial derived neurotrophic factor (GDNF). Pericytes have also been reported to contribute to the maintenance of the BBB structure by inducing the polarity of the astrocyte end-feet (Dohgu, et al., Brain Res., 2005; Armulik, et al., Nature, 2010). It was found that differentiation is inhibited by deficiency of PDGFRβ, a specific marker of pericyte (Lindahl, et al., Science, 1997). Analysis of BBB permeability and expressed molecules in this knock-out mouse revealed that pericytes play an important role in BBB formation in the developmental stage (Daneman, et al., Nature, 2010). In addition, there is an inverse correlation between pericyte-coverage of vessels and BBB permeability, and the pericyte ablation triggers increased BBB permeability, cerebral blood flow decreases and neuronal cell death (Nikolakopoulou, et al., Nat. Neurosci., 2019). On the other hand, microglia have been studied by focusing on the interaction with the vessels during

pathological conditions by animal models such as Alzheimer's disease and stroke. After direct administration of Aβ or induction of ischemia, activated microglia have been reported to be toxic to the BBB by phagocytosis and production of interleukin-1β (IL-1β), tumor necrosis factor-α (TNFα) and NO (Lambertsen, et al., J. Cereb. Blood Flow Metab., 2012; Ryu and McLarnon, Exp. Neurol., 2006). It has also been reported that angiogenesis after ischemia acts protectively by the production of VEGF (Xie, et al., Vasc Cell, 2013). Furthermore, when the vessels are experimentally injured by laser, microglia accumulate processes at the injured site depending on the ATP signal via P2RY12 and suppress leakage (Lou, et al., Proc. Natl. Acad. Sci. U. S. A., 2016). However, the detailed mechanism of BBB control by direct contact between microglia and the vessels has not been clarified.

BBB dysfunction and neuropsychiatric disorders

The BBB failures have been reported in neurological and psychiatric disorders, and the progression of disease states from BBB impairments has been extensively studied. Decreased expression of tight junction molecules in endothelial cells reduces barrier function, and enhanced vascular permeability causes leakage of plasma components into the brain parenchyma. Furthermore, if the breakdown of the BBB structure progresses, infiltration of immune cells into the brain parenchyma occurs, causing neuronal cell death and abnormalities in neural circuit activity, leading to central nervous system disease (Hanisch and Kettenmann, Nat. Neurosci., 2007). In multiple sclerosis, IL-1β produced by activated microglia induces a decrease in BBB function, allowing monocytes and T cells to infiltrate the brain parenchyma, causing an immune response to the myelin sheath, and demyelination (Wang, et al., PLoS One, 2014). In Alzheimer's-type cognitive impairment, increased vascular permeability in the hippocampus has been reported from studies using magnetic resonance imaging (MRI) (Montagne, et al., Neuron, 2015). In addition, microglia are activated around the damaged vessels, suggesting that increased permeability of injured vessels is involved in disease progression (Giannoni, et al., Neurobiol. Dis., 2016). In Parkinson's disease, increased permeability in the midbrain has been found by detection of radioisotope tracers using positron emission tomography (PET) (Kortekaas, et al., Ann. Neurol., 2005). It has also been reported that activated microglia highly expressing lysosomal marker CD68 accumulate at the lesion site of stroke, and damage the vessels by phagocytosis of the vessel component and production

of inflammatory cytokines (Jolivel, et al., Acta Neuropathol., 2015). Thus, abnormalities of BBB and central nervous system diseases are closely related, and it has been suggested that negative control of BBB by activated microglia plays an important role behind it.

Relation between BBB and systemic inflammation

Inflammation originating outside the brain, such as sepsis and autoimmune disease, also causes BBB dysfunction and microglial activation. An increase in BBB permeability in white matter of type 2 diabetic patients has been reported in studies using MRI (Starr, et al., J. Neurol. Neurosurg. Psychiatry, 2003). In chronic periodontitis, it has been reported that IL-1β and IL-6 produced in the immune response to the causative bacteria act on vascular endothelial cells to increase permeability (Dumitrescu, Front. Psychol., 2016). In severe infections, TNFα, IL-1β, IL-6, and NO are known to reduce the expression of tight junction-related molecules in endothelial cells, leading to reduced BBB function (Banks, et al., J. Neuroinflammation, 2015; Danielski, et al., Mol. Neurobiol., 2018). Furthermore, it is known that BBB function is also reduced in systemic lupus erythematosus (SLE), which is an autoimmune disease. Autoantibodies such as anti-N-methyl-d-aspartate (NMDA) receptor antibody and anti-deoxyribonucleic acid (DNA) antibody have been detected in patients' cerebrospinal fluid (Stojanovich, et al., Autoimmun Rev, 2007). SLE is one of the autoimmune diseases with systemic inflammation and multi-organ damage. It is characterized by producing autoantibodies (Dema and Charles, Antibodies (Basel), 2016), butterfly rash, arthritis, nephritis and vascular disorders (Kaul, et al., Nat Rev Dis Primers, 2016). SLE can be associated with central nervous system symptoms, including convulsions, meningitis, psychiatric symptoms such as anxiety and depression, and cognitive impairment. The prevalence of such symptoms is about half of all SLE patients (Popescu and Kao, Curr. Neuropharmacol., 2011; Ainiala, et al., Neurology, 2001). BBB breakdown and microglial activation are suspected to causes of central nervous system symptoms. In SLE model mice, it has been reported that leaked autoantibodies and interferon-α (IFNα) activate microglia and cause synapse and dendrite reduction (Bialas, et al., Nature, 2017; Nestor, et al., J. Exp. Med., 2018). However, there are many unclear points regarding the mechanism by which systemic inflammation causes BBB functional breakdown and the process by which microglia are activated.

In this study, I examined how microglia are involved in BBB permeability in

order to understand changes in BBB caused by inflammation from outside the vessel. To clarify the interaction between BBB and microglia, two types of mouse model were used for validation: MRL/lpr mice, as a SLE model mice, and lipopolysaccaride (LPS)-injected mice as a model of systemic inflammation induced by intraperitoneal injection of LPS. I daily observed the changes in BBB permeability and contact between microglia and the vessels by *in vivo* imaging using a two-photon microscope. Here, I report that microglia interact with blood vessels with systemic inflammation and are involved in both BBB protection and increased permeability depending on the phases of inflammation.

Material and Methods

Strains and animal care

Experimental protocols were approved by the Animal Care and Use Committees of Kobe University Graduate School of Medicine and the National Institutes of Natural Sciences. Experiments were conducted according to the guidelines of the National Institutes of Health *Guide for the Care and Use of Laboratory Animals*. I used male mice for all experiments to avoid potential variations during estrus cycles. All of the animals in this study were given free access to food and water and housed under 12 h light/dark cycle conditions. I used ICR (WT) mice and MRL/MpJJmsSlc-lpr/lpr (MRL/lpr) mice as a model of autoimmune disorders, such as systemic lupus erythematosus and Sjogren's syndrome, which were purchased from Japan SLC (Shizuoka, Japan). To visualize the morphology and motility of microglia, I used Cx3cr1-EGFP transgenic mice expressing enhanced green fluorescent protein (EGFP) controlled by of Cx3cr1 promoter which is specific for microglia, macrophages and monocytes (Jung, et al., Mol. Cell. Biol., 2000). I then backcrossed Cx3cr1-EGFP mice onto MRL/lpr mice for more than six generations to generate MRL/lpr::Cx3cr1-EGFP mice, which developed lymphadenopathy and splenomegaly at the age of 9 weeks. To further visualize the resident microglia, I used Sall1 reporter mice (Sall1-GFP) (Buttgereit, et al., Nat. Immunol., 2016). For microglia ablation experiments, I crossed Iba1-tetracycline transactivator (Iba1-tTA) mice (Tanaka, et al., Cell Rep, 2012) with tetracycline operator-diphtheria toxin A (tetO-DTA) mice (Stanger, et al., Nature, 2007). All transgenic mice were derived from the C57BL/6J strain.

Surgery

I performed the first surgery in 6-8-week-old mice. Following anesthesia with ketamine (74 mg/kg, *i.p.*) and xylazine (10 mg/kg, *i.p.*) the skull was exposed and cleaned, and a custom-made head plate was firmly attached to the skull with dental cement (G-CEM ONE; GC, Tokyo, Japan). This head plate allowed us to securely attach the mouse to a stainless frame for two-photon imaging in the awake state or perform the circular craniotomy. One or two days after plate attachment, I performed a circular craniotomy (2 mm diameter) over the left primary motor cortex (M1, centered at 1 mm lateral from the bregma) under isoflurane (1%) anesthesia as previously described (Masamizu, et al., Nat. Neurosci., 2014). After the craniotomy, 2% (w/v) agarose L dissolved (Nippon Gene, Tokyo, Japan) in saline was applied, and a glass window comprising two coverslips (2 &

4 mm each; Matsunami Glass, Osaka, Japan) were placed over the brain surface with ultraviolet curable adhesive (NOR-61, Norland). The edges of the cranial window were sealed with a combination of dental cement and dental adhesive resin cement (Super Bond; Sun Medical, Shiga, Japan). Mice were housed individually and imaging experiments started around 3 weeks after the surgical treatments (i.e., 9-11-week old).

Two-photon imaging

Two-photon images were acquired from the left M1 using a laser scanning system (LSM 7 MP system; Carl Zeiss, Oberkochen, Germany) with two types of water-immersion objective lenses (10×, numerical aperture (N.A.) 0.5; 20×, N.A. 1.0; Carl Zeiss) and a Ti:sapphire laser (Mai Tai HP; Spectra-Physics, Santa Clara, CA) operating at a 950-nm wavelength. Fluorescence was separated by a 570-nm dichroic mirror with 495-550 nm (green channel: for EGFP fluorescence detection) and 570-630 nm (red channel: for Texas Red fluorescence detection) emission filters and collected using GaAsP photomultiplier tubes (Hamamatsu Photonics, Shizuoka, Japan). To assess blood-brain barrier permeability, I used a laser scanning system (NIS-Elements; Nikon Instech Co., Ltd., Tokyo, Japan) with a water-immersion objective lens (25×, N.A. 1.10; Nikon Instech Co., Ltd.) and a mode-locked Ti:sapphire Chameleon Ultra II laser (Coherent, Santa Clara, CA) set at 950-nm. Fluorescence was separated with two dichroic mirrors (560-nm dichroic mirror with 500-550 nm [green channel: for fluorescein fluorescence detection] and 563-588 nm [red channel: for Tetramethylrhodamine (TMR) fluorescence detection] emission filters; 593-nm dichroic mirror with 601-657 nm [magenta channel: for Texas Red fluorescence detection] emission filters).

In vivo quantification of blood-brain barrier permeability

Cerebral blood vessels were visualized using dextran-conjugated fluorophores. To estimate disruption of the blood-brain barrier (BBB) caused by systemic inflammation (see below), I injected fluorescence-tagged dextrans into the tail vein during imaging. Three different dextran beads of increasing size: 10 kDa Dextran-Texas Red, 40 kDa Dextran-tetramethylrhodamine (TMR), and 70 kDa Dextran-fluorescein (all at concentrations of 2 mg/ml, Thermo Fisher Scientific, Waltham, MA). None of these dextrans would cross an intact BBB so the presence of fluorescence in the brain parenchyma in response to a dextran injection indicated BBB disruption. To quantify the

degree of disruption, I reconstructed 23 stacks of individual Z-plane images acquired after each dextran injection with each focal plane separated by 2 μm where each frame was a resolution of 1024 × 1024 pixels. The borders of the vessels in the Z-stacks were mapped out using the "Maximum Entropy Threshold" function in ImageJ (National Institutes of Health, Bethesda, MD). This was combined with the "Analyze Particles" function to delineate the vessel borders (using settings of size = 40-Infinity (μm^2), and "Include holes"). This allowed quantification of the mean fluorescence intensity outside the defined vessels. These values were expressed relative to WT in the original Z-projected image. Figure 2 schematically illustrates the approach to quantify BBB leak.

Systemic drug administration

Lipopolysaccharide (LPS; Funakoshi, Tokyo, Japan) was administered to induce systemic inflammation. Single daily injections of LPS (1.0 mg/kg, *i.p.*) were repeated for 7 days after two-photon imaging under control conditions (7 consecutive days before LPS injections). Control mice received *i.p.* saline injections under the same dosing schedule. To produce a milder LPS model, I also prepared a single LPS injection model (1.0 mg/kg, *i.p.*, one shot throughout the experiment).

The Iba1-tTA::tetO-DTA mice were reared with chow containing Dox 100 mg/kg. Withdrawal of the doxycycline (Dox-Off) in the feed induced selective expression of the diphtheria toxin A (DTA) in microglia, resulting in cell death. The Dox-containing chow was replaced by Dox-free standard chow 7 days before starting two-photon imaging during the consecutive 7-day LPS injections.

Minocycline hydrochloride (Mino; M9511-1G, Sigma-Aldrich, St. Louis, MO) was administered to inhibit microglial activation. Single daily injections of Mino (75 mg/kg, *i.p.*) were started 3 days prior to LPS injections and continued for 10 consecutive days. Control mice received *i.p.* vehicle (5% Dimethyl sulfoxide in saline) injections under the same LPS dosing schedule. I also created mice that had received the 10-day Mino injections but not the LPS injections.

Systemic interferon-alpha (IFNα) was also injected to trigger the release of CCL5, which could regulate microglial motility. A 1 x 10^5 IU dose of recombinant mouse IFNα (12100-1, R&D systems, Minneapolis, MN) dissolved in 100 μl of sterile saline was intravenously injected.

Intraparenchymal drug injection

To identify what triggers expression of CLDN5 and CD68 in microglia (Also see the main text), I injected intraparenchymal IFNα. Under isoflurane (1%) anesthesia, a glass pipette (GDC-1, Narishige, Tokyo, Japan) was stereotaxically inserted into the left primary motor cortex. A 600 IU dose of recombinant mouse IFNα (12100-1, R&D system) dissolved in 600 nl of sterile saline was injected. As the control, 600 nl of sterile saline was injected in the right primary motor cortex.

Intraventricular drug injection

To identify which factor attracted microglia to blood vessels, I performed daily intraventricular injections of an inhibitor of the most likely signaling molecule. For the intraventricular injection, I implanted a combination of guide (CXG-8; Eicom, Kyoto, Japan) and dummy cannula (CXD-8; Eicom) in the right lateral ventricle after creating the glass window. D-Ala-peptide T-amide (DAPTA; R&D systems), a selective antagonist for CCL5 receptor CCR5 (Rosi, et al., Neuroscience, 2005; Di Prisco, et al., J. Neurochem., 2012) was injected into the ventricle through an injection canula (CXMI-8; Eicom) attached to an electrically-driven injection pump (UMP3; WPI, Sarasota, FL). Single daily injections of DAPTA (1μl; 0.4 μg/μl in saline) were started 3 days prior to LPS injections and continued for 7 consecutive days.

Immunohistochemistry

Animals were deeply anesthetized with ketamine and xylazine, and transcardially perfused with 4% paraformaldehyde solution in PBS. Fixed brains were extracted from the skull and post-fixed overnight in the same solution followed by 30% sucrose. The brains were microtomed (Leica Microsystems, Wetzlar, Germany) into 30 μm slices. After blocking and permeabilization for 1 hour in 5% bovine serum albumin (BSA) and 0.5% Triton X-100 in PBS, the slices were incubated at 4°C overnight with primary antibodies diluted in PBS. After PBS wash, slices were subsequently incubated with secondary antibodies in PBS at room temperature (RT) for 3 hours. Slices were then mounted on glass slides in Fluoromount-G (Southern Biotech, Birmingham, AL). Fixed tissue was imaged using a Zeiss LSM510 Meta confocal microscope (Carl Zeiss) with a 20× objective (NA 1.0; Carl Zeiss) or a 63× oil-immersion objective (NA 1.4). The following antibodies were used for staining: anti-IBA1 (019-19741, Wako, Osaka, Japan;

ab5076, Abcam, London, UK; 1:400), anti-AQP4 (AB3594, Merck KGaA, Darmstadt, Germany; 1:500), anti-CLDN5 (35-2500, Thermo Fisher Scientific; 1:100), anti-CD68 (MCA1957GA, Bio-Rad, Hercules, CA; 1:400), anti-PDGFRβ (14-1402-82, Thermo Fisher Scientific; 1:100), anti-TMEM119 (400-011, Synaptic Systems, Göttingen, Germany; 1:100), anti-CD31 (14-0311-81, Thermo Fisher Scientific; 1:100), anti-GFAP (AB53554-100, Abcam; 1:400), anti-Fibrin (A0080, DAKO, Santa Clara, CA, 1:250), anti-rabbit Alexa 488, anti-rabbit Alexa 594, anti-goat Alexa 488, anti-goat Alexa 594, anti-mouse Alexa 594, anti-rat Alexa 555 (Molecular Probes, Eugene, OR; 1:500 for each), anti-mouse Alexa 405 and anti-rat Alexa 405 (Abcam; 1:500 for each). To visualize the cerebral vasculature, the brain slices were incubated with DyLight 488 labeled Lycopersicon esculentum lectin (DL1174, Vector laboratories, Burlingame, CA, USA; 1:200) at RT for 1 hour (Nikolakopoulou, et al., PLoS One, 2017).

Image analysis

Images were analyzed using ImageJ (National Institutes of Health) and MATLAB (MathWorks, Natick, MA) software packages. Movies and 3D images were corrected for focal plane displacement using ImageJ plug-in TurboReg and StackReg (Thevenaz, et al., IEEE Trans Image Process, 1998). Microglia in the superficial layer of the motor cortex (100-200 μm from the pia, corresponding to layer II/III) were analyzed in Z-projected images (confocal image: 1024×321 pixels, 0.312 μm/pixel, 2 μm Z-step [rostrocaudal direction], 10 slices, Maximum Intensity projection; two-photon image: 1024×1024 pixels, 0.254 μm/pixel, 2 μm Z-step [dorsoventral direction], 50 slices). The imaging depth was determined to satisfy the following criteria: (1) a depth (i.e., 200 μm) at which clear two-photon images of microglia and vessels could be monitored with moderate laser power (low enough to avoid brain tissue damage), (2) I divided the captured images into four sections (each section, 50 μm), and estimated the microglia in each section, (3) the 2 most superficial layers (0 to 50 μm and 50 to 100 μm from the surface) were excluded to avoid the possible surgical damage, and (4) the 100-150 μm section and 150-200 μm section contained equal numbers of microglia, and so the data from these two sections (100 to 200 μm) were combined. Using the ImageJ plug-in, Simple Neurite Tracer, I then quantified microglial morphology based on the reconstructed Z-stacked confocal images. The number of microglial processes and total lengths were determined from confocal 3D image data (1024×1024 pixels, 0.139 μm/pixel, 0.5 μm Z-step, 30 slices). Cell body areas

were quantified using the segmented line tool in ImageJ. To define vessel-associated microglia, (1) a vertical line was drawn from the presumed center of the microglia the surface of a blood vessel, (2) signal intensities of microglia-associated green fluorescence (EGFP) and blood vessel-associated red fluorescence (Texas Red) were calculated along the ROI line using the "Multiplot" function in ImageJ, (3) the standard deviation of fluorescent intensity was subtracted from the original signal for each channel, and (4) if the distance along the microglia-blood vessel axis was below 4 pixels (1 μm) between the point the green fluorescence decreased to zero and the point the red fluorescence increased from zero, the microglia was defined to have "contacted" the blood vessel (vessel-associated microglia). I then calculated what percentage of microglia in the captured image were vessel-associated microglia. Using the ImageJ plug-in Coloc2, Pearson's correlation coefficient was calculated to assess colocalization of IBA1 and AQP4, IBA1 and CLDN5, and CD68 and AQP4. To define CD68 positive microglia, the number of CD68 puncta were counted in the microglia. More than two of the CD68 puncta in microglia were defined as CD68 positive microglia.

Co-localization of PDGFRβ and lectin fluorescent signals were used to determine pericyte coverage, defined as a percentage (%) of the PDGFRβ positive area overlapping with lectin positive vessel surface area in each image frame, as previously reported(Nikolakopoulou, et al., PLoS One, 2017; Bell, et al., Neuron, 2010). Pericyte density was quantified as PDGFRβ positive and DAPI positive cells.

Isolation of microglia and astrocytes

After euthanasia with ketamine and xylazine, animals were transcardially perfused with PBS to remove circulating blood cells in the CNS. The cortex was cut off and dissociated using Neural Tissue Dissociation Kits (130-093-231; Milteny Biotec, Bergisch Gladbach, Germany). Debris was filtered through a cell strainer (100 μL) with 5% BSA-PBS followed by treatment with debris removal solution (130-109-398; Milteny Biotec). I then used the magnetic-activated cell sorting (MACS) system with CD11b magnetic beads (for microglia, 130-093-634; Milteny Biotec) or anti-GLAST magnetic beads (for astrocyte, 130-095-826; Milteny Biotec) and an MS column (130-042-201; Milteny Biotec). RNA was extracted using RNeasy Plus Mini kit (74134; Qiagen, Hilden, Germany).

Gene expression analysis

The RNA in microglia and astrocyte was precipitated in the presence of isopropanol and sodium acetate at −80°C. The RNA pellet was washed with 70% ethanol on ice, air-dried, and resuspended in RNase-free water. Total RNA (1000 ng) from each sample was further quantified by Qubit fluorometric quantitation and analyzed by Agilent 2100 Bioanalyzer (Agilent Technologies, Santa Clara, CA). The samples were then hybridized to microarray slides with Whole Mouse Genome 4×44K v2 Microarray Kit (G4846A; Agilent Technologies, Santa Clara, CA). Microarray data were analyzed using R-Bioconductor package (open source software). Gene ontology (GO) terms were referenced from online tools in Metascape (http://metascape.org/) (Zhou, et al., Nature communications, 2019)

Electron microscopy with immunohistochemistry

To examine the 3D structure of microglia and vessels during immunostaining for CLDN5 and AQP4, serial images were acquired with 3D reconstruction using serial block-face scanning electron microscopy (SBEM) as previously described with some modifications (Katoh, et al., Sci. Rep., 2017). Briefly, the tissues were fixed in 4% paraformaldehyde solution in PBS and post-fixed overnight in the same solution. Brains were cut with a vibratome into 200 μm thick sections, and freeze-thawed after infiltration of PBS containing 30% sucrose (Parajuli, et al., J. Neurosci., 2012). After blocking for 1 hour in 5% BSA in PBS, slices were incubated overnight at 4°C with primary antibodies against CLDN5 (35-2500, Thermo Fisher Scientific; 1:100) or AQP4 (AB3594, Merck KGaA; 1:500). The slices for CLDN5 immunostaining were heated at 95°C for 1 min. After PBS wash, slices were incubated in HRP-conjugated secondary antibodies at 4°C for 3 hours in PBS. Immunoreactions were visualized using 0.5 mg/ml diaminobenzidine substrate (Sigma-Aldrich) with 10 mM H_2O_2 and enhanced with ice cold 0.04% OsO4 in PBS. After additional fixation with 2.5% glutaraldehyde in 0.1M PB (pH 7.4) at 4°C for 2 hours and washing with ice cold PBS, the slices were further incubated with 2% OsO4 in 1.5% potassium ferrocyanide in PBS for 1 hour on ice. After washing with double distilled water (dDW), the tissues were then incubated in filtered 1% thiocarbohydrazide solution for 20 min at RT. After washing again with dDW, the tissues were incubated in a newly prepared 2% OsO4 for 30 min at RT. The tissues were placed in 2% uranyl acetate at 4°C overnight and incubated in lead aspartate solution at 65°C for 30 min after washing with

dDW. The tissues were dehydrated in a graded series of ethanol (60%, 80%, 90%, and 99.5% for 5 min each), followed by infiltration with acetone that was dehydrated with a molecular sieve in a 1:1 mixture of resin and acetone and 100% resin. The resin was prepared with a Durcupan kit according to the manufacturer's instructions (Sigma-Aldrich) and 7% Ketjen black was added to increase Durcupan conductivity (Nguyen, et al., Sci. Rep., 2016). Trimmed sample surfaces were gold sputtered to increase conductivity and imaged on field emission-SEM (Merlin or Sigma, Carl Zeiss AG.) equipped with 3View (Gatan, Inc., Pleasanton, CA). The resulting serial images were handled by ImageJ with Fiji plugins (http://fiji.sc/). Segmentation and image analyses were performed with Microscopy Image Browser (http://mib.helsinki.fi.) and Amira (FEI Visualization Science Group, Hillsboro, OR, USA) software. Microglial soma were identified using established criteria, which include relatively small and elongated nuclei, with clumped chromatin beneath the nuclear envelope and irregular contours of cytoplasm and processes with lysosomes and long endoplasmic reticulum (Alan, Oxford University Press, 1991). The processes of these microglia were then tracked in these 3D images to identify process terminations associated with specific elements of the neurovascular unit.

Endothelial cell culture

Primary endothelial cell cultures were prepared by puromycin treatment method (Assmann, et al., Bio Protoc, 2017). The cerebral cortices of mice were minced with collagenase-based digestion medium and cultured with Dulbecco's Modified Eagle's Medium (DMEM) containing 10% fetal bovine serum (FBS) and 30 μg/ml of Endothelial Cell Growth Supplement (E2759; Sigma-Aldrich) in a 24-well plate coated with collagen IV for 5 days. Endothelial cells were selected through puromycin treatment (P8833; Sigma-Aldrich, 8 μg/ml, 3 days). Endothelial cells were washed twice with media before stimulation, and then stimulated (immersed) in a solution containing LPS (100 ng/ml) or IFNα (1,000 IU/ml) for 24 hours. Culture supernatants were collected after stimulation. The collected supernatant was stored at −80°C. Cytokine production was measured by Proteome Profiler, Mouse XL Cytokine Array Kit (ARY028; R&D systems).

Microglial culture

Isolation of primary adult microglial cultures was adapted from Singh et al. (Singh, et al.,

Chem. Res. Toxicol., 2014). Briefly, the whole brain tissues of adult mice (C57BL/6, 9 weeks old) were dispersed with papain-based digestion medium and the microglia-rich fraction was isolated using Percoll (17-0891-02, GE Healthcare, Uppsala, Sweden) density gradient centrifugation. The microglial pellet was washed and cells were seeded on to 24 or 96-well plates in DMEM containing 10% FBS and incubated at 37°C for 10 min, and then the plate was washed with culture medium to remove non-adherent cells. The purity of CD11b positive microglia was confirmed by flow cytometry. The adherent microglia were maintained in DMEM containing 10% FBS for 0-6 hours, or stimulated for 1 hour with 100 ng/ml CCL5 (594202, BioLegend, San Diego, CA, USA) before being collected for real time PCR analysis. Primary neonatal microglia were prepared from a primary mix-culture (Tokizane, et al., Glia, 2017). The cerebral cortices of neonatal mice (C57BL/6, 0 days old) were minced and treated with trypsin-based digestion medium, and then dispersed cells were cultured in DMEM containing 10% FBS in culture flask (75 cm^2; 658170, Greiner Bio-One, Kremsmünster, Austria) in a 5% CO_2 humidified incubator at 37°C for 10-12 days. Microglia were detached by gently shaking the flask and these floating cells were collected and plated on 24 or 96 well plates in DMEM containing 10% FBS. Non-adherent cells were removed after 20-30 mins leaving adherent microglial cells that were incubated for 1 hour with 100 ng/ml CCL5 before being collected for real time PCR analysis.

Flow cytometry

Microglia and endothelial cells were isolated from LPS-injected Cx3cr1-GFP mice and MRL/lpr::Cx3cr1-GFP mice using a collagenase-based digestion medium. The isolated cells were treated with anti-CD16/32 antibody to block Fc receptors (70-0161-U100, TONBO Biosciences, San Diego, CA) before staining. The samples were then processed in PBS solution containing 5% fetal bovine serum (FBS) and 2 mM EDTA. The first antibodies against CD31 (14-0311-81, Thermo Fisher Scientific; 1:100) and CLDN5 (35-2500; Thermo Fisher Scientific; 1:100) were incubated for 1 hour at 4°C. Secondary anti-mouse Alexa 405 and anti-rat Alexa 647 (Abcam; 1:500 for each) antibodies were incubated for 30 min at 4°C. To evaluate the purity of microglial cultures, primary antibodies against CD31 (PE (phycoerythrin) conjugated, 102507, BioLegend; 1:100) and CD11b (APC (allophycocyanin) conjugated, 101211, BioLegend; 1:100) were used. Stained cells were acquired using FACS Aria III or FACS CantoII (BD Biosciences, San

Jose, CA), and the data were analyzed using FlowJo software (BD Biosciences). Compensation for spectral overlap between Alexa 405, GFP, PE, Alexa 647, APC was calculated with FACSDiva software using single-stained samples.

Real Time PCR

To quantify the expression of Cldn5 in microglia, total RNA was extracted from MACS-isolated microglia. First-strand complementary DNA (cDNA) was synthesized from total RNA using Transcriptor First Strand cDNA Synthesis Kit (04896866001, Roche Diagnostics, Mannheim, Germany) or SuperScript III (18080093, Thermo Fisher Scientific). Amplification reactions were performed on LightCycler 96 System (Roche Diagnostics) using the FastStart Essential DNA Green Master (06402712001, Roche Diagnostics). Amplification results were analyzed with the LightCycler or StepOnePlus (Thermo Fisher Scientific) using the FastStart Essential DNA Green Master (06402712001, Roche Diagnostics) or Fast SYBR Green Master Mix (Thermo Fisher Scientific). Amplification results were analyzed with the LightCycler or StepOnePlus software and then normalized on the basis of the Gapdh mRNA levels in each sample. The primer sequences used for the real-time PCR of target gene (Cldn5) were forward: 5′-GCTGGCGCTGGTGGCACTCTTTGT-3′ and reverse: 5′-GGCGAACCAGCAGAGCGGCAC-3′, (Ccr5) were forward: 5′-AGACATCCGTTCCCCCTACA-3′ and reverse: 5′-GCAGGGTGCTGACATACCAT-3′ and for Gapdh were forward: 5′-AATGCATCCTGCACCACCAAC-3′ and reverse: 5′-TGGATGCAGGGATGATGTTCTG-3′.

Data analysis and statistics

Data were analyzed using GraphPad Prism 8 statistical software (GraphPad Software Inc., La Jolla, CA). All data are presented as means ± SD. Unpaired t-test, ANOVA followed by Holm-Sidak post-hoc test, and Pearson's correlation tests were used to test for statistical significance.

Results

Association of microglia with the vessels and BBB leakage in MRL/lpr mice

Characterize the microglia and vessels using confocal microscopy

To verify the interaction between microglia and the BBB during systemic inflammation, I performed immunostaining of microglia and blood vessels using fixed brain tissue of MRL/lpr mice as a mouse model of SLE. As a result of co-staining with IBA1 as a microglial marker and Aquaporin-4 (AQP4), which is known to be localized in the astrocyte end-feet as a vessel marker, it was revealed that microglia have a dense contact with the vessels in the cortex of MRL/lpr mice (Fig. 1a). The ratio of vessel-associated microglia to the total number of microglia was significantly increased in MRL/lpr mice compared with that of wild-type mice (Fig. 1b). In addition, the number of IBA1-positive microglia in brain parenchyma and not in contact with the vessels was significantly reduced in MRL/lpr mice, while the number of microglia in the cortex was not different between wild-type mice and MRL/lpr mice. These results suggest that the parenchymal microglia may migrate to the vessels and accumulate around there (Fig. 1c).

Evaluation of BBB permeability by *in vivo* imaging

To assess BBB permeability, three different molecular weights of fluorescently labeled dextran (10 kDa, 40 kDa, 70 kDa) were intravenously administered to 9-week-old MRL/lpr mice simultaneously with *in vivo* two-photon imaging. In wild-type mice with an intact BBB, 10 kDa dextran does not leak into the brain parenchyma (Ben-Zvi et al., Nature, 2014). Using dyes with different fluorescence wavelengths for each of the three colors, fluorescence was separated and detected using a dichroic mirror and a bandpass filter, and the ratio of leakage was calculated based on the fluorescent intensity outside the vessel compared with that of wild-type parenchyma (Fig. 2a-b). As a result, dextran with a molecular weight of 10 kDa leaked in MRL/lpr mice (Fig. 3a-b). Leakage of larger dextrans (40 kDa and 70 kDa) were not detected.

Microglial migration and temporal changes of BBB permeability

Temporal changes of microglial accumulation around the vessels (daily LPS injections)

To clarify whether the migration of microglia to the vessels is caused by systemic inflammation, I used LPS-induced inflammation model. Cx3cr1-GFP mice that express GFP specifically in microglia were intraperitoneally injected LPS, a major component of bacteria. *In vivo* imaging was performed continuously for 7 days before

and after inflammation induced by LPS administration, thereby verifying time course changes in microglia. As a result, it was observed that microglia migrated and contacted the vessels after LPS administration (Fig. 4a). There was no migration during the 7 days before LPS administration and without LPS administration, and the percentage of vascular contact microglia did not change. In contrast, the percentage of vessel-associated microglia increased within 1 day after LPS administration. This increased percentage lasted 7 days after continuous LPS administration (Fig. 4a-b). There was no change in the total cell number of microglia (Fig. 4c).

Temporal changes of BBB permeability (daily LPS injections)

To verify changes in BBB permeability in LPS-treated mice, leakage of fluorescently labeled dextran was evaluated through the *in vivo* imaging. As a result, it was revealed that 10 kDa dextran leaked significantly from the day 4 after LPS administration (Fig. 5a-b). Leakage of larger dextrans (40 kDa and 70 kDa) were not detected (Fig. 5c). In addition, the leakage of fibrin (~ 340 kDa), which is also used as a marker for evaluating BBB leakage, was confirmed by immunostaining and was not detected in both groups of MRL/lpr mice and LPS-treated mice (Fig. 6a-b). These results suggest that continuous administration of LPS leads to increased BBB permeability, whereas that microglia accumulation around vessels precedes increased permeability of 10 kDa dextran.

Microglial migration and BBB permeability (single LPS injection)

To evaluate the accumulation of microglia around the vessels after acute inflammation, systemic inflammation was induced by a single administration of LPS. As a result, the percentage of vessel-associated microglia increased within 1 day after administration and then continued for 7 days (Fig. 7a). During that time, increasing of BBB permeability did not occur (Fig. 7b).

Characterize of vessel-associated microglia

Morphological analysis by confocal microscopy

Microglia that are resident cells in the CNS have finely branched processes as morphological features (called “resting” or “ramified” phenotype), and stretch and retract their processes in normal condition. On the other hand, when activated through detection of the tissue damage or pathogens, the morphology changes dramatically, resulting in a called amoeboid shape with processes retracted. That is, a decrease in the length and

number of processes and an increase in cell body area mean microglial activation. I examined the changes of microglial morphology in order to characterize vessel-associated microglia. Microglial morphology of wild-type and MRL/lpr mice was analyzed from three-dimensional (3D) images acquired with a confocal microscope. As a result, it was revealed that the number and length of the processes of MRL/lpr mice that associated with the vessels were significantly reduced compared to the wild-type mice (Fig. 8a-c). There was no difference in cell body area (Fig. 8d). Furthermore, time course changes of morphology due to daily LPS administration were verified based on two-photon microscope images. As a result, the number of processes were reduced, and the area of the cell body was increased during inflammation continues by LPS injection (Fig. 8e-g). From these results, it was clarified that the morphology of vessel-associated microglia during systemic inflammation showed an activated phenotype.

Evaluation of microglia specific markers

Macrophages expressing CX3CR1 and IBA1 exist around the vessels (known as perivascular macrophage: PVM), and it has been reported to be involved in the regulation of the BBB and blood-retinal barrier (BRB) through the production of basement membrane components (Faraco et al., J. Mol. Med., 2017; Mendes-Jorge et al., Invest. Ophthalmol. Vis. Sci., 2009). However, TMEM119 and SALL1, which are known as microglia-specific markers, are known not to be expressed in monocyte-derived cells (Bennet et al., PNAs, 2016; Buttgereit et al., Nat. Immunol., 2016). I examined the expression of microglia-specific markers in vessel-associated microglia of MRL/lpr mice and LPS-treated mice, and confirmed whether the vessel-associated IBA1-positive cells that increase with systemic inflammation are resident microglia. When the fixed brain tissue of MRL/lpr mice was immunostained, all vessel-associated IBA1-positive cells were TMEM119 positive (Fig. 9a). In addition, SALL1 was expressed in vessel-associated microglia in the LPS-treated Sall1-GFP mice that expressed green fluorescent protein GFP with the expression of SALL1, and GFP and IBA1 were co-localized (Fig. 9b-c). These results suggest that the origin of vessel-associated microglia is not the monocyte-derived cells but the brain parenchymal microglia.

Evaluations of pericyte changes in MRL/lpr mice and LPS-treated mice

Pericyte is present in the basement membrane that covers the outer surface of vascular endothelial cells, and it has recently been clarified that a decrease in the number of cells and vascular coverage leads to BBB dysfunction, and plays an important role in

maintaining BBB function (Armulik et al., Nature, 2010; Nikolakopoulou et al., Nature Neurosci., 2019). I examined whether any changes occurred in pericytes of MRL/lpr mice and LPS-treated mice. Immunostaining was performed with PDGFRβ, which is a marker for pericyte, AQP4 as a vascular marker, fluorescently labeled Lectin that specifically binds to glycans of endothelial cells, and DAPI for staining of cell nuclei. As a result of observing vessels and pericytes with a confocal microscope, both MRL/lpr mice and LPS-treated mice showed no difference in the number of pericytes and vascular coverage compared to that of control mice (Fig. 10a-e).

Molecular basis of microglial migration toward vessels

Chemoattractant produced from endothelial cells

Microglia accumulation occurs prior to the increased BBB permeability. Therefore, I hypothesized that a chemokine was secreted from the vessels to attract microglia before BBB dysfunction. To identify molecules candidate for chemoattractant, I evaluated chemokine production from endothelial cells depending on the inflammation stimulus. Endothelial cells isolated and cultured from wild-type mice were stimulated with LPS or IFNα, a cytokine characteristic of SLE patients and MRL/lpr mice. Cytokines in the culture supernatant were detected using the cytokine array system. As a result, production of the chemokine CCL5 was markedly upregulated in both LPS and IFNα stimulation (Fig. 11a-b).

Microglial migration during CCL5-CCR5 pathway inhibition

Changes in microglia migration and BBB permeability were verified by administering D-Ala-peptide T-amide (DAPTA), which is an antagonist of CCR5, CCL5 receptor. I performed surgery to enable imaging simultaneously with direct administration of DAPTA into the cerebral ventricle through a cannula (Fig. 11c). When systemic inflammation was induced by intraperitoneal injection of LPS under DAPTA treatment, microglial migration was suppressed 1 day after LPS injection. The accumulation of microglia toward the vessels was suppressed in DAPTA-treated mice compared to LPS-alone mice (Fig. 11d-e). In addition, the stimulation by intravenous administration of IFNα similarly suppressed the accumulation of microglia around the vessels (Fig. 11g).

Changing of BBB permeability during CCL5-CCR5 pathway inhibition

To assess the role of CCL5 signal in BBB integrity, the BBB permeability under DAPTA treatment was measured. Under LPS-treated condition, DAPTA-treated mice had

earlier leakage than LPS-alone mice. BBB permeability increased 2 days after LPS injection (Fig. 11f). This may be due to a delay in the accumulation of microglia. IFNα did not cause increased BBB permeability during this experiment (Fig. 11h). These results suggest that the CCL5-CCR5 signal plays an important role in the accumulation of microglia around the vessels and their protective effects on BBB in early phase of systemic inflammation.

Effect of microglia ablation on BBB permeability

Microglia ablation using Iba1-tTA::tetO-DTA mice

To understand the role of microglia on the permeability of BBB, the permeability change with LPS treatment during microglia ablation was examined. For microglia ablation, a mouse expressing the tetracycline-regulated trans-activator tTA downstream of the microglia-specific promoter Iba1 was mated with a knock-in mouse expressing diphtheria toxin downstream of the tetO sequence (Iba1-tTA::tetO-DTA mouse). They were raised on a chow containing doxycycline (Dox). Dox withdrawal (Dox-Off) induces microglia death due to the expression of microglia-specific diphtheria toxin. It was confirmed by immunostaining that the number of microglia decreased in Dox-Off mice. As a result, the number of vessel-associated microglia was significantly reduced in Dox-Off mice (Fig. 12a-c).

Changes BBB permeability after microglia ablation

Under microglia ablation, change of BBB permeability was evaluated in LPS-treated mice. Significant increase in permeability occurred on the day 3 after LPS injection, and on the other hand, BBB leakage was suppressed on the day 7 (Fig. 13a-b). It was found that in mice from which microglia had been ablated, the leakage was promoted in early phase, but it does not worsen even prolonged inflammation. These results suggest that microglia act protectively on the BBB permeability early in the inflammation, and that the BBB integrity is impaired during chronic inflammation.

Effects of microglia ablation on vessels and astrocyte

Under microglia ablation without LPS injection, the expression of Glial fibrillary acidic protein (GFAP), which is known to increase when astrocytes are activated, was confirmed by immunostaining. Its expression was slightly increased by microglia ablation (Fig. 12d-e). In addition, it was confirmed that there was no increase in BBB permeability in Dox-Off mice without LPS injection (Fig. 12f).

Altering gene expression in microglia induced by systemic inflammation

In order to investigate the microglia functions related to the permeability control by microglia, I performed a comprehensive analysis of gene expression in microglia. First, microglia were collected from the wild-type or MRL/lpr mouse brain using magnetic-activated cell sorting (MACS). The expression of a gene in microglia was analyzed by using microarray. As a result, I found increased expression of a tight junction-related molecular group, including claudin5 (Cldn5) that has not been reported in microglia, and increased expression of a phagocytosis-related molecular group (Fig. 14).

CLDN5 expression in microglia

To verify the expression of CLDN5 in MRL/lpr mice, I performed immunostaining of CLDN5, IBA1 and AQP4 or CD31 as vascular markers. As a result of observation using a confocal microscope, it was found that CLDN5 was expressed in vessel-associated microglia of MRL/lpr mice. (Fig. 15a-c). Furthermore, vessel-associated microglia and parenchymal microglia were distinguished, and as a result of counting IBA1-positive cells co-localized with CLDN5, the ratio of CLDN5-positive cells was increased in vessel-associated microglia of MRL/lpr mice compared with that of wild-type mice (Fig. 15b).

CD68 expression in microglia

To verify the expression of CD68 in MRL/lpr mice, immunostaining of CD68, IBA1 and AQP4 as vascular markers was performed. CD68 is a phagocytic marker localized in lysosomes. When microglia become phagocytic phenotype, the number and volume of CD68-positive vesicles increase. Microglia with two or more CD68-positive vesicles were defined as CD68 positive microglia. It was found that the percentage of CD68-positive cells was higher in vessel-associated microglia than in parenchymal microglia, and the highest in MRL/lpr mice (Fig. 16a-b).

Correlation between CLDN5 and CD68 expression

Since both CLDN5-positive cells and CD68-positive cells existed in MRL/lpr mice, the correlation between CLDN5 expression and CD68 expression for each cell was examined. As a result, CLDN5 and CD68 expression was inversely correlated (Fig. 16c). In addition, there was a correlation between the expression of IBA1 (Ito et al., Brain Res. Mol. Brain Res., 1998), which is known to increase with activation, and the expression

of CD68. Confocal images revealed that CD68 increased with the activation of microglia (Fig. 16d). This result suggests that CLDN5 and CD68 expression varies depending on the stage of inflammation.

CLDN5 expression in early phase of inflammation

Time course of CLDN5 expression in LPS-treated mice

To clarify temporal changes of CLDN5 expression in microglia, immunostaining was performed using LPS-induced systemic inflammation model. Confocal imaging revealed that vessel-associated microglia expressed CLDN5 within 1 day and 4 days after LPS injection, and this expression decreased after 7 days (Fig. 17a-b, 18a-b). This suggests that microglial CLDN5 is transiently expressed by inflammation.

Verification of CLDN5 expression in microglia

To further confirm CLDN5 expression in microglia, protein expression was verified using flow cytometry. CLDN5-positive microglia were detected in microglia of MRL/lpr mice and LPS-injected mice（Fig.19a-b）。In addition, there was no change in CLDN5 expression in vascular endothelial cells (Fig. 19c).

Microstructure and CLDN5 localization in vessel-associated microglia

To clarify the structure of microglia contact site and the expression of CLDN5 in high resolution, the microstructure of the contact surface of the vessel-associated microglia of MRL/lpr mice was observed with a three-dimensional electron microscope. It was observed that microglial processes expressing CLDN5 penetrated the basement membrane and were in direct contact with endothelial cells (Fig. 20). These results suggest that microglia directly act on vascular endothelial cells during systemic inflammation and may form a tight junction that act protectively on BBB.

Signals that induce CLDN5 expression

Wild-type mice were stimulated with LPS under CCR5 inhibition, microglia were isolated and collected, and qPCR was performed to verify Cldn5 expression. In the LPS-treated mice, Cldn5 expression was transiently increased on the Day 1 and Day 4 after LPS injection similar to the results of immunostaining (Fig. 21a). In contrast, Cldn5 expression was remarkably suppressed on the Day 4 in the DAPTA-treated mice. Furthermore, CCL5 stimulation was performed using cultured microglia from neonates or adult mice, and Cldn5 expression was verified by qPCR. CCL5-stimulated microglia derived from adult mice increased Cldn5 expression (Fig. 21b). Microglia derived from

adult mice express CCL5, a receptor for CCL5, but the expression decreased in culture medium without CCL5 1-3 hours after the start of culture (Fig. 21c). Microglia derived from adult mouse brains express Ccr5, a receptor for CCL5, but Ccr5 expression decreased in culture medium without CCL5 1-3 hours after the start of culture (Fig. 21c). The purity of the cultured microglia used in this experiment was verified using flow cytometer. The CD11b-positive microglia were 92% or more and the contamination of CD31-positive endothelial cells was 0.5% or less (Fig. 21d). On the other hand, Ccr5 was not expressed in microglia derived from neonatal brains, and Cldn5 expression was not increased by CCL5 stimulation (Fig. 21b-c). These results suggest that the CCL5-CCR5 signal pathway plays an important role in inducing Cldn5 expression in microglia.

Microglial phagocytosis of BBB component during prolonged inflammation

Time course of CD68 expression in LPS-treated mice

Immunostaining was performed using LPS-treated mice in order to verify temporal changes in CD68 expression in microglia. Observation by confocal microscopy showed that the percentage of CD68-positive microglia gradually increased by Day 7 after LPS administration (Fig. 22a-b). This suggests that the phagocytosis ability of microglia enhances with prolonged inflammation.

Microglial phagocytosis of astrocytic end-feet

As a result of detailed observation of CD68 positive vesicles in microglial cells, it was found that AQP4, astrocyte end-feet marker, was included in lysosomes (Fig. 22c). Furthermore, the number of microglia with AQP4 inclusion was significantly elevated 7 days after LPS administration (Fig.22d).

Microstructure and Aqp4 inclusion in vessel-associated microglia

Using serial block-face scanning electron microscopy (SBF-SEM), the microstructure of microglia was observed. Using a continuous block surface scanning electron microscope (Serial Block-face SEM, SBF-SEM) method, I verified the inclusion of astrocytes end-feet in microglial lysosome. As a result of observing the inside of the contact microglia, AQP4 signal was observed inside the intracellular phagocytic vesicle (Fig. 23). These results suggest that microglial phagocytosis increases with prolonged systemic inflammation, and that phagocytosis of the astrocyte end-feet causes the breakdown of the BBB structure.

Signals that induce CD68 expression

A decrease in the number of synapses has been reported in SLE model mice with CNS symptoms. It has been clarified that knockout of type I interferon receptor or administration of a neutralizing antibody suppresses excess synapse elimination by microglia (Bialas et al., Nature, 2017). IFNα is a cytokine detected in the serum of SLE patients and MRL/lpr mice. I injected IFNα directly to the brain parenchyma of wild-type mice and co-stained with CD68 and IBA1. As a result, the number of CD68 positive microglia was significantly increased in IFNα-injected mice (Fig. 24a-b). This suggests that IFNα enhances expression of CD68 in microglia and microglial phagocytosis.

BBB permeability during inhibition of microglia activation in late phase of inflammation

Inhibition of microglia activation using minocycline

Since it was suggested that microglial activation causes phagocytosis of BBB components, I examined whether inhibition of activation could suppress BBB leakage. I continuously injected minocycline (Mino), which is known to suppress the activation of microglia, into the peritoneal cavity. The morphological changes associated with microglia activation during LPS stimulation were evaluated (Fig. 25a). As a result, administration of minocycline suppressed the retraction of microglial processes and the increase in cell body area (Fig. 25b). In addition, when I administrate minocycline alone without LPS stimulation, the morphology of microglia was not affected (Fig. 26a-b). These results suggest that Mino administration can suppress microglia activation by LPS continuous administration.

Microglia migration in minocycline-treated mice

I verified whether minocycline treatment affects the accumulation of microglia around the vessels. As a result of observing temporal changes in microglia under Mino treatment, the proportion of vessel-associated microglia was increased with LPS stimulation (Fig. 25c). This suggests that Mino administration may not affect the accumulation of microglia around the vessels. Also, when I administrate minocycline alone without LPS stimulation, there was no effect on the movement of microglia (Fig. 26c).

BBB permeability in minocycline-treated mice

As a result of evaluating changes in BBB permeability under administration of minocycline, leakage on Day 4 and 7 after LPS stimulation was significantly suppressed

while leakage during early phases of inflammation (Day1-3) did not worsen (Fig. 25d). Also, when I administrate minocycline alone without LPS stimulation, there was no effect on the BBB permeability (Fig. 26d).

Discussion

Background and purpose

Microglial protective functions for regulation of blood vessels have not only been related to angiogenesis by the production of VEGF and IGF-1 (Xie, et al., Vasc Cell, 2013; Lalancette-Hebert, et al., J. Neurosci., 2007). It has also been reported that, microglia accumulate their processes and suppress BBB leakage in an ATP-dependent manner in response to artificial damage using a laser (Lou, et al., Proc. Natl. Acad. Sci. U. S. A., 2016). On the other hand, microglia activated by acute stroke or accumulation of Aβ are also known to damage BBB by cytokine production and excessive phagocytosis (Lambertsen, et al., J. Cereb. Blood Flow Metab., 2012; Ryu and McLarnon, Exp. Neurol., 2006). In addition, activation of the systemic immune system associated with infections and autoimmune diseases leads to microglia activation and decreased BBB integrity (Danielski, et al., Mol. Neurobiol., 2018; Bialas, et al., Nature, 2017). It is necessary to understand in detail the role of BBB regulation in microglia to elucidate the mechanism of BBB breakdown that causes CNS diseases. The purpose of this study was to elucidate how microglia, which are immune cells, are involved in changes in BBB permeability caused by systemic inflammation.

Migration of microglia toward blood vessels

In this study, it was revealed that the molecular weight-selective hyperpermeability of BBB occurred in the brain of MRL/lpr mice, an autoimmune disease model, and the number of vessel-associated microglia was increased. As a result of *in vivo* imaging using LPS-injected mice, it was found that microglia migrated and accumulated around the vessels within one day after induction of systemic inflammation. It was also found that the permeability of BBB increases after continuous injection of LPS. Chemokine signal inhibition by chemokine receptor inhibitors revealed that the signal of CCL5 produced by vascular endothelial cells and CCR5, which is a receptor on the microglia, play an important role in the accumulation of microglia around the vessels. Previously, it has been known that the breakdown of BBB causes microglial accumulation. In a model of EAE, fibrinogen leaked from vessels has been reported to induce microglial migration to the vessels, causing axonal damage to surrounding neurons through the production of reactive oxygen species (Davalos, et al., Nat Commun, 2012). In the case of this study, it was considered that the attractant was produced from the vessels before

the increasing of BBB permeability because the microglia accumulated in the vessels prior to the leakage. Immune cells express chemokine receptors, which are important factors for tissue invasion and migration to lesion sites. A number of studies has been done on chemokine-chemokine receptor signals that cause microglial migration. In Alzheimer's disease, CCR2 has been shown to be important for microglial accumulation to Aβ deposit (El Khoury, et al., Nat. Med., 2007). CX3CL1 is a ligand for the microglia-specific receptor CX3CR1 and plays an important role in synapse elimination during CNS development (Paolicelli, et al., Science, 2011), as well as it is important for the microglial migration to the barrel structure of the somatosensory cortex (Hoshiko, et al., J. Neurosci., 2012). CCL5 (also known as RANTES) is produced by T cells, macrophages, dendritic cells and endothelial cells, and it is known to trigger for the migration of T cells, monocytes, eosinophils and basophils via the chemokine receptors CCR1, CCR3 and CCR5 (Griffith, et al., Annu. Rev. Immunol., 2014). CCR5 is important in the immune system to recruit monocytes and Th1 cells to the inflammatory site (Campbell and Butcher, Curr. Opin. Immunol., 2000). CCR5 acts as a protective factor against encephalitis during West Nile virus infection by recruiting immune cells, as well as CCR5 mutations have been reported to increase the risk of encephalitis (Glass, et al., J. Exp. Med., 2005). CCL5-CCR5 signal not only triggers immune cell migration, but also has a function of suppressing apoptosis in macrophages during virus infection (Tyner, et al., Nat. Med., 2005), and inducing the differentiation of T cells (Luther and Cyster, Nat. Immunol., 2001). CCL5 has been reported as a factor inducing the remodeling of the microglial actin cytoskeleton. It has been reported that CCL5 involved in the accumulation of microglia at the lesion site of trauma or multiple sclerosis (Cross and Woodroofe, J. Neurosci. Res., 1999). Microglia express the CCR5, which is CCL5 receptor (Sorce, et al., Prog. Neurobiol., 2011). The function of CCL5 in the central nervous system is poorly understood, although it has been reported that CCL5 is detected in the cerebrospinal fluid of SLE patients with psychiatric symptoms and patients with autism spectrum disorders (ASD) (Fragoso-Loyo, et al., Arthritis Rheum., 2007). In multiple sclerosis, cerebral infarction and epilepsy, increasing of CCL5 concentration in cerebrospinal fluid has also been reported (Louboutin and Strayer, CNS Neurol. Disord. Drug Targets, 2013). DAPTA, used to inhibit the CCL5-CCR5 signal in this study, is an antagonist that selectively binds to CCR5. DAPTA has been reported to suppress the production of inflammatory cytokines from microglia by suppressing the activation of

transcription factor NF-κB downstream of CCR5 (Rosi, et al., Neuroscience, 2005). In the results of this study, chemokines were produced from vascular endothelial cells resulting attracted microglia to the vessels in the early phases of inflammation before BBB breakdown. This study proposes a new concept that microglia accumulates around the vessels by CCL5-CCR5 signal and protect the BBB integrity.

CLDN5 expression and contribution to the BBB function

As a result of observing the contact area between microglia and vessels with a high resolution using a three-dimensional electron microscope, it was found that microglia penetrated the astrocyte end-feet and basement membrane. Furthermore, CLDN5-positive microglial processes were found to be in direct contact with vascular endothelial cells. The claudin family is known as a tight junction proteins, and there are differences in their expression patterns in each tissue (Furuse, et al., J. Cell Biol., 1998; Van Itallie and Anderson, Physiology (Bethesda), 2004). CLDN5 is expressed in vascular endothelial cells in the brain and forms a tight junction by forming homophilic adhesion between cells, and is a necessary molecule for constructing BBB (Van Itallie and Anderson, Physiology (Bethesda), 2004). It has been shown in CLDN5-deficient mice that CLDN5 actually plays an important role as a barrier that limits molecular diffusion. In this mouse, leakage of a fluorescent tracer of 800 Da or less has been revealed increasing of molecular weight selective leakage (Nitta, et al., J. Cell Biol., 2003). There are several reports on the expression of tight junction proteins in immune cells. It has been suggested that macrophages and dendritic cells residing in the lung may form tight junctions with epithelial cells and take up extraneous particles while maintaining the barrier function (Blank, et al., Immunobiology, 2011). The studies using the EAE model have reported that circulating immune cells express CLDN5 when passing through the BBB, and may infiltrate from the vessels to the brain parenchyma without causing BBB disruption (Paul, et al., J. Neuroinflammation, 2016). Studies focusing on inflammatory joint diseases have also found that macrophages present in the synovium in the joint act to protect the joint from immune cell infiltration by expressing CLDN5 (Culemann, et al., Nature, 2019). Thus, it is considered that not only epithelial cells and endothelial cells but also immune cells contribute to barrier formation. This study was the first to reveal transient CLDN5 expression in microglia and revealed its contribution to the barrier function in BBB. Previously, in the comprehensive analysis of gene expression such as

RNA-seq in microglia, the expression of Cldn5 is very little compared with endothelial cells and has not been verified (Zhang, et al., J. Neurosci., 2014). In this study, I observed changes over time in LPS-injected mice and immunostaining of CLDN5, and found that vessel-associated microglia transiently express CLDN5 triggered by systemic inflammation and the accompanying CCL5 signal. It is considered that the conventional method of analyzing whole cell genes of a tissue may not be able to detect a small cell population or transient expression. Furthermore, it has been pointed out that there are actually differences in the gene expression patterns of individual cells. Single cell level analysis combining in situ hybridization and RNA-seq has reported that even if the same cell types is compared, diverse in expression patterns occur due to differences in adjacent cells and regions. (Eng, et al., Nature, 2019). In reports of RNA-seq analysis at the single cell level, microglia that express Cldn5 have been detected (Li, et al., Neuron, 2019).

Phagocytosis of BBB component by microglia

In MRL/lpr mice, CLDN5-positive microglia and CD68-positive microglia were mixed, and their expression was inversely correlated within single microglial cell. Furthermore, along with prolonged inflammation due to daily injection of LPS, the expression of CD68, a lysosomal marker, increased simultaneously with the decrease in CLDN5 expression in microglia. This result suggests that prolonged inflammation activated microglia and changed its function to the phagocytic type. In addition, AQP4, a component of the astrocyte end-feet, was contained inside the microglia phagocytic vesicles, indicating that phagocytosis of BBB components by activated microglia. As a result of immunostaining and observation with an electron microscope, it was confirmed that AQP4 puncta was included into microglial phagocytic vesicles in direct contact with vascular endothelial cells. Since the structural breakdown of the astrocyte end-feet is thought to impair the function of the BBB (Ezan, et al., J. Cereb. Blood Flow Metab., 2012), microglial phagocytosis may associate with the BBB permeability. Type I interferon, a cytokine that is up-regulated in SLE patients, has been reported to change microglial function to a phagocytic phenotype (Bialas, et al., Nature, 2017). In this study as well, direct exposure of IFNα to microglia increased the expression of the phagocytic marker CD68. The genetic ablation of microglia accelerated BBB permeability during inflammation and conversely suppressed the increase during prolonged inflammation, suggesting that BBB was impaired by microglia. Whether or not such phagocytosis of

astrocyte end-feet by microglia is a beneficial phenomenon for individuals should be discussed. Phagocytosis by microglia is important for development and homeostasis of the brain environment. Several functions of phagocytosis were previously reported such as phagocytosis of dead cells and their debris (Brockhaus, et al., Glia, 1996; Neumann, et al., Brain, 2009; Tanaka, et al., J. Biol. Chem., 2009), phagocytosis of apoptotic neural stem cells (Sierra, et al., Cell Stem Cell, 2010) and regulation of synapses by phagocytosis. (Paolicelli, et al., Science, 2011). On the other hand, it is also known that excessive phagocytosis is associated with the progression of the disease. In Alzheimer's disease, Apolipoprotein E (APOE), which binds to both Aβ and apoptotic cells, is recognized through the microglia TREM2 and enhances phagocytic ability (Krasemann, et al., Immunity, 2017; Galloway, et al., Front. Immunol., 2019). Through APOE signal, it has been pointed out that the gene expression pattern of microglia changes to a pattern characteristic of neurodegenerative diseases. It has been reported that myelin debris is cleared by phagocytosis in multiple sclerosis, but in the presence of inflammatory cytokines such as IL-4, it works to exacerbate the pathological condition (Jack, et al., J. Neurosci. Res., 2005; Galloway, et al., Front. Immunol., 2019; Durafourt, et al., Glia, 2012). In addition, it has been reported that the phagocytic ability of microglia is enhanced during a stroke, phagocytosing not only dead cells but also living cells, and inducing cell death. The significance of this phenomenon called phagotosis has not been elucidated (Neher, et al., Proc. Natl. Acad. Sci. U. S. A., 2013). From a protective point of view, microglia may be responsible for tissue repair (remodeling) via engulfment of BBB components impaired by inflammation. On the other hand, excessive or chronic inflammation may enhance microglial phagocytosis, resulting tissue damage. In this study, disease model mice and continuous administration of LPS were used as systemic inflammation models. Using stimulation conditions that specific signal to be activated may reveal a mechanism that alters microglia function. It is necessary to verify the function of microglia and the BBB permeability by administration of a single cytokine or autoantibody, and LPS stimulation with extended intervals or low concentration.

Inhibition of microglial activation and changing of BBB permeability

Minocycline (Mino) is known to suppress the activation of microglia (Moller, et al., Glia, 2016). In addition, it has been reported that the Mino suppress BBB hyperpermeability in hypoxia, stroke, and Alzheimer-type cognitive impairment (Ryu and

McLarnon, Exp. Neurol., 2006; Yang, et al., J. Neuroinflammation, 2015; Yenari, et al., Stroke, 2006). In this study, it was found that administration of Mino can suppress the increase of BBB permeability at the phases of chronic inflammation induced by daily LPS injection. Mino treatment did not affecting the accumulation of microglia to the vessels and the suppression of leakage in the early stage of inflammation. From this result, it is considered that excessive phagocytosis can be suppressed by suppressing the activation of microglia, and the functional breakdown of BBB during systemic inflammation can be suppressed. Sickness behavior (reduced appetite and reduced social exploration) and depression-like behavior are known to occur in mice after LPS administration, but administration of Mino has been reported to improve these behavioral abnormalities (Dantzer, et al., Nat. Rev. Neurosci., 2008). As a mechanism behind this, increase of BBB permeability may be inhibited by suppressing microglia activation. In addition to spontaneous development of SLE-like systemic inflammation, MRL/lpr mice have been shown to exhibit abnormal behavior such as anxiety-like behavior, depression-like behavior and cognitive decline through the open field tests, forced swimming tests and water maze tests (Jeltsch-David and Muller, Autoimmun Rev, 2014). If the activation of microglia can be suppressed, it may be possible to inhibit an increase of BBB permeability and abnormal behavior. However, since the onset of MRL/lpr inflammation is not fixed in time, it could not be evaluated experimentally in this study. Further validation is required when testing minocycline administration. That is, whether it should be administered Mino before the increasing level of cytokines in the serum, whether it is effective even after the onset of symptoms, or whether removal of microglia is effective in suppressing permeability. Whether or not behavioral abnormalities can be improved by inhibiting the accumulation of microglia is one of the important future challenge for studying psychiatric symptoms associated with systemic inflammation.

Comparison with previous study and research limitations

For the detection of BBB hyperpermeability, there have mainly been methods of albumin concentration ratio in blood and cerebrospinal fluid, immunostaining of leaked IgG and fibrin, and chemical fixation after intravenous administration of a fluorescent tracer has been used. The imaging technique with the two-photon microscope used for the evaluation of BBB permeability was advantageous in that microglia can be observed in a living animal and that changes over time can be detect simultaneously with

the BBB permeability. However, in the small amount of local leakage that cannot be detected with a microscope and the specific transport of a molecule via a receptor, exhaustive confirmation has not been performed, and further verification is necessary. Regarding the function of microglia, the microglia ablation accelerates the increase in BBB permeability during the early phases of inflammation, indicating that microglia acts protectively against changes in permeability. However, it has not been proved that the tight junction of CLDN5 expressed in microglia actually functions as a barrier. Although there is a method for evaluating the barrier function by measuring transendothelial electrical resistance (TEER) using a culture system, there remains a problem in whether the interaction between BBB structure and microglia in the culture can be sufficiently reproduced *in vitro*. Cultured microglia have been reported to have some different pattern of gene expression from microglia in the brain (Butovsky, et al., Nat. Neurosci., 2014).

Previously, it has been shown that inflammatory cytokines such as TNFα, IL-1, and IL-6 decrease the expression of tight junction proteins in endothelial cells as a factor that increases BBB permeability in inflammation originating from outside the brain (Capaldo and Nusrat, Biochim. Biophys. Acta, 2009). It is necessary to verify in the future how cytokine production by microglia affects the function of BBB.

Whether the vessel-associated microglia have the ability to return to the original parenchymal microglia after the convergence of the inflammatory response is important in understanding the physiological functions of the microglia. It has been reported that microglia undergo epigenetic changes upon activation due to peripheral inflammatory training stimulus and affect subsequent functions as if “immune memory” (Wendeln, et al., Nature, 2018). In the observation of single injection of LPS, the vessel-associated microglia did not leave the vessels for 7 days after administration. Verification of the immune memory and reversibility of microglial function requires long-term observation.

Conclusion and future perspectives

The conclusion of this study is that microglia have the function of suppressing and enhancing the permeability of BBB and play different roles depending on the phase of inflammation. During the early phases of systemic inflammation, microglia expressed CLDN5 and accumulated around the vessels to suppress the increased BBB permeability. On the other hand, microglia became a phagocytic phenotype in prolonged inflammation, and they disrupt BBB structure by phagocytosing the astrocyte end-feet. In addition, the

CCL5-CCR5 pathway was identified as an important signal for migration of microglia to the vessels and BBB protection during early phases of inflammation. Administration of Mino did not affect the migration of microglia and significantly suppressed the increased BBB permeability. These results suggest the possibility of developing new treatments and prevention methods targeting microglia in the breakdown of BBB caused by systemic inflammation and the accompanying psychiatric and neurological symptoms. Further understanding of the BBB failure and repair process and the elucidation of the physiological functions of microglia are expected to be developed in the future. Especially in functionally diverse microglia, there may be small populations with new functions not previously detected. It is considered that analysis at the single cell level and the observation techniques of the same cell over time *in vivo* will become more important in this research field.

Acknowledgments

First and foremost, I would like to thank Prof. Junichi Nabekura whose experience and generous support were invaluable for this thesis. I am grateful to Prof. Hiroaki Wake of Department of Anatomy and Molecular Cell Biology, Nagoya University Graduate School of Medicine, for encouragement and supervision throughout the course of my doctoral thesis. I also would like to thank associate professor Dr. Yoshihisa Tachibana of Division of System Neuroscience, Kobe University Graduate School of Medicine, for kind advice and guidance of my study.

I also would like to thank Prof. Nobuhiko Ohno of Department of Anatomy, Division of Histology and Cell Biology, Jichi Medical University, who taught me electron microscope methods and encouraged me. I appreciate thank Dr. Hiroyuki Konishi and Prof. Hiroshi Kiyama of Department of Functional Anatomy and Neuroscience, Nagoya University Graduate School of Medicine, for their support of culture experiments and kind suggestion on my study.

I would gratefully thank to the member of my thesis committee Prof. Motohiro Nishida of Division of Cardiocirculatory Signaling, National Institute for Physiological Sciences; Prof. Mikio Furuse of Division of Cell Structure, National Institute for Physiological Sciences; Prof. Koji Yamanaka of Department of Neuroscience and Pathobiology, Research Institute of Environmental Medicine, Nagoya University.

Finally, I would like to thank all laboratory members as well.

References

Kettenmann, H., Hanisch, U.K., Noda, M. & Verkhratsky, A. Physiology of microglia. *Physiol. Rev.* **91**, 461-553 (2011).

Giulian, D. & Baker, T.J. Characterization of ameboid microglia isolated from developing mammalian brain. *J. Neurosci.* **6**, 2163-2178 (1986).

Imai, Y., Ibata, I., Ito, D., Ohsawa, K. & Kohsaka, S. A novel gene iba1 in the major histocompatibility complex class III region encoding an EF hand protein expressed in a monocytic lineage. *Biochem. Biophys. Res. Commun.* **224**, 855-862 (1996).

Perry, V.H., Hume, D.A. & Gordon, S. Immunohistochemical localization of macrophages and microglia in the adult and developing mouse brain. *Neuroscience* **15**, 313-326 (1985).

Raivich, G. & Banati, R. Brain microglia and blood-derived macrophages: molecular profiles and functional roles in multiple sclerosis and animal models of autoimmune demyelinating disease. *Brain Res. Brain Res. Rev.* **46**, 261-281 (2004).

Guillemin, G.J. & Brew, B.J. Microglia, macrophages, perivascular macrophages, and pericytes: a review of function and identification. *J. Leukoc. Biol.* **75**, 388-397 (2004).

Fujita, S. & Kitamura, T. Origin of brain macrophages and the nature of the so-called microglia. *Acta Neuropathol. Suppl.* **Suppl 6**, 291-296 (1975).

Ginhoux, F., Lim, S., Hoeffel, G., Low, D. & Huber, T. Origin and differentiation of microglia. *Front. Cell. Neurosci.* **7**, 45 (2013).

Chan, W.Y., Kohsaka, S. & Rezaie, P. The origin and cell lineage of microglia: new concepts. *Brain Res Rev* **53**, 344-354 (2007).

Ginhoux, F., Greter, M., Leboeuf, M., Nandi, S., See, P., Gokhan, S., Mehler, M.F., Conway, S.J., Ng, L.G., Stanley, E.R., Samokhvalov, I.M. & Merad, M. Fate mapping analysis reveals that adult microglia derive from primitive macrophages. *Science* **330**, 841-845 (2010).

Schulz, C., Gomez Perdiguero, E., Chorro, L., Szabo-Rogers, H., Cagnard, N., Kierdorf, K., Prinz, M., Wu, B., Jacobsen, S.E., Pollard, J.W., Frampton, J., Liu, K.J. & Geissmann, F. A lineage of myeloid cells independent of Myb and hematopoietic stem cells. *Science* **336**, 86-90 (2012).

Zhao, Y., Zou, W., Du, J. & Zhao, Y. The origins and homeostasis of monocytes and tissue-resident macrophages in physiological situation. *J. Cell. Physiol.* **233**, 6425-6439 (2018).

Krall, W.J., Challita, P.M., Perlmutter, L.S., Skelton, D.C. & Kohn, D.B. Cells expressing human glucocerebrosidase from a retroviral vector repopulate macrophages and central nervous system microglia after murine bone marrow transplantation. *Blood* **83**, 2737-2748 (1994).

Ajami, B., Bennett, J.L., Krieger, C., McNagny, K.M. & Rossi, F.M. Infiltrating monocytes trigger EAE progression, but do not contribute to the resident microglia pool. *Nat. Neurosci.* **14**, 1142-1149 (2011).

Elmore, M.R., Najafi, A.R., Koike, M.A., Dagher, N.N., Spangenberg, E.E., Rice, R.A., Kitazawa, M., Matusow, B., Nguyen, H., West, B.L. & Green, K.N. Colony-stimulating factor 1 receptor signaling is necessary for microglia viability, unmasking a microglia progenitor cell in the adult brain. *Neuron* **82**, 380-397 (2014).

Kennedy, D.W. & Abkowitz, J.L. Kinetics of central nervous system microglial and macrophage engraftment: Analysis using a transgenic bone marrow transplantation model. *Blood* **90**, 986-993 (1997).

Thomas, W.E. Brain macrophages: on the role of pericytes and perivascular cells. *Brain Res. Brain Res. Rev.* **31**, 42-57 (1999).

Ransohoff, R.M. & Cardona, A.E. The myeloid cells of the central nervous system parenchyma. *Nature* **468**, 253-262 (2010).

Prinz, M. & Priller, J. Microglia and brain macrophages in the molecular age: from origin to neuropsychiatric disease. *Nat. Rev. Neurosci.* **15**, 300-312 (2014).

Faraco, G., Park, L., Anrather, J. & Iadecola, C. Brain perivascular macrophages: characterization and functional roles in health and disease. *J. Mol. Med. (Berl.)* **95**, 1143-1152 (2017).

Hirasawa, T., Ohsawa, K., Imai, Y., Ondo, Y., Akazawa, C., Uchino, S. & Kohsaka, S. Visualization of microglia in living tissues using Iba1-EGFP transgenic mice. *J. Neurosci. Res.* **81**, 357-362 (2005).

Jung, S., Aliberti, J., Graemmel, P., Sunshine, M.J., Kreutzberg, G.W., Sher, A. & Littman, D.R. Analysis of fractalkine receptor CX(3)CR1 function by targeted deletion and green fluorescent protein reporter gene insertion. *Mol. Cell. Biol.*

20, 4106-4114 (2000).

Nimmerjahn, A., Kirchhoff, F. & Helmchen, F. Resting microglial cells are highly dynamic surveillants of brain parenchyma in vivo. *Science* **308**, 1314-1318 (2005).

Davalos, D., Grutzendler, J., Yang, G., Kim, J.V., Zuo, Y., Jung, S., Littman, D.R., Dustin, M.L. & Gan, W.B. ATP mediates rapid microglial response to local brain injury in vivo. *Nat. Neurosci.* **8**, 752-758 (2005).

Wake, H., Moorhouse, A.J., Jinno, S., Kohsaka, S. & Nabekura, J. Resting microglia directly monitor the functional state of synapses in vivo and determine the fate of ischemic terminals. *J. Neurosci.* **29**, 3974-3980 (2009).

Tremblay, M.E., Lowery, R.L. & Majewska, A.K. Microglial interactions with synapses are modulated by visual experience. *PLoS Biol.* **8**, e1000527 (2010).

Miyamoto, A., Wake, H., Ishikawa, A.W., Eto, K., Shibata, K., Murakoshi, H., Koizumi, S., Moorhouse, A.J., Yoshimura, Y. & Nabekura, J. Microglia contact induces synapse formation in developing somatosensory cortex. *Nat Commun* **7**, 12540 (2016).

Paolicelli, R.C., Bolasco, G., Pagani, F., Maggi, L., Scianni, M., Panzanelli, P., Giustetto, M., Ferreira, T.A., Guiducci, E., Dumas, L., Ragozzino, D. & Gross, C.T. Synaptic pruning by microglia is necessary for normal brain development. *Science* **333**, 1456-1458 (2011).

Schafer, D.P., Lehrman, E.K., Kautzman, A.G., Koyama, R., Mardinly, A.R., Yamasaki, R., Ransohoff, R.M., Greenberg, M.E., Barres, B.A. & Stevens, B. Microglia sculpt postnatal neural circuits in an activity and complement-dependent manner. *Neuron* **74**, 691-705 (2012).

Lehnardt, S. Innate immunity and neuroinflammation in the CNS: the role of microglia in Toll-like receptor-mediated neuronal injury. *Glia* **58**, 253-263 (2010).

Fiebich, B.L., Batista, C.R.A., Saliba, S.W., Yousif, N.M. & de Oliveira, A.C.P. Role of Microglia TLRs in Neurodegeneration. *Front. Cell. Neurosci.* **12**, 329 (2018).

Aloisi, F. Immune function of microglia. *Glia* **36**, 165-179 (2001).

Bennett, M.L., Bennett, F.C., Liddelow, S.A., Ajami, B., Zamanian, J.L., Fernhoff, N.B., Mulinyawe, S.B., Bohlen, C.J., Adil, A., Tucker, A., Weissman, I.L., Chang, E.F., Li, G., Grant, G.A., Hayden Gephart, M.G. & Barres, B.A. New tools for studying microglia in the mouse and human CNS. *Proc. Natl. Acad. Sci. U. S. A.*

113, E1738-1746 (2016).

Zeisel, A., Munoz-Manchado, A.B., Codeluppi, S., Lonnerberg, P., La Manno, G., Jureus, A., Marques, S., Munguba, H., He, L., Betsholtz, C., Rolny, C., Castelo-Branco, G., Hjerling-Leffler, J. & Linnarsson, S. Brain structure. Cell types in the mouse cortex and hippocampus revealed by single-cell RNA-seq. *Science* **347**, 1138-1142 (2015).

Butovsky, O., Jedrychowski, M.P., Moore, C.S., Cialic, R., Lanser, A.J., Gabriely, G., Koeglsperger, T., Dake, B., Wu, P.M., Doykan, C.E., Fanek, Z., Liu, L., Chen, Z., Rothstein, J.D., Ransohoff, R.M., Gygi, S.P., Antel, J.P. & Weiner, H.L. Identification of a unique TGF-beta-dependent molecular and functional signature in microglia. *Nat. Neurosci.* **17**, 131-143 (2014).

Buttgereit, A., Lelios, I., Yu, X., Vrohlings, M., Krakoski, N.R., Gautier, E.L., Nishinakamura, R., Becher, B. & Greter, M. Sall1 is a transcriptional regulator defining microglia identity and function. *Nat. Immunol.* **17**, 1397-1406 (2016).

Ayata, P., Badimon, A., Strasburger, H.J., Duff, M.K., Montgomery, S.E., Loh, Y.E., Ebert, A., Pimenova, A.A., Ramirez, B.R., Chan, A.T., Sullivan, J.M., Purushothaman, I., Scarpa, J.R., Goate, A.M., Busslinger, M., Shen, L., Losic, B. & Schaefer, A. Epigenetic regulation of brain region-specific microglia clearance activity. *Nat. Neurosci.* **21**, 1049-1060 (2018).

De Biase, L.M., Schuebel, K.E., Fusfeld, Z.H., Jair, K., Hawes, I.A., Cimbro, R., Zhang, H.Y., Liu, Q.R., Shen, H., Xi, Z.X., Goldman, D. & Bonci, A. Local Cues Establish and Maintain Region-Specific Phenotypes of Basal Ganglia Microglia. *Neuron* **95**, 341-356 e346 (2017).

Li, Q., Cheng, Z., Zhou, L., Darmanis, S., Neff, N.F., Okamoto, J., Gulati, G., Bennett, M.L., Sun, L.O., Clarke, L.E., Marschallinger, J., Yu, G., Quake, S.R., Wyss-Coray, T. & Barres, B.A. Developmental Heterogeneity of Microglia and Brain Myeloid Cells Revealed by Deep Single-Cell RNA Sequencing. *Neuron* **101**, 207-223 e210 (2019).

Gulke, E., Gelderblom, M. & Magnus, T. Danger signals in stroke and their role on microglia activation after ischemia. *Ther. Adv. Neurol. Disord.* **11**, 1756286418774254 (2018).

Barichello, T., Generoso, J.S., Simoes, L.R., Goularte, J.A., Petronilho, F., Saigal, P., Badawy, M. & Quevedo, J. Role of Microglial Activation in the

Pathophysiology of Bacterial Meningitis. *Mol. Neurobiol.* **53**, 1770-1781 (2016).

Kim, S.U. & de Vellis, J. Microglia in health and disease. *J. Neurosci. Res.* **81**, 302-313 (2005).

Barger, S.W. & Harmon, A.D. Microglial activation by Alzheimer amyloid precursor protein and modulation by apolipoprotein E. *Nature* **388**, 878-881 (1997).

Akiyama, H. Inflammation and Alzheimer's disease. *Neurobiol. Aging* **21**, 383-421 (2000).

McGeer, P.L., Itagaki, S., Boyes, B.E. & McGeer, E.G. Reactive microglia are positive for HLA-DR in the substantia nigra of Parkinson's and Alzheimer's disease brains. *Neurology* **38**, 1285-1291 (1988).

Lecours, C., Bordeleau, M., Cantin, L., Parent, M., Paolo, T.D. & Tremblay, M.E. Microglial Implication in Parkinson's Disease: Loss of Beneficial Physiological Roles or Gain of Inflammatory Functions? *Front. Cell. Neurosci.* **12**, 282 (2018).

Jack, C., Ruffini, F., Bar-Or, A. & Antel, J.P. Microglia and multiple sclerosis. *J. Neurosci. Res.* **81**, 363-373 (2005).

Xie, L., Mao, X., Jin, K. & Greenberg, D.A. Vascular endothelial growth factor-B expression in postischemic rat brain. *Vasc Cell* **5**, 8 (2013).

Lalancette-Hebert, M., Gowing, G., Simard, A., Weng, Y.C. & Kriz, J. Selective ablation of proliferating microglial cells exacerbates ischemic injury in the brain. *J. Neurosci.* **27**, 2596-2605 (2007).

Lambertsen, K.L., Biber, K. & Finsen, B. Inflammatory cytokines in experimental and human stroke. *J. Cereb. Blood Flow Metab.* **32**, 1677-1698 (2012).

Patel, A.R., Ritzel, R., McCullough, L.D. & Liu, F. Microglia and ischemic stroke: a double-edged sword. *Int. J. Physiol. Pathophysiol. Pharmacol.* **5**, 73-90 (2013).

Zhao, X., Eyo, U.B., Murugan, M. & Wu, L.J. Microglial interactions with the neurovascular system in physiology and pathology. *Dev. Neurobiol.* **78**, 604-617 (2018).

Zlokovic, B.V. The blood-brain barrier in health and chronic neurodegenerative disorders. *Neuron* **57**, 178-201 (2008).

Iadecola, C. Neurovascular regulation in the normal brain and in Alzheimer's disease. *Nat. Rev. Neurosci.* **5**, 347-360 (2004).

Hawkins, B.T. & Davis, T.P. The blood-brain barrier/neurovascular unit in health and

disease. *Pharmacol. Rev.* **57**, 173-185 (2005).

Banks, W.A., Gray, A.M., Erickson, M.A., Salameh, T.S., Damodarasamy, M., Sheibani, N., Meabon, J.S., Wing, E.E., Morofuji, Y., Cook, D.G. & Reed, M.J. Lipopolysaccharide-induced blood-brain barrier disruption: roles of cyclooxygenase, oxidative stress, neuroinflammation, and elements of the neurovascular unit. *J. Neuroinflammation* **12**, 223 (2015).

Abbott, N.J., Patabendige, A.A., Dolman, D.E., Yusof, S.R. & Begley, D.J. Structure and function of the blood-brain barrier. *Neurobiol. Dis.* **37**, 13-25 (2010).

Higashi, K., Fujita, A., Inanobe, A., Tanemoto, M., Doi, K., Kubo, T. & Kurachi, Y. An inwardly rectifying K(+) channel, Kir4.1, expressed in astrocytes surrounds synapses and blood vessels in brain. *Am. J. Physiol. Cell Physiol.* **281**, C922-931 (2001).

Mathiisen, T.M., Lehre, K.P., Danbolt, N.C. & Ottersen, O.P. The perivascular astroglial sheath provides a complete covering of the brain microvessels: an electron microscopic 3D reconstruction. *Glia* **58**, 1094-1103 (2010).

Korogod, N., Petersen, C.C. & Knott, G.W. Ultrastructural analysis of adult mouse neocortex comparing aldehyde perfusion with cryo fixation. *Elife* **4**(2015).

Ezan, P., Andre, P., Cisternino, S., Saubamea, B., Boulay, A.C., Doutremer, S., Thomas, M.A., Quenech'du, N., Giaume, C. & Cohen-Salmon, M. Deletion of astroglial connexins weakens the blood-brain barrier. *J. Cereb. Blood Flow Metab.* **32**, 1457-1467 (2012).

Nuriya, M., Shinotsuka, T. & Yasui, M. Diffusion properties of molecules at the blood-brain interface: potential contributions of astrocyte endfeet to diffusion barrier functions. *Cereb. Cortex* **23**, 2118-2126 (2013).

Horng, S., Therattil, A., Moyon, S., Gordon, A., Kim, K., Argaw, A.T., Hara, Y., Mariani, J.N., Sawai, S., Flodby, P., Crandall, E.D., Borok, Z., Sofroniew, M.V., Chapouly, C. & John, G.R. Astrocytic tight junctions control inflammatory CNS lesion pathogenesis. *J. Clin. Invest.* **127**, 3136-3151 (2017).

Dohgu, S., Takata, F., Yamauchi, A., Nakagawa, S., Egawa, T., Naito, M., Tsuruo, T., Sawada, Y., Niwa, M. & Kataoka, Y. Brain pericytes contribute to the induction and up-regulation of blood-brain barrier functions through transforming growth factor-beta production. *Brain Res.* **1038**, 208-215 (2005).

Armulik, A., Genove, G., Mae, M., Nisancioglu, M.H., Wallgard, E., Niaudet, C., He,

L., Norlin, J., Lindblom, P., Strittmatter, K., Johansson, B.R. & Betsholtz, C. Pericytes regulate the blood-brain barrier. *Nature* **468**, 557-561 (2010).

Lindahl, P., Johansson, B.R., Leveen, P. & Betsholtz, C. Pericyte loss and microaneurysm formation in PDGF-B-deficient mice. *Science* **277**, 242-245 (1997).

Daneman, R., Zhou, L., Kebede, A.A. & Barres, B.A. Pericytes are required for blood-brain barrier integrity during embryogenesis. *Nature* **468**, 562-566 (2010).

Nikolakopoulou, A.M., Montagne, A., Kisler, K., Dai, Z., Wang, Y., Huuskonen, M.T., Sagare, A.P., Lazic, D., Sweeney, M.D., Kong, P., Wang, M., Owens, N.C., Lawson, E.J., Xie, X., Zhao, Z. & Zlokovic, B.V. Pericyte loss leads to circulatory failure and pleiotrophin depletion causing neuron loss. *Nat. Neurosci.* **22**, 1089-1098 (2019).

Ryu, J.K. & McLarnon, J.G. Minocycline or iNOS inhibition block 3-nitrotyrosine increases and blood-brain barrier leakiness in amyloid beta-peptide-injected rat hippocampus. *Exp. Neurol.* **198**, 552-557 (2006).

Lou, N., Takano, T., Pei, Y., Xavier, A.L., Goldman, S.A. & Nedergaard, M. Purinergic receptor P2RY12-dependent microglial closure of the injured blood-brain barrier. *Proc. Natl. Acad. Sci. U. S. A.* **113**, 1074-1079 (2016).

Hanisch, U.K. & Kettenmann, H. Microglia: active sensor and versatile effector cells in the normal and pathologic brain. *Nat. Neurosci.* **10**, 1387-1394 (2007).

Wang, Y., Jin, S., Sonobe, Y., Cheng, Y., Horiuchi, H., Parajuli, B., Kawanokuchi, J., Mizuno, T., Takeuchi, H. & Suzumura, A. Interleukin-1beta induces blood-brain barrier disruption by downregulating Sonic hedgehog in astrocytes. *PLoS One* **9**, e110024 (2014).

Montagne, A., Barnes, S.R., Sweeney, M.D., Halliday, M.R., Sagare, A.P., Zhao, Z., Toga, A.W., Jacobs, R.E., Liu, C.Y., Amezcua, L., Harrington, M.G., Chui, H.C., Law, M. & Zlokovic, B.V. Blood-brain barrier breakdown in the aging human hippocampus. *Neuron* **85**, 296-302 (2015).

Giannoni, P., Arango-Lievano, M., Neves, I.D., Rousset, M.C., Baranger, K., Rivera, S., Jeanneteau, F., Claeysen, S. & Marchi, N. Cerebrovascular pathology during the progression of experimental Alzheimer's disease. *Neurobiol. Dis.* **88**, 107-117 (2016).

Kortekaas, R., Leenders, K.L., van Oostrom, J.C., Vaalburg, W., Bart, J., Willemsen,

A.T. & Hendrikse, N.H. Blood-brain barrier dysfunction in parkinsonian midbrain in vivo. *Ann. Neurol.* **57**, 176-179 (2005).

Jolivel, V., Bicker, F., Biname, F., Ploen, R., Keller, S., Gollan, R., Jurek, B., Birkenstock, J., Poisa-Beiro, L., Bruttger, J., Opitz, V., Thal, S.C., Waisman, A., Bauerle, T., Schafer, M.K., Zipp, F. & Schmidt, M.H.H. Perivascular microglia promote blood vessel disintegration in the ischemic penumbra. *Acta Neuropathol.* **129**, 279-295 (2015).

Starr, J.M., Wardlaw, J., Ferguson, K., MacLullich, A., Deary, I.J. & Marshall, I. Increased blood-brain barrier permeability in type II diabetes demonstrated by gadolinium magnetic resonance imaging. *J. Neurol. Neurosurg. Psychiatry* **74**, 70-76 (2003).

Dumitrescu, A.L. Depression and Inflammatory Periodontal Disease Considerations-An Interdisciplinary Approach. *Front. Psychol.* **7**, 347 (2016).

Danielski, L.G., Giustina, A.D., Badawy, M., Barichello, T., Quevedo, J., Dal-Pizzol, F. & Petronilho, F. Brain Barrier Breakdown as a Cause and Consequence of Neuroinflammation in Sepsis. *Mol. Neurobiol.* **55**, 1045-1053 (2018).

Stojanovich, L., Zandman-Goddard, G., Pavlovich, S. & Sikanich, N. Psychiatric manifestations in systemic lupus erythematosus. *Autoimmun Rev* **6**, 421-426 (2007).

Dema, B. & Charles, N. Autoantibodies in SLE: Specificities, Isotypes and Receptors. *Antibodies (Basel)* **5**(2016).

Kaul, A., Gordon, C., Crow, M.K., Touma, Z., Urowitz, M.B., van Vollenhoven, R., Ruiz-Irastorza, G. & Hughes, G. Systemic lupus erythematosus. *Nat Rev Dis Primers* **2**, 16039 (2016).

Popescu, A. & Kao, A.H. Neuropsychiatric systemic lupus erythematosus. *Curr. Neuropharmacol.* **9**, 449-457 (2011).

Ainiala, H., Loukkola, J., Peltola, J., Korpela, M. & Hietaharju, A. The prevalence of neuropsychiatric syndromes in systemic lupus erythematosus. *Neurology* **57**, 496-500 (2001).

Bialas, A.R., Presumey, J., Das, A., van der Poel, C.E., Lapchak, P.H., Mesin, L., Victora, G., Tsokos, G.C., Mawrin, C., Herbst, R. & Carroll, M.C. Microglia-dependent synapse loss in type I interferon-mediated lupus. *Nature* **546**, 539-543 (2017).

Nestor, J., Arinuma, Y., Huerta, T.S., Kowal, C., Nasiri, E., Kello, N., Fujieda, Y., Bialas, A., Hammond, T., Sriram, U., Stevens, B., Huerta, P.T., Volpe, B.T. & Diamond, B. Lupus antibodies induce behavioral changes mediated by microglia and blocked by ACE inhibitors. *J. Exp. Med.* **215**, 2554-2566 (2018).

Tanaka, K.F., Matsui, K., Sasaki, T., Sano, H., Sugio, S., Fan, K., Hen, R., Nakai, J., Yanagawa, Y., Hasuwa, H., Okabe, M., Deisseroth, K., Ikenaka, K. & Yamanaka, A. Expanding the repertoire of optogenetically targeted cells with an enhanced gene expression system. *Cell Rep* **2**, 397-406 (2012).

Stanger, B.Z., Tanaka, A.J. & Melton, D.A. Organ size is limited by the number of embryonic progenitor cells in the pancreas but not the liver. *Nature* **445**, 886-891 (2007).

Masamizu, Y., Tanaka, Y.R., Tanaka, Y.H., Hira, R., Ohkubo, F., Kitamura, K., Isomura, Y., Okada, T. & Matsuzaki, M. Two distinct layer-specific dynamics of cortical ensembles during learning of a motor task. *Nat. Neurosci.* **17**, 987-994 (2014).

Rosi, S., Pert, C.B., Ruff, M.R., McGann-Gramling, K. & Wenk, G.L. Chemokine receptor 5 antagonist D-Ala-peptide T-amide reduces microglia and astrocyte activation within the hippocampus in a neuroinflammatory rat model of Alzheimer's disease. *Neuroscience* **134**, 671-676 (2005).

Di Prisco, S., Summa, M., Chellakudam, V., Rossi, P.I. & Pittaluga, A. RANTES-mediated control of excitatory amino acid release in mouse spinal cord. *J. Neurochem.* **121**, 428-437 (2012).

Nikolakopoulou, A.M., Zhao, Z., Montagne, A. & Zlokovic, B.V. Regional early and progressive loss of brain pericytes but not vascular smooth muscle cells in adult mice with disrupted platelet-derived growth factor receptor-β signaling. *PLoS One* **12**, e0176225 (2017).

Thevenaz, P., Ruttimann, U.E. & Unser, M. A pyramid approach to subpixel registration based on intensity. *IEEE Trans Image Process* **7**, 27-41 (1998).

Bell, R.D., Winkler, E.A., Sagare, A.P., Singh, I., LaRue, B., Deane, R. & Zlokovic, B.V. Pericytes control key neurovascular functions and neuronal phenotype in the adult brain and during brain aging. *Neuron* **68**, 409-427 (2010).

Zhou, Y., Zhou, B., Pache, L., Chang, M., Khodabakhshi, A.H., Tanaseichuk, O., Benner, C. & Chanda, S.K. Metascape provides a biologist-oriented resource for the analysis of systems-level datasets. *Nature communications* **10**, 1523-1523

(2019).

Katoh, M., Wu, B., Nguyen, H.B., Thai, T.Q., Yamasaki, R., Lu, H., Rietsch, A.M., Zorlu, M.M., Shinozaki, Y., Saitoh, Y., Saitoh, S., Sakoh, T., Ikenaka, K., Koizumi, S., Ransohoff, R.M. & Ohno, N. Polymorphic regulation of mitochondrial fission and fusion modifies phenotypes of microglia in neuroinflammation. *Sci. Rep.* **7**, 4942 (2017).

Parajuli, L.K., Nakajima, C., Kulik, A., Matsui, K., Schneider, T., Shigemoto, R. & Fukazawa, Y. Quantitative regional and ultrastructural localization of the Ca(v)2.3 subunit of R-type calcium channel in mouse brain. *J. Neurosci.* **32**, 13555-13567 (2012).

Nguyen, H.B., Thai, T.Q., Saitoh, S., Wu, B., Saitoh, Y., Shimo, S., Fujitani, H., Otobe, H. & Ohno, N. Conductive resins improve charging and resolution of acquired images in electron microscopic volume imaging. *Sci. Rep.* **6**, 23721 (2016).

Alan, P., Sanford, L. P., and Henry, deF. The fine structure of the nervous system: The neurons and supporting cells. *Oxford University Press* (1991).

Assmann, J.C., Muller, K., Wenzel, J., Walther, T., Brands, J., Thornton, P., Allan, S.M. & Schwaninger, M. Isolation and Cultivation of Primary Brain Endothelial Cells from Adult Mice. *Bio Protoc* **7**, e2294 (2017).

Singh, V., Mitra, S., Sharma, A.K., Gera, R. & Ghosh, D. Isolation and characterization of microglia from adult mouse brain: selected applications for ex vivo evaluation of immunotoxicological alterations following in vivo xenobiotic exposure. *Chem. Res. Toxicol.* **27**, 895-903 (2014).

Tokizane, K., Konishi, H., Makide, K., Kawana, H., Nakamuta, S., Kaibuchi, K., Ohwada, T., Aoki, J. & Kiyama, H. Phospholipid localization implies microglial morphology and function via Cdc42 in vitro. *Glia* **65**, 740-755 (2017).

Davalos, D., Ryu, J.K., Merlini, M., Baeten, K.M., Le Moan, N., Petersen, M.A., Deerinck, T.J., Smirnoff, D.S., Bedard, C., Hakozaki, H., Gonias Murray, S., Ling, J.B., Lassmann, H., Degen, J.L., Ellisman, M.H. & Akassoglou, K. Fibrinogen-induced perivascular microglial clustering is required for the development of axonal damage in neuroinflammation. *Nat Commun* **3**, 1227 (2012).

El Khoury, J., Toft, M., Hickman, S.E., Means, T.K., Terada, K., Geula, C. & Luster, A.D. Ccr2 deficiency impairs microglial accumulation and accelerates

progression of Alzheimer-like disease. *Nat. Med.* **13**, 432-438 (2007).

Hoshiko, M., Arnoux, I., Avignone, E., Yamamoto, N. & Audinat, E. Deficiency of the microglial receptor CX3CR1 impairs postnatal functional development of thalamocortical synapses in the barrel cortex. *J. Neurosci.* **32**, 15106-15111 (2012).

Griffith, J.W., Sokol, C.L. & Luster, A.D. Chemokines and chemokine receptors: positioning cells for host defense and immunity. *Annu. Rev. Immunol.* **32**, 659-702 (2014).

Campbell, J.J. & Butcher, E.C. Chemokines in tissue-specific and microenvironment-specific lymphocyte homing. *Curr. Opin. Immunol.* **12**, 336-341 (2000).

Glass, W.G., Lim, J.K., Cholera, R., Pletnev, A.G., Gao, J.L. & Murphy, P.M. Chemokine receptor CCR5 promotes leukocyte trafficking to the brain and survival in West Nile virus infection. *J. Exp. Med.* **202**, 1087-1098 (2005).

Tyner, J.W., Uchida, O., Kajiwara, N., Kim, E.Y., Patel, A.C., O'Sullivan, M.P., Walter, M.J., Schwendener, R.A., Cook, D.N., Danoff, T.M. & Holtzman, M.J. CCL5-CCR5 interaction provides antiapoptotic signals for macrophage survival during viral infection. *Nat. Med.* **11**, 1180-1187 (2005).

Luther, S.A. & Cyster, J.G. Chemokines as regulators of T cell differentiation. *Nat. Immunol.* **2**, 102-107 (2001).

Cross, A.K. & Woodroofe, M.N. Chemokines induce migration and changes in actin polymerization in adult rat brain microglia and a human fetal microglial cell line in vitro. *J. Neurosci. Res.* **55**, 17-23 (1999).

Sorce, S., Myburgh, R. & Krause, K.H. The chemokine receptor CCR5 in the central nervous system. *Prog. Neurobiol.* **93**, 297-311 (2011).

Fragoso-Loyo, H., Richaud-Patin, Y., Orozco-Narvaez, A., Davila-Maldonado, L., Atisha-Fregoso, Y., Llorente, L. & Sanchez-Guerrero, J. Interleukin-6 and chemokines in the neuropsychiatric manifestations of systemic lupus erythematosus. *Arthritis Rheum.* **56**, 1242-1250 (2007).

Louboutin, J.P. & Strayer, D.S. Relationship between the chemokine receptor CCR5 and microglia in neurological disorders: consequences of targeting CCR5 on neuroinflammation, neuronal death and regeneration in a model of epilepsy. *CNS Neurol. Disord. Drug Targets* **12**, 815-829 (2013).

Furuse, M., Fujita, K., Hiiragi, T., Fujimoto, K. & Tsukita, S. Claudin-1 and -2: novel

integral membrane proteins localizing at tight junctions with no sequence similarity to occludin. *J. Cell Biol.* **141**, 1539-1550 (1998).

Van Itallie, C.M. & Anderson, J.M. The molecular physiology of tight junction pores. *Physiology (Bethesda)* **19**, 331-338 (2004).

Nitta, T., Hata, M., Gotoh, S., Seo, Y., Sasaki, H., Hashimoto, N., Furuse, M. & Tsukita, S. Size-selective loosening of the blood-brain barrier in claudin-5-deficient mice. *J. Cell Biol.* **161**, 653-660 (2003).

Blank, F., Wehrli, M., Lehmann, A., Baum, O., Gehr, P., von Garnier, C. & Rothen-Rutishauser, B.M. Macrophages and dendritic cells express tight junction proteins and exchange particles in an in vitro model of the human airway wall. *Immunobiology* **216**, 86-95 (2011).

Paul, D., Baena, V., Ge, S., Jiang, X., Jellison, E.R., Kiprono, T., Agalliu, D. & Pachter, J.S. Appearance of claudin-5(+) leukocytes in the central nervous system during neuroinflammation: a novel role for endothelial-derived extracellular vesicles. *J. Neuroinflammation* **13**, 292 (2016).

Culemann, S., Gruneboom, A., Nicolas-Avila, J.A., Weidner, D., Lammle, K.F., Rothe, T., Quintana, J.A., Kirchner, P., Krljanac, B., Eberhardt, M., Ferrazzi, F., Kretzschmar, E., Schicht, M., Fischer, K., Gelse, K., Faas, M., Pfeifle, R., Ackermann, J.A., Pachowsky, M., Renner, N., Simon, D., Haseloff, R.F., Ekici, A.B., Bauerle, T., Blasig, I.E., Vera, J., Voehringer, D., Kleyer, A., Paulsen, F., Schett, G., Hidalgo, A. & Kronke, G. Locally renewing resident synovial macrophages provide a protective barrier for the joint. *Nature* **572**, 670-675 (2019).

Zhang, Y., Chen, K., Sloan, S.A., Bennett, M.L., Scholze, A.R., O'Keeffe, S., Phatnani, H.P., Guarnieri, P., Caneda, C., Ruderisch, N., Deng, S., Liddelow, S.A., Zhang, C., Daneman, R., Maniatis, T., Barres, B.A. & Wu, J.Q. An RNA-sequencing transcriptome and splicing database of glia, neurons, and vascular cells of the cerebral cortex. *J. Neurosci.* **34**, 11929-11947 (2014).

Eng, C.L., Lawson, M., Zhu, Q., Dries, R., Koulena, N., Takei, Y., Yun, J., Cronin, C., Karp, C., Yuan, G.C. & Cai, L. Transcriptome-scale super-resolved imaging in tissues by RNA seqFISH. *Nature* **568**, 235-239 (2019).

Brockhaus, J., Moller, T. & Kettenmann, H. Phagocytozing ameboid microglial cells studied in a mouse corpus callosum slice preparation. *Glia* **16**, 81-90 (1996).

Neumann, H., Kotter, M.R. & Franklin, R.J. Debris clearance by microglia: an essential link between degeneration and regeneration. *Brain* **132**, 288-295 (2009).

Tanaka, T., Ueno, M. & Yamashita, T. Engulfment of axon debris by microglia requires p38 MAPK activity. *J. Biol. Chem.* **284**, 21626-21636 (2009).

Sierra, A., Encinas, J.M., Deudero, J.J., Chancey, J.H., Enikolopov, G., Overstreet-Wadiche, L.S., Tsirka, S.E. & Maletic-Savatic, M. Microglia shape adult hippocampal neurogenesis through apoptosis-coupled phagocytosis. *Cell Stem Cell* **7**, 483-495 (2010).

Krasemann, S., Madore, C., Cialic, R., Baufeld, C., Calcagno, N., El Fatimy, R., Beckers, L., O'Loughlin, E., Xu, Y., Fanek, Z., Greco, D.J., Smith, S.T., Tweet, G., Humulock, Z., Zrzavy, T., Conde-Sanroman, P., Gacias, M., Weng, Z., Chen, H., Tjon, E., Mazaheri, F., Hartmann, K., Madi, A., Ulrich, J.D., Glatzel, M., Worthmann, A., Heeren, J., Budnik, B., Lemere, C., Ikezu, T., Heppner, F.L., Litvak, V., Holtzman, D.M., Lassmann, H., Weiner, H.L., Ochando, J., Haass, C. & Butovsky, O. The TREM2-APOE Pathway Drives the Transcriptional Phenotype of Dysfunctional Microglia in Neurodegenerative Diseases. *Immunity* **47**, 566-581 e569 (2017).

Galloway, D.A., Phillips, A.E.M., Owen, D.R.J. & Moore, C.S. Phagocytosis in the Brain: Homeostasis and Disease. *Front. Immunol.* **10**, 790 (2019).

Durafourt, B.A., Moore, C.S., Zammit, D.A., Johnson, T.A., Zaguia, F., Guiot, M.C., Bar-Or, A. & Antel, J.P. Comparison of polarization properties of human adult microglia and blood-derived macrophages. *Glia* **60**, 717-727 (2012).

Neher, J.J., Emmrich, J.V., Fricker, M., Mander, P.K., Thery, C. & Brown, G.C. Phagocytosis executes delayed neuronal death after focal brain ischemia. *Proc. Natl. Acad. Sci. U. S. A.* **110**, E4098-4107 (2013).

Moller, T., Bard, F., Bhattacharya, A., Biber, K., Campbell, B., Dale, E., Eder, C., Gan, L., Garden, G.A., Hughes, Z.A., Pearse, D.D., Staal, R.G., Sayed, F.A., Wes, P.D. & Boddeke, H.W. Critical data-based re-evaluation of minocycline as a putative specific microglia inhibitor. *Glia* **64**, 1788-1794 (2016).

Yang, Y., Salayandia, V.M., Thompson, J.F., Yang, L.Y., Estrada, E.Y. & Yang, Y. Attenuation of acute stroke injury in rat brain by minocycline promotes blood-brain barrier remodeling and alternative microglia/macrophage activation during recovery. *J. Neuroinflammation* **12**, 26 (2015).

Yenari, M.A., Xu, L., Tang, X.N., Qiao, Y. & Giffard, R.G. Microglia potentiate damage to blood-brain barrier constituents: improvement by minocycline in vivo and in vitro. *Stroke* **37**, 1087-1093 (2006).

Dantzer, R., O'Connor, J.C., Freund, G.G., Johnson, R.W. & Kelley, K.W. From inflammation to sickness and depression: when the immune system subjugates the brain. *Nat. Rev. Neurosci.* **9**, 46-56 (2008).

Jeltsch-David, H. & Muller, S. Neuropsychiatric systemic lupus erythematosus and cognitive dysfunction: the MRL-lpr mouse strain as a model. *Autoimmun Rev* **13**, 963-973 (2014).

Capaldo, C.T. & Nusrat, A. Cytokine regulation of tight junctions. *Biochim. Biophys. Acta* **1788**, 864-871 (2009).

Wendeln, A.C., Degenhardt, K., Kaurani, L., Gertig, M., Ulas, T., Jain, G., Wagner, J., Hasler, L.M., Wild, K., Skodras, A., Blank, T., Staszewski, O., Datta, M., Centeno, T.P., Capece, V., Islam, M.R., Kerimoglu, C., Staufenbiel, M., Schultze, J.L., Beyer, M., Prinz, M., Jucker, M., Fischer, A. & Neher, J.J. Innate immune memory in the brain shapes neurological disease hallmarks. *Nature* **556**, 332-338 (2018).

Figure Legends

Figure 1

(a) Typical fluorescent images of IBA1 (microglia marker, green) and AQP4 (astrocyte end-feet marker as a marker of blood vessels, red) in WT mice and MRL/lpr mice. Magnified images show typical vessel-associated microglia and the vessels. Arrowheads indicate vessel-associated microglia. Scale bar: 50 μm or 10 μm (inset). (b, c) The graphs show the percentage of vessel-associated microglia (b) and the colocalization coefficiency (c). (d, e) The graphs show the density of total IBA1+ microglia (d) and parenchymal IBA1+ microglia (e). In all graphs, each point indicates averaged data from an individual animal, while columns and error bars show mean ± SD. N.S., not significant. $n = 5$ mice in each group. Unpaired *t*-test. $*P < 0.05$ and $**P < 0.01$.

Figure 2

(a) Observation scheme in the measurement of vascular permeability. To simultaneously detect leakage by size, fluorescence was separated using three color dyes. 70 kDa (Fluorescein, green), 40 kDa (Tetramethylrhodamine [TMR], yellow), and 10 kDa (TexasRed, red). The fluorescence signals were split into green, yellow, and red channels using dichroic mirrors (560 nm and 593 nm) and bandpass filtered (green, 500–550 nm; yellow, 563–588 nm; red, 601-657 nm). (b) Scheme of BBB permeability evaluation method. The 70 kDa image is displayed in green and the 40 and 10 kDa images are displayed in red using a pseudo color. The region of interest was taken outside the blood vessel (brain parenchyma), and the mean fluorescence intensity was measured to quantify the leakage and evaluate the BBB permeability.

Figure 3

(a) Typical examples of the image used for leakage evaluation. Scale bar: 50 μm. (b) The relative leakage was quantified by comparing mean fluorescence intensity in MRL/lpr mice with that in WT mice (normalized to 1.00). In all graphs, each point indicates averaged data from an individual animal, while columns and error bars show mean ± SD. $n = 6$ (70 kDa, 40 kDa), $n = 7$ (10 kDa) mice. Unpaired *t*-test. N.S., not significant. $*P < 0.05$.

Figure 4

(a) Typical images of *in vivo* imaging during systemic inflammation induced by LPS injection. Arrowheads indicate vessel-associated microglia. Scale bar: 50 μm. (b) Percentage of vessel-associated microglia to the total number of microglia. (c) Density of total microglia. In each graph the faint lines indicate data from an individual animal, while the dark lines and error bars indicate the mean ± SD. N.S., not significant. $n = 5$ mice in each group. Two-way repeated measures ANOVA, *post-hoc* Holm-Sidak multiple comparisons test. $***P < 0.001$.

Figure 5

(a) Typical images of *in vivo* verification of BBB permeability during systemic inflammation induced by LPS injection. Scale bar: 50 μm. (b) The graph shows of relative ratio of 10 kDa dextran permeability. The parenchymal mean fluorescent intensity of 10 kDa dextran in Day −7 was indexed as 1.00. (c) Permeability of the BBB in different size dextrans. In each graph the faint lines indicate data from an individual animal, while the dark lines and error bars indicate the mean ± SD. $n = 5$ mice in each group. Two-way repeated measures ANOVA, *post-hoc* Holm-Sidak multiple comparisons test. N.S., not significant. $*P < 0.05$, $**P < 0.01$ and $***P < 0.001$.

Figure 6

(a) Typical fluorescent images of Lectin (as a vessel marker) and Fibrin. Scale bar: 50 μm. (b) Comparison of Fibrin fluorescence intensity as a permeability evaluation. In all graphs, each point indicates averaged data from an individual animal, while columns and error bars show mean ± SD. $n = 5$ mice in each group. Unpaired *t*-test (left) and one-way repeated measures ANOVA, *post-hoc* Holm-Sidak multiple comparisons test (right). N.S., not significant.

Figure 7

(a) Percentage of vessel-associated microglia by single administration of LPS. (b) Change in permeability with a single dose of LPS injection. The parenchymal mean fluorescent intensity of 10 kDa dextran in Day −7 was indexed as 1.00. $n = 5$ mice in each group. In each graph the faint lines indicate data from an individual animal, while the dark lines and error bars indicate the mean ± SD. One-way repeated measures ANOVA, *post-hoc*

Holm-Sidak multiple comparisons test. N.S., not significant. ***$P < 0.001$.

Figure 8

(a) Skeletonized images of microglia from WT (left) and MRL/lpr mice (right) in parenchyma or associated with vessels. Scale bar: 50 μm. (b-d) The results of morphological analysis of microglia show the differences in the number of processes (b), total length (c) and cell body area (d). $n = 5$ mice in each group. In all graphs, each point indicates averaged data from an individual animal, while columns and error bars show mean ± SD. N.S., not significant. *$P < 0.05$, **$P < 0.01$ and ***$P < 0.001$. (e) Typical serial images of *in vivo* imaging of microglia and vessels during systemic inflammation induced by LPS injection. Scale bar: 50 μm. (f, g) The graphs show the average length of microglial processes and cell body area in LPS-injected mice. $n = 5$ mice in each group. In each graph the faint lines indicate data from an individual animal, while the dark lines and error bars indicate the mean ± SD. One-way repeated measures ANOVA, *post-hoc* Holm-Sidak multiple comparisons test. N.S., not significant. *$P < 0.05$, **$P < 0.01$ and ***$P < 0.001$.

Figure 9

(a) Co-staining images of TMEM119 (as a marker of brain resident microglia) and IBA1 in WT mice and MRL/lpr mice. Scale bar: 50 μm or 10 μm (inset). (b) Typical images of SALL1 (resident microglia marker) and IBA1 from LPS-injected mice and the density of each positive cell. Scale bar: 50 μm. $n = 5$ mice in each group. In all graphs, each point indicates averaged data from an individual animal, while columns and error bars show mean ± SD. Unpaired *t*-test. N.S., not significant. ***$P < 0.001$.

Figure 10

(a) Co-staining images of PDGFRβ (pericyte marker), AQP4 (vessel marker) and IBA1 (microglia marker). Scale bar: 50 μm. (b) Pericytes density counted by the number of PDGFRβ puncta positive cells. (c) Co-staining images of PDGFRβ (pericyte marker), lectin (vessel marker) and DAPI (nuclei). Scale bar: 50 μm. (d) Pericytes density counted by the number of PDGFRβ and DAPI double-positive cells. (e) The Graphs show PDGFRβ-positive pericyte coverage of lectin-positive vessels. In all graphs, each point indicates averaged data from an individual animal, while columns and error bars show

mean ± SD. n = 5 mice in each group. Unpaired t-test (WT vs MRL/lpr), and one-way repeated measures ANOVA, *post-hoc* Holm-Sidak multiple comparisons test (Pre, Day 1 and Day 7). N.S., not significant.

Figure 11

(a) Representative blot of cytokine array of supernatant from vascular endothelial cell culture treated with LPS or IFNα. (b) The top 21 cytokines that changed with the presence of LPS or IFNα, compared to control cells. CCL5 increased with both treatments. (c) Scheme of mouse experiments for intraventricular administration of inhibitor using cannula. (d) Typical images of microglia in LPS-injected mice under DAPTA administration. Scale bar: 50 μm. (e, f) Effect of DAPTA administration on microglia accumulation to the vessels (e), and BBB permeability in LPS-injected mice(f). (g, h) Effect of DAPTA administration on microglia accumulation to the vessels (g), and BBB permeability in IFNα-injected mice (h). In each graph the faint lines indicate data from an individual animal, while the dark lines and error bars indicate the mean ± SD. n = 5 mice in each group. Two-way repeated measures ANOVA, *post-hoc* Holm-Sidak multiple comparisons test. N.S., not significant. $*P < 0.05$, $**P < 0.01$ and $***P < 0.001$.

Figure 12

(a) Typical images of IBA1 positive cells and vessels after microglia ablation in Iba1-tTA::tetO-DTA mice. Scale bar: 50 μm. (b) Density of vessel-associated IBA1-positive cells and parenchymal IBA1-positive cells and density of brain parenchyma. n = 4 mice in each group. (c) Density of total microglia in Iba1-tTA::tetO-DTA mice. (d) Typical images of immunostaining with GFAP (astrocyte marker) under Dox-On or Dox-Off condition. Scale bar: 50 μm. (e) Activation of astrocytes compared with the fluorescence intensity of GFAP. n = 5 mice in each group. In all graphs, each point indicates averaged data from an individual animal, while columns and error bars show mean ± SD. Two-way repeated measures ANOVA, *post-hoc* Holm-Sidak multiple comparisons test (b), and unpaired t-test (c, e, f). N.S., not significant. $*P < 0.05$ and $**P < 0.01$. (f) BBB permeability without LPS injection in microglia ablated mice. n = 4 mice in each group. Faint lines indicate data from an individual animal, while the dark lines and error bars indicate the mean ± SD.

Figure 13

(a) Typical serial images of dextran leakage in LPS-injected mice after microglia ablation in Iba1-tTA::tetO-DTA mice. Scale bar: 50 μm. (b) The graph shows changes of BBB permeability during systemic inflammation induced by daily LPS injection. Faint lines indicate data from an individual animal, while the dark lines and error bars indicate the mean ± SD. n = 6 mice in each group. Two-way repeated measures ANOVA, *post-hoc* Holm-Sidak multiple comparisons test. N.S., not significant. *$P < 0.05$ and ***$P < 0.001$.

Figure 14

(a) Cluster analysis of microarray data from microglia. Numerous genes were upregulated in MRL/lpr mice, those involved in immune responses, cell adhesion and phagocytosis. (b) Result of Gene Ontology (GO) analysis. The focused clusters are highlighted in red.

Figure 15

(a) Typical images and orthogonal view of immunostaining with CLDN5. Scale bar: 50 μm or 10 μm (orthogonal view). (b) The percentage of CLDN5-positive microglia. Left: Comparison of colocalization coefficiency of CLDN5-IBA1. Right: The percentage of CLDN5-positive microglia. (c) Comparison of colocalization rates with endothelial cell marker (CD31) and IBA1. In all graphs, each point indicates averaged data from an individual animal, while columns and error bars show mean ± SD. n = 5 mice in each group. Two-way repeated measures ANOVA, *post-hoc* Holm-Sidak multiple comparisons test (b), and unpaired t-test (c). N.S., not significant. *$P < 0.05$, **$P < 0.01$ and ***$P < 0.001$.

Figure 16

(a) Typical images of immunostaining with CD68 in MRL/lpr mice. Scale bar: 10 μm. (b) Graph shows the number of CD68-pisitive microglia. The cells included two or more CD68-positive puncta were counted as positive cells. Each point indicates averaged data from an individual animal, while columns and error bars show mean ± SD. n = 6 mice in each group. Two-way repeated measures ANOVA, *post-hoc* Holm-Sidak multiple comparisons test. N.S., not significant. *$P < 0.05$ and **$P < 0.01$. (c, d) Correlation of fluorescence intensity of CD68 and CLDN5 (c). Each point represents a single cell. Correlation of fluorescence intensity of CD68 and IBA1 (d). Each point represents a

single cell.

Figure 17

(a) Typical images of coimmunostaining with CLDN5, IBA1 and AQP4 in LPS-injected mice. Arrowheads indicate CLDN5-positive microglia. Scale bar: 50 μm or 10 μm (inset). (b) The percentage of CLDN5-positive microglia. In all graphs, each point indicates averaged data from an individual animal, while columns and error bars show mean ± SD. Two-way repeated measures ANOVA, *post-hoc* Holm-Sidak multiple comparisons test. $n = 5$ mice in each group. N.S., not significant. $^{**}P < 0.01$ and $^{***}P < 0.001$.

Figure 18

(a) Typical images of coimmunostaining with CLDN5, IBA1 and endothelial cell marker CD31 in LPS-injected mice. Scale bar: 10 μm. (b) Comparison of colocalization coefficiency with CD31 and CLDN5 (left), or IBA1 and CLDN5 (right). In all graphs, each point indicates averaged data from an individual animal, while columns and error bars show mean ± SD. $n = 5$ mice in each group. One-way repeated measures ANOVA, *post-hoc* Holm-Sidak multiple comparisons test. N.S., not significant. $^{**}P < 0.01$ and $^{***}P < 0.001$.

Figure 19

(a) Gating strategy for flow cytometry analysis to verify CLDN5 expression in microglia and vascular endothelial cells. (b) The percentage of CLDN5-positive microglia. $n = 7$ mice in each group. (c) The percentage of CLDN5 high endothelial cells. $n = 6$ mice in each group. In all graphs, each point indicates averaged data from an individual animal, while columns and error bars show mean ± SD. One-way repeated measures ANOVA, *post-hoc* Holm-Sidak multiple comparisons test. N.S., not significant. $^{*}P < 0.05$ and $^{**}P < 0.01$.

Figure 20

A series of representative images of electron microscope observation with CLDN5 immunostaining in the MRL/lpr mouse. Left column shows raw images, center column shows color-coded components and the right column shows 3D reconstruction, of the 1st, 20th and 35th serial sections. A microglial cell (green) adhering the surface of the

basement membrane (BM, orange-yellow) has small processes that penetrate the BM to form immunoreactive contacts (arrowheads) with endothelial cells (pink), which resemble the immune-reactive contact between endothelial cells (arrows, tight junctions). The 3D reconstruction illustrates protrusions through the BM (center) and the endothelial cell contacts (lower panel, red). Arrows indicate CLDN5 signal of vascular endothelial cells. The arrowheads indicate the CLDN5 signal of microglia. Scale bar: 1 μm.

Figure 21

(a) The quantitative analysis of Cldn5 expression level by real-time PCR. $n = 5$ mice in each group. (b) The Cldn5 expression in cultured microglia stimulated by CCL5. (c) The Ccr5 expression in cultured microglia. (d) The purity of CD11b-positive microglia in adult brain derived culture. $n = 4$ cultures in each group. In all graphs, each point indicates averaged data from an individual animal, while columns and error bars show mean ± SD. One-way repeated measures ANOVA, *post-hoc* Holm-Sidak multiple comparisons test (a, c), and unpaired *t*-test (b). N.S., not significant. $*P < 0.05$, $**P < 0.01$ and $***P < 0.001$.

Figure 22

(a) Typical images of immunostaining with CD68 in LPS-injected mice. Scale bar: 50 μm or 10 μm (inset). (b) Temporal changes in the percentage of CD68-positive microglia. $n = 4$ mice in each group. (c) Typical image of CD68-positive phagocytic vesicles with AQP4 inclusion. Scale bar: 10 μm or 3 μm (inset). (d) Temporal changes in the percentage of microglia with AQP4 inclusion during daily LPS stimulation. $n = 9$ mice in each group. In all graphs, each point indicates averaged data from an individual animal, while columns and error bars show mean ± SD. Two-way repeated measures ANOVA, *post-hoc* Holm-Sidak multiple comparisons test (b), and One-way repeated measures ANOVA, *post-hoc* Holm-Sidak multiple comparisons test (d). N.S., not significant. $*P < 0.05$, $**P < 0.01$ and $***P < 0.001$.

Figure 23

A series of representative images of electron microscope observation with AQP4 immunostaining in the MRL/lpr mouse. Left column shows raw images (insets show magnified immunopositive segments), and the center column shows color-coded components while the right column shows 3D reconstruction. The arrowheads indicate

the AQP4 signal of astrocyte end-feet surrounding vessels. Arrows indicate AQP4 signal in microglial phagosome. Scale bar: 2 μm.

Figure 24

(a) Typical images of immunostaining with CD68 after direct administration of IFNα or saline to the brain parenchyma. Scale bar: 50 μm. (b) The percentage of CD68-positive microglia. In all graphs, each point indicates averaged data from an individual animal, while columns and error bars show mean ± SD. $n = 5$ mice in each group. Unpaired *t*-test. $^{**}P < 0.01$.

Figure 25

(a) Minocycline administration schedule. (b) Results of microglial morphology analysis by *in vivo* imaging under minocycline administration. Temporal changes in the average length of processes from the cell body (left) and the changes in cell body area (right). (c) Representative images of *in vivo* imaging of microglia in the LPS-injected mice with or without minocycline treatment. Graph shows temporal changes in the percentage of vessel-associated microglia. Scale bar: 50 μm or 10 μm (inset). (d) Typical images of leakage evaluation under minocycline administration. Graph shows temporal changes of BBB permeability. Scale bar: 50 μm. In each graph the faint lines indicate data from an individual animal, while the dark lines and error bars indicate the mean ± SD. $n = 5$ mice in each group. Two-way repeated measures ANOVA, *post-hoc* Holm-Sidak multiple comparisons test. N.S., not significant. $^{*}P < 0.05$, $^{**}P < 0.01$ and $^{***}P < 0.001$.

Figure 26

(a) Temporal changes of the average length of processes from the cell body after minocycline administration alone (without LPS stimulation). (b) Temporal changes of cell body area. (c) Temporal changes of the percentage of vessel-associated microglia. (d) Temporal changes of BBB permeability. In each graph the faint lines indicate data from an individual animal, while the dark lines and error bars indicate the mean ± SD. $n = 5$ mice in each group.

Figure 1

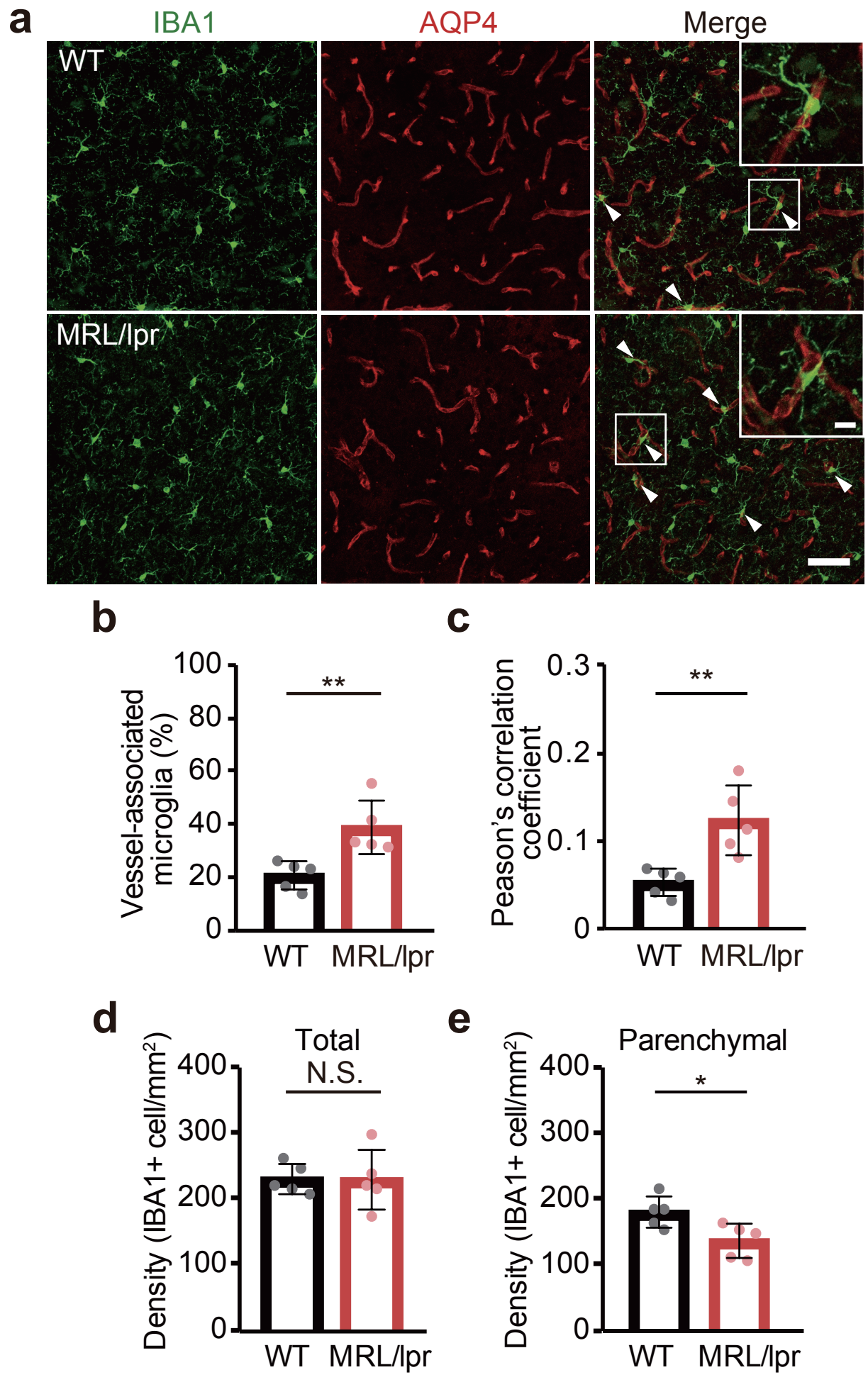
a
IBA1
AQP4
Merge
WT
MRL/lpr
b
Vessel-associated microglia (%)
100
80
60
40
20
0
**
WT
MRL/lpr
c
Peason's correlation coefficient
0.3
0.2
0.1
0
**
WT
MRL/lpr
d
Total
N.S.
Density (IBA1+ cell/mm²)
400
300
200
100
0
WT
MRL/lpr
e
Parenchymal
*
Density (IBA1+ cell/mm²)
400
300
200
100
0
WT
MRL/lpr

Figure 2

a Experimental paradigm for visualizing defferent-sized dextrans.

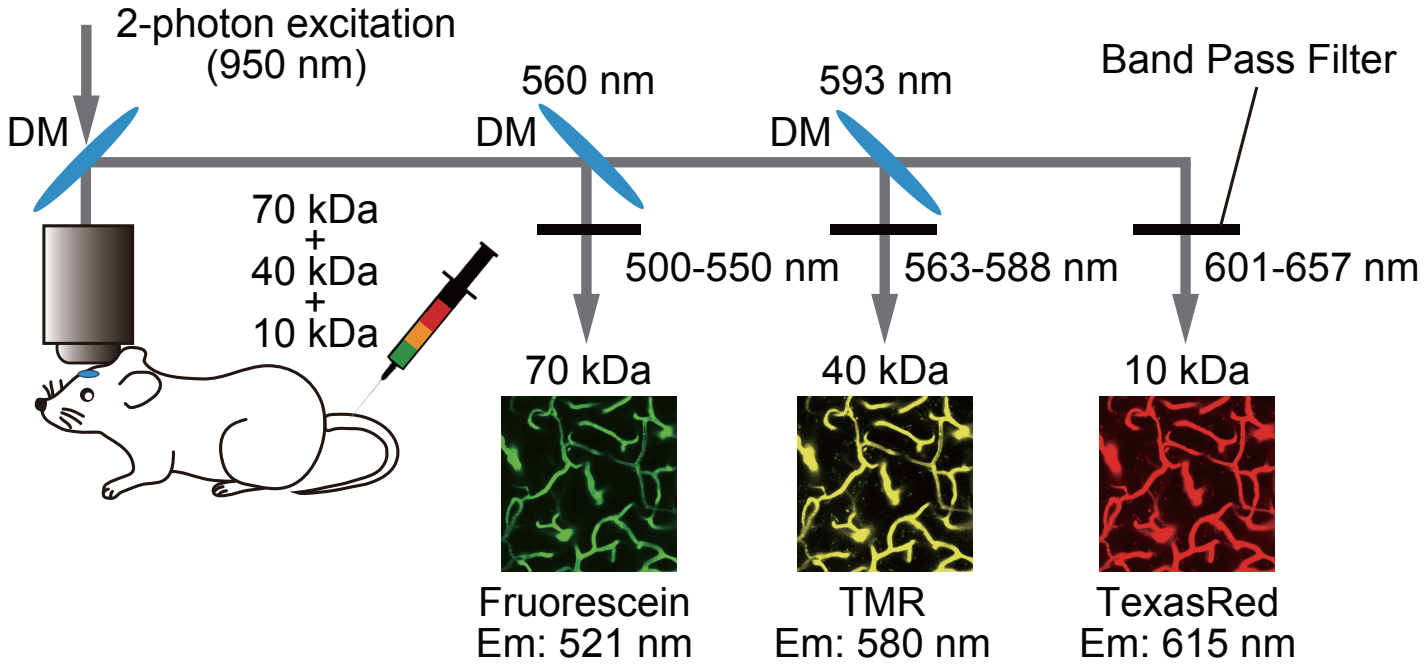

b

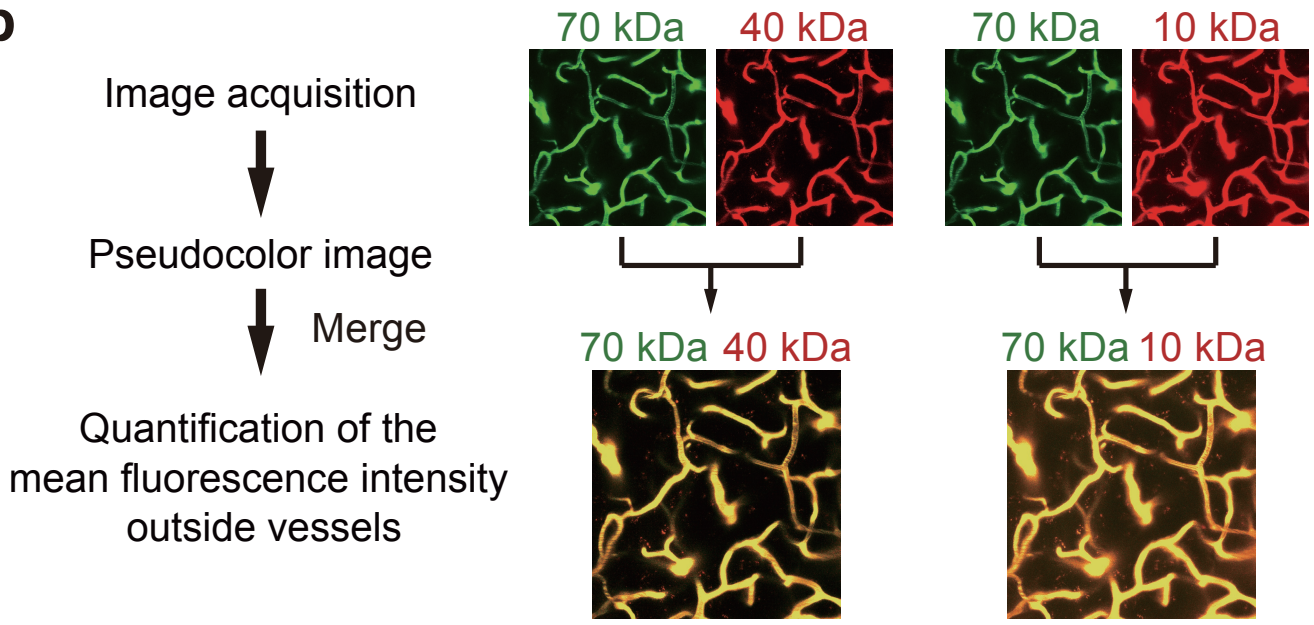

Figure 3

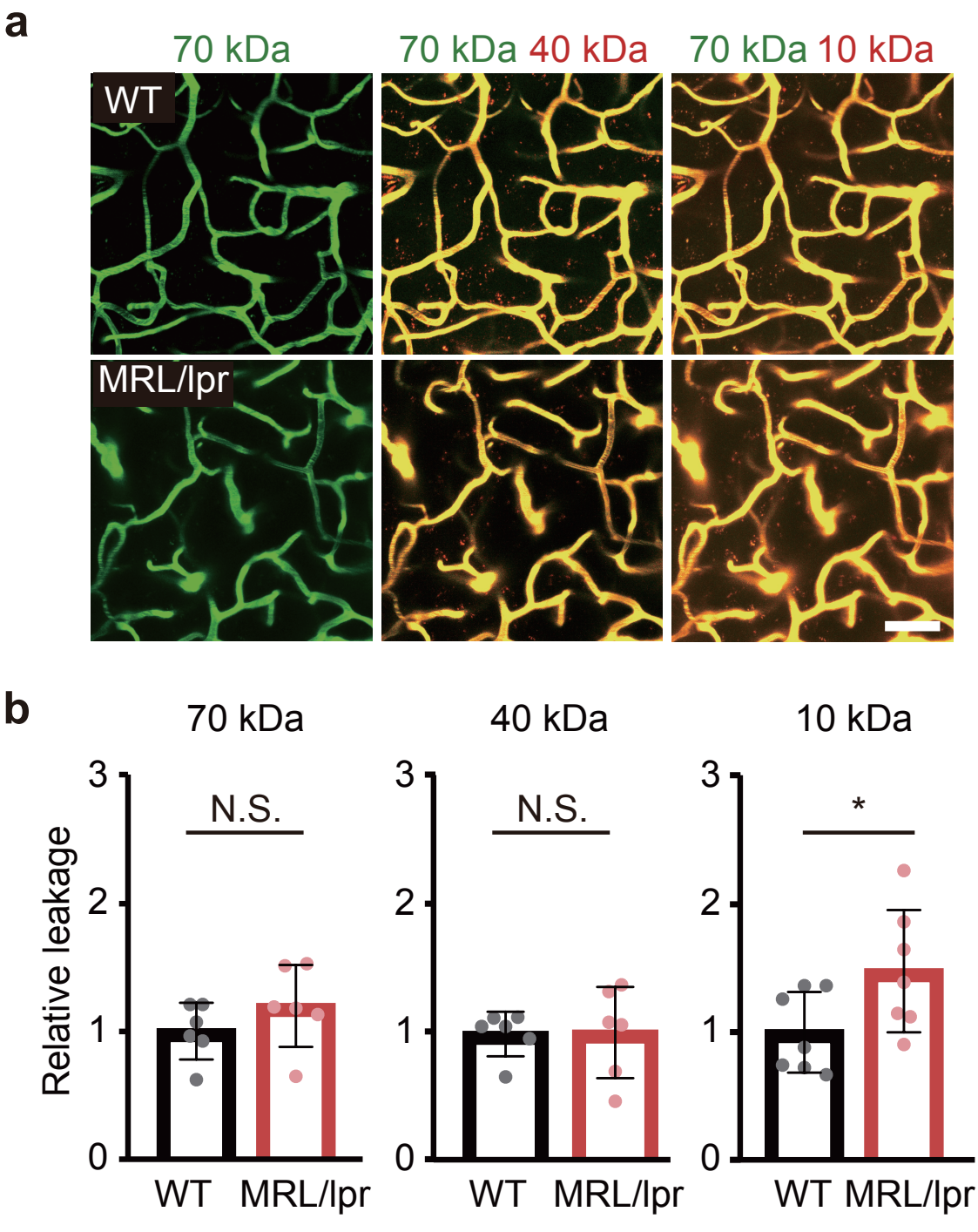
a
70 kDa
70 kDa 40 kDa
70 kDa 10 kDa
WT
MRL/lpr
b
70 kDa
40 kDa
10 kDa
Relative leakage
N.S.
N.S.
*
0
1
2
3
WT
MRL/lpr

Figure 4

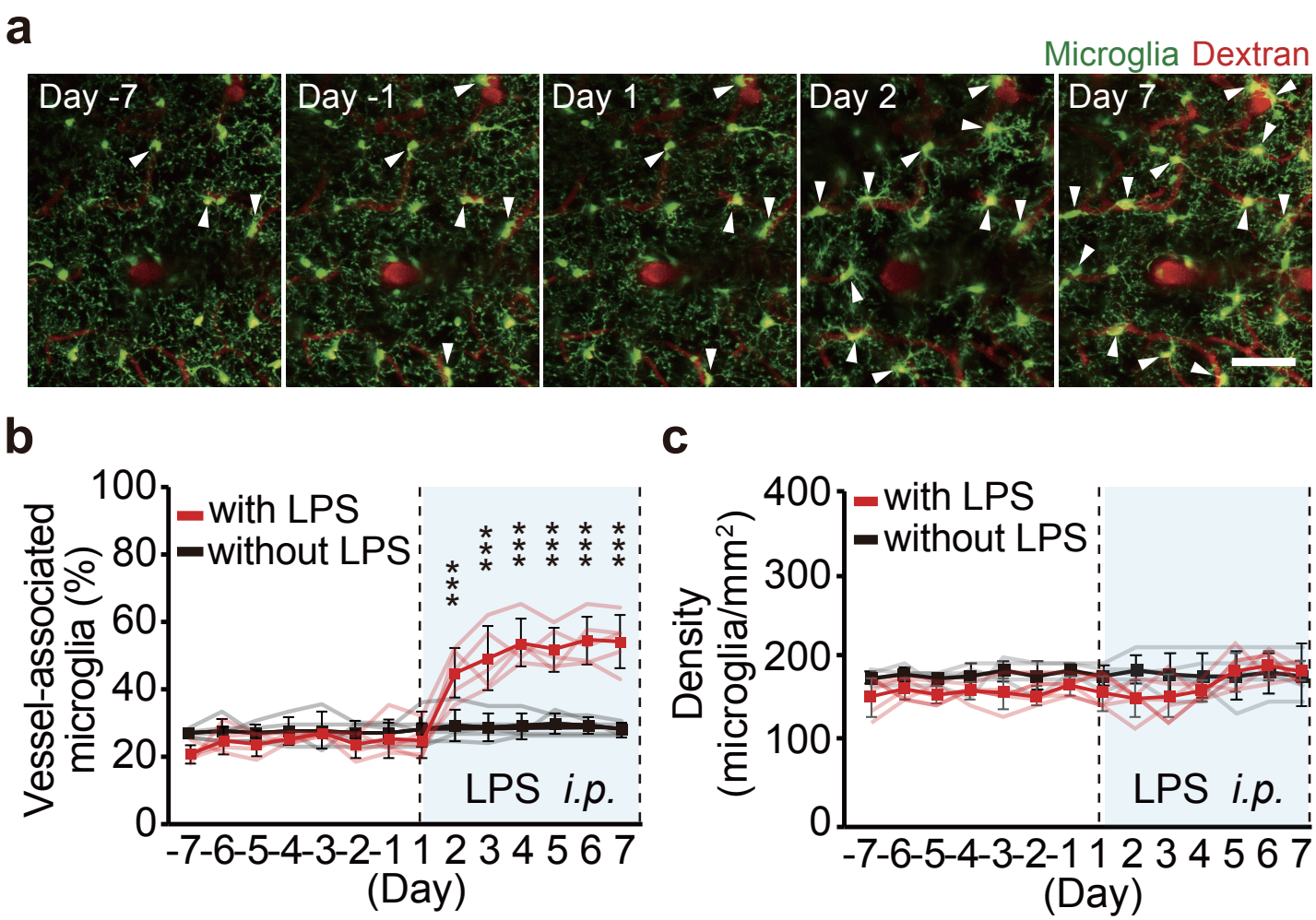
a
Microglia Dextran
Day -7
Day -1
Day 1
Day 2
Day 7
b
Vessel-associated microglia (%)
with LPS
without LPS
LPS i.p.
(Day)
c
Density (microglia/mm²)
with LPS
without LPS
LPS i.p.
(Day)

Figure 5

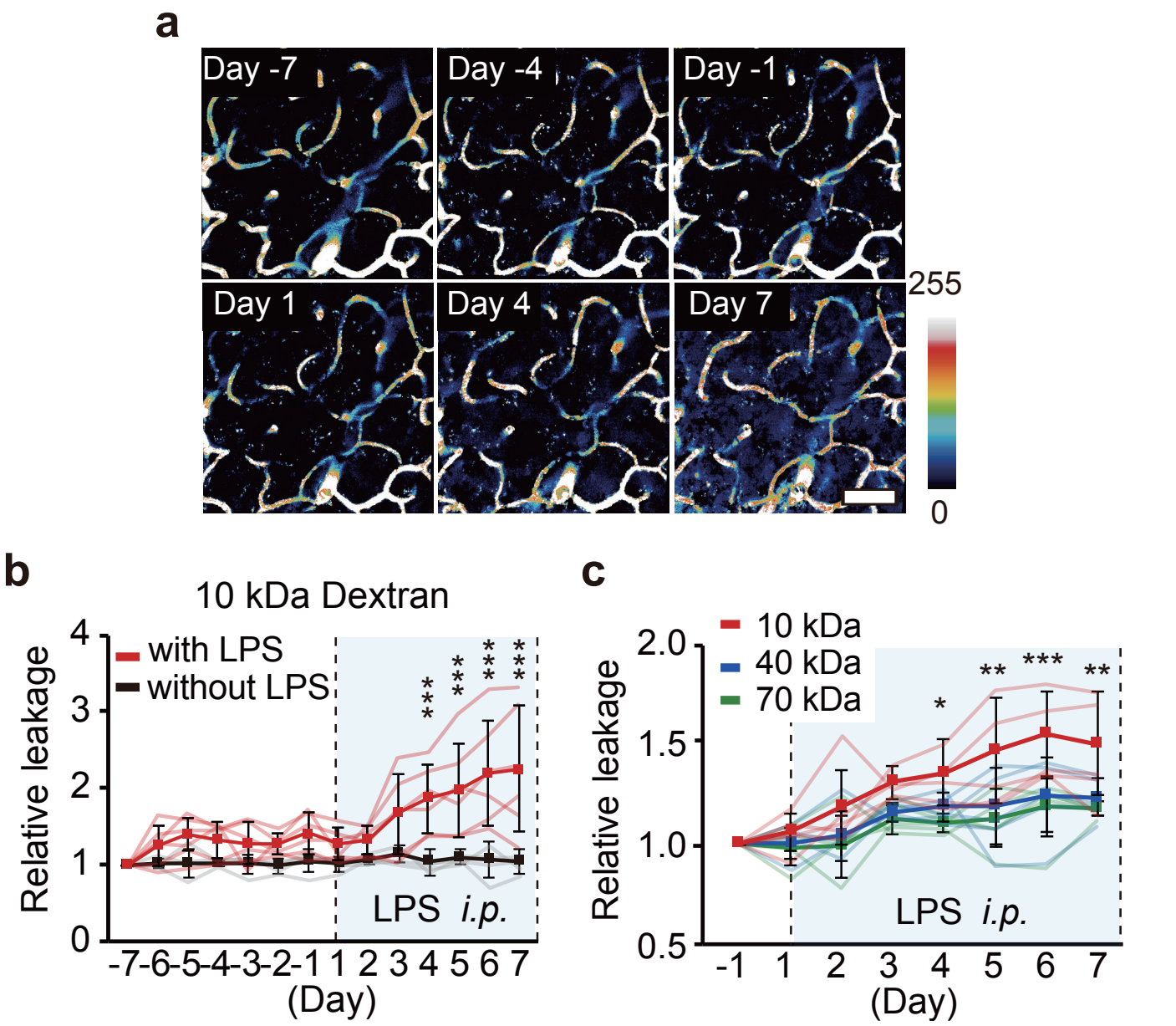
a
Day -7
Day -4
Day -1
Day 1
Day 4
Day 7
255
0
b
10 kDa Dextran
with LPS
without LPS
Relative leakage
LPS i.p.
(Day)
c
10 kDa
40 kDa
70 kDa
Relative leakage
LPS i.p.
(Day)

Figure 6

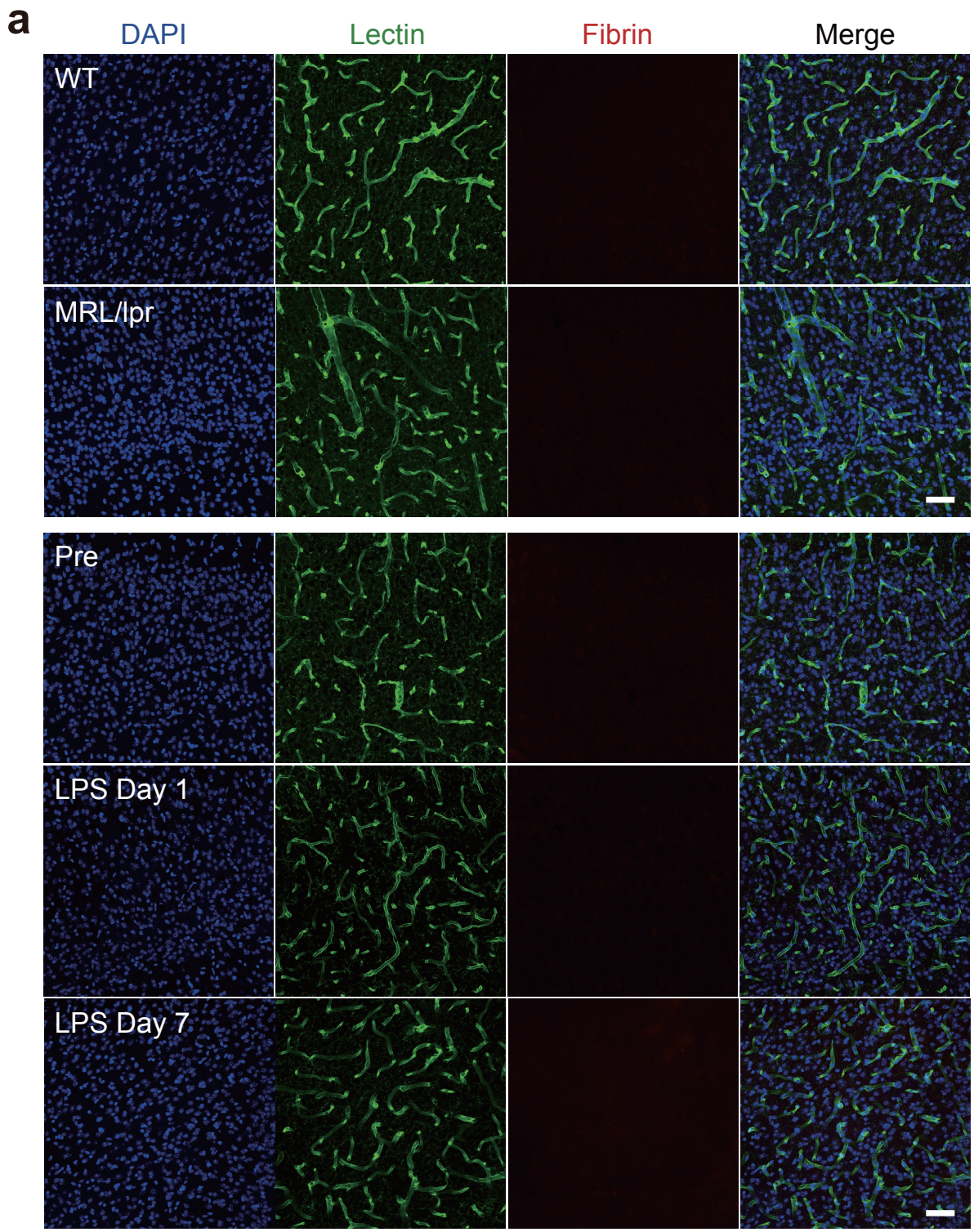
a
DAPI
Lectin
Fibrin
Merge
WT
MRL/lpr
Pre
LPS Day 1
LPS Day 7
b
Fibrin
(Integrated density x 10^3)
100
75
50
25
0
N.S.
N.S.
N.S.
WT
MRL/lpr
Pre
Day 1
Day 7

Figure 7

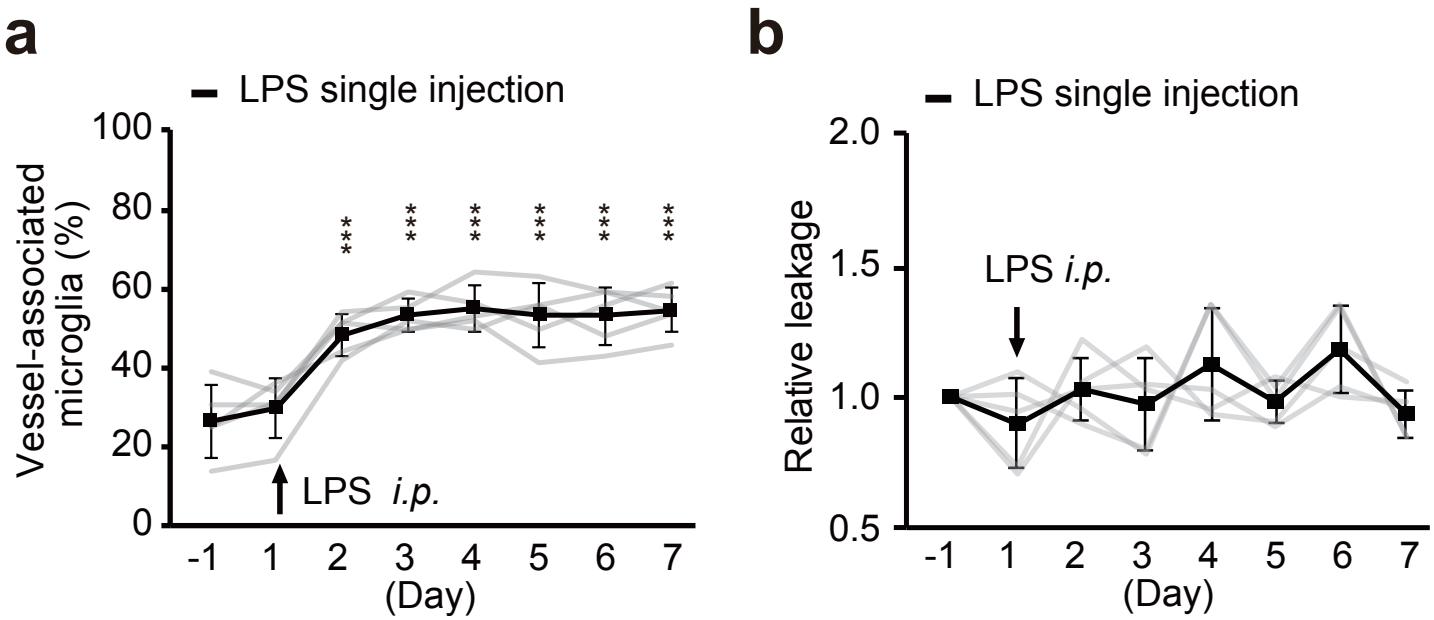
a
LPS single injection
Vessel-associated microglia (%)
100
80
60
40
20
0
***
***
***
***
***
***
LPS i.p.
-1
1
2
3
4
5
6
7
(Day)
b
LPS single injection
Relative leakage
2.0
1.5
1.0
0.5
LPS i.p.
-1
1
2
3
4
5
6
7
(Day)

Figure 8

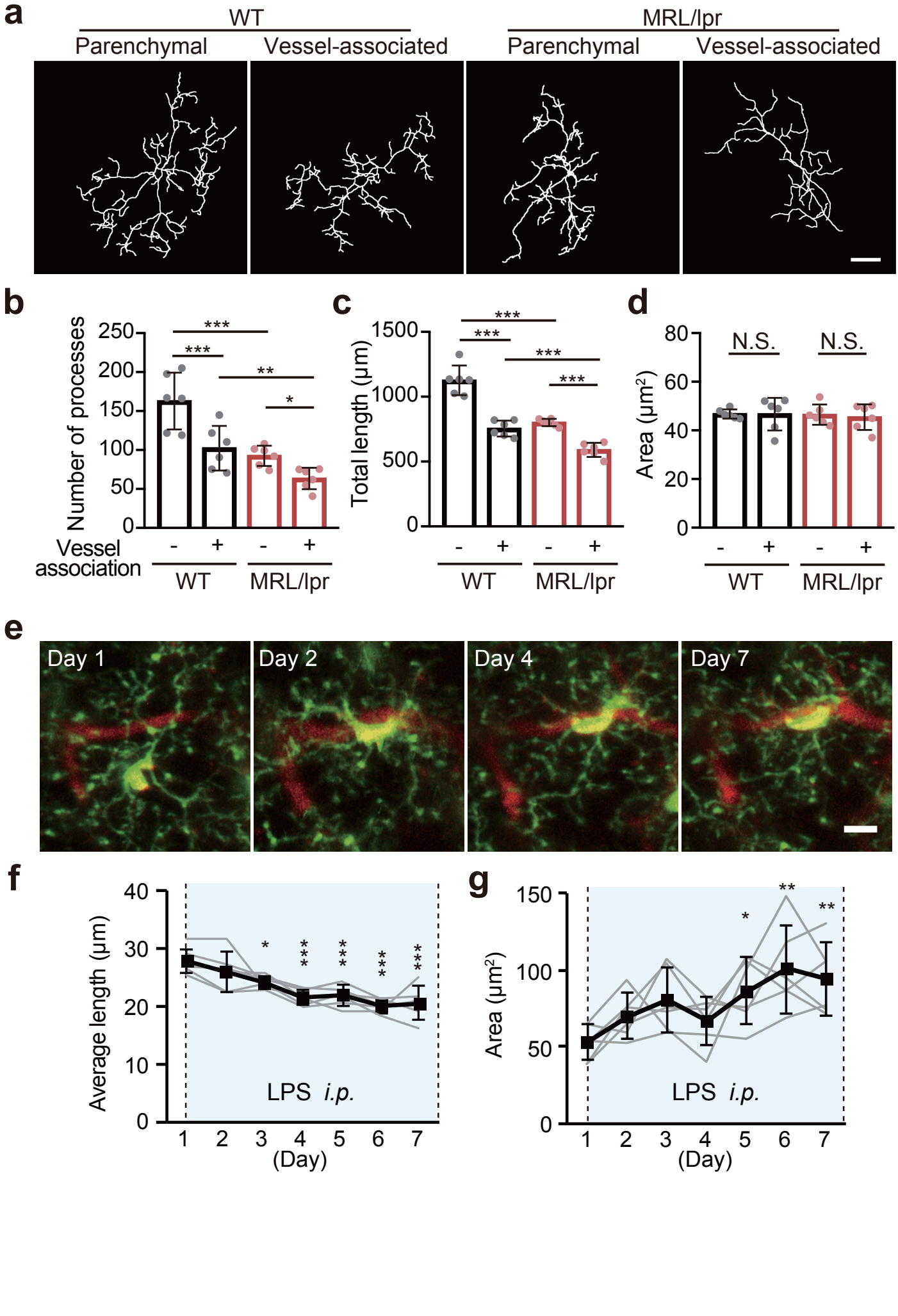
a
WT
MRL/lpr
Parenchymal
Vessel-associated
Parenchymal
Vessel-associated
b
Number of processes
250
200
150
100
50
0
***
***
**
*
Vessel association
-
+
-
+
WT
MRL/lpr
c
Total length (μm)
1500
1000
500
0
***
***
***
***
-
+
-
+
WT
MRL/lpr
d
Area (μm²)
80
60
40
20
0
N.S.
N.S.
-
+
-
+
WT
MRL/lpr
e
Day 1
Day 2
Day 4
Day 7
f
Average length (μm)
40
30
20
10
0
*
***
***
***
***
LPS i.p.
1
2
3
4
5
6
7
(Day)
g
Area (μm²)
150
100
50
0
*
**
**
LPS i.p.
1
2
3
4
5
6
7
(Day)

Figure 9

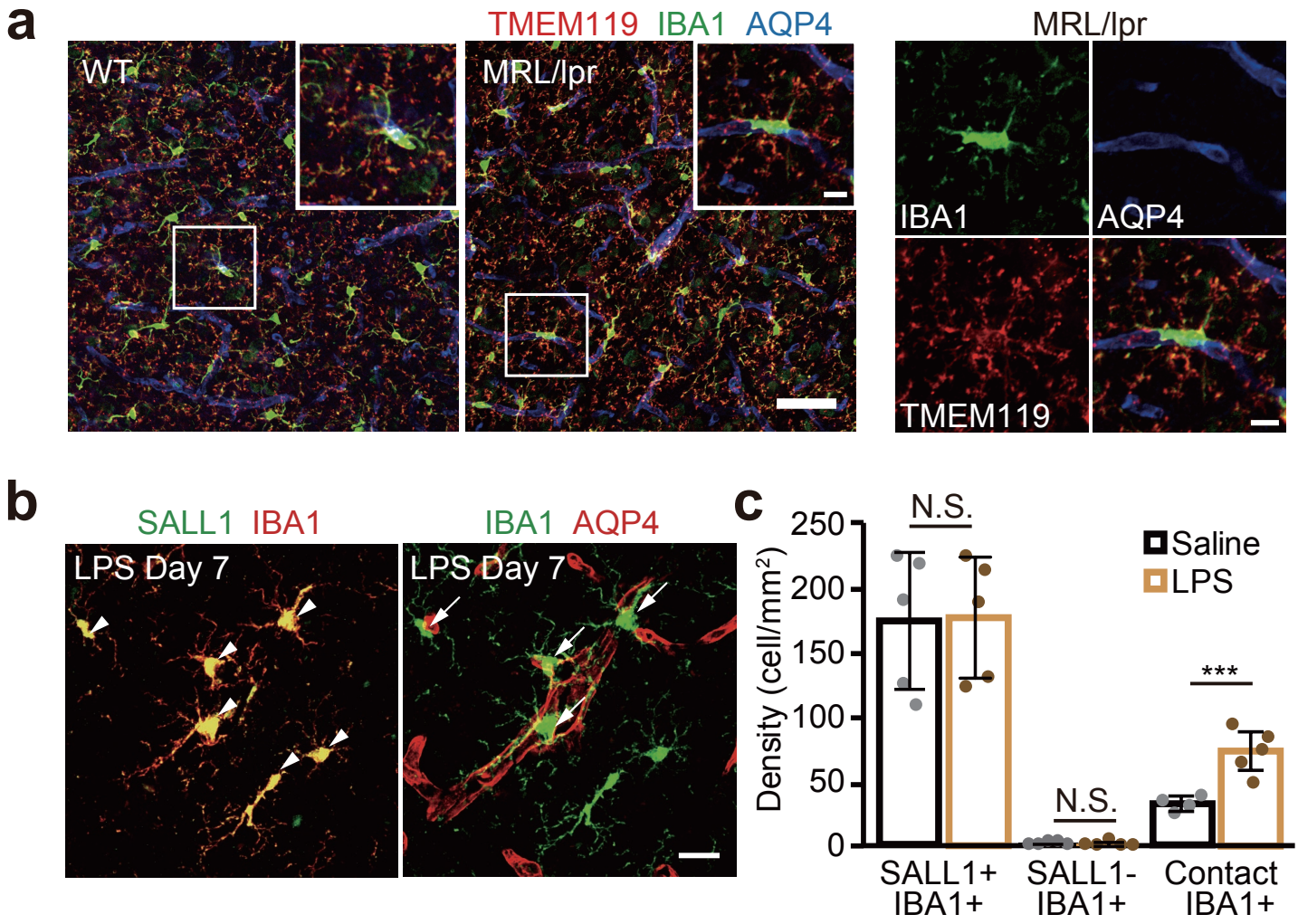
a
TMEM119 IBA1 AQP4
WT
MRL/lpr
MRL/lpr
IBA1
AQP4
TMEM119
b
SALL1 IBA1
IBA1 AQP4
LPS Day 7
LPS Day 7
c
N.S.
Saline
LPS
***
N.S.
Density (cell/mm²)
250
200
150
100
50
0
SALL1+ IBA1+
SALL1- IBA1+
Contact IBA1+

Figure 10

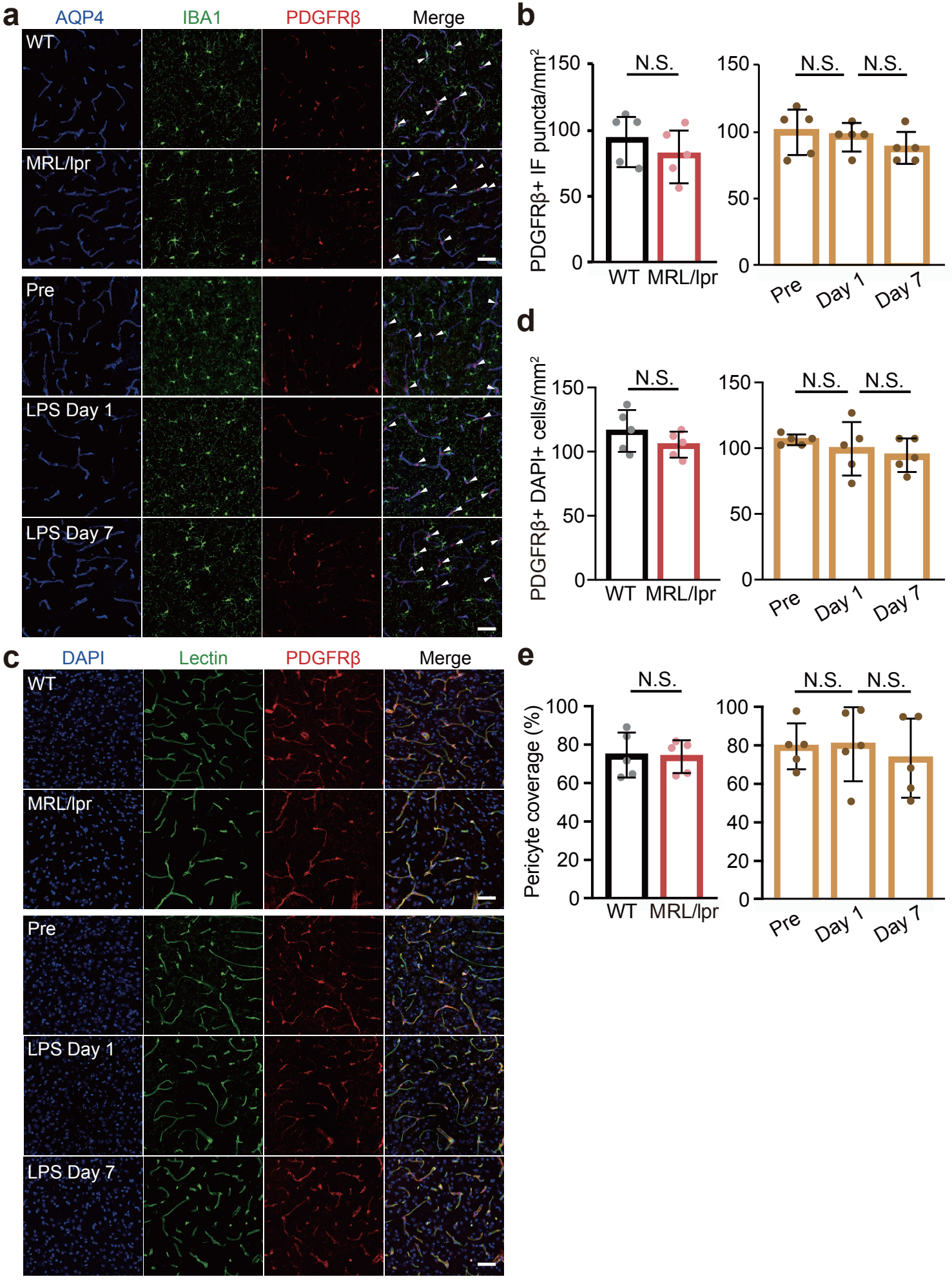
a
AQP4
IBA1
PDGFRβ
Merge
WT
MRL/lpr
Pre
LPS Day 1
LPS Day 7
b
PDGFRβ+ IF puncta/mm²
150
100
50
0
N.S.
WT
MRL/lpr
Pre
Day 1
Day 7
c
DAPI
Lectin
PDGFRβ
Merge
WT
MRL/lpr
Pre
LPS Day 1
LPS Day 7
d
PDGFRβ+ DAPI+ cells/mm²
e
Pericyte coverage (%)
100
80
60
40
20
0

Figure 11

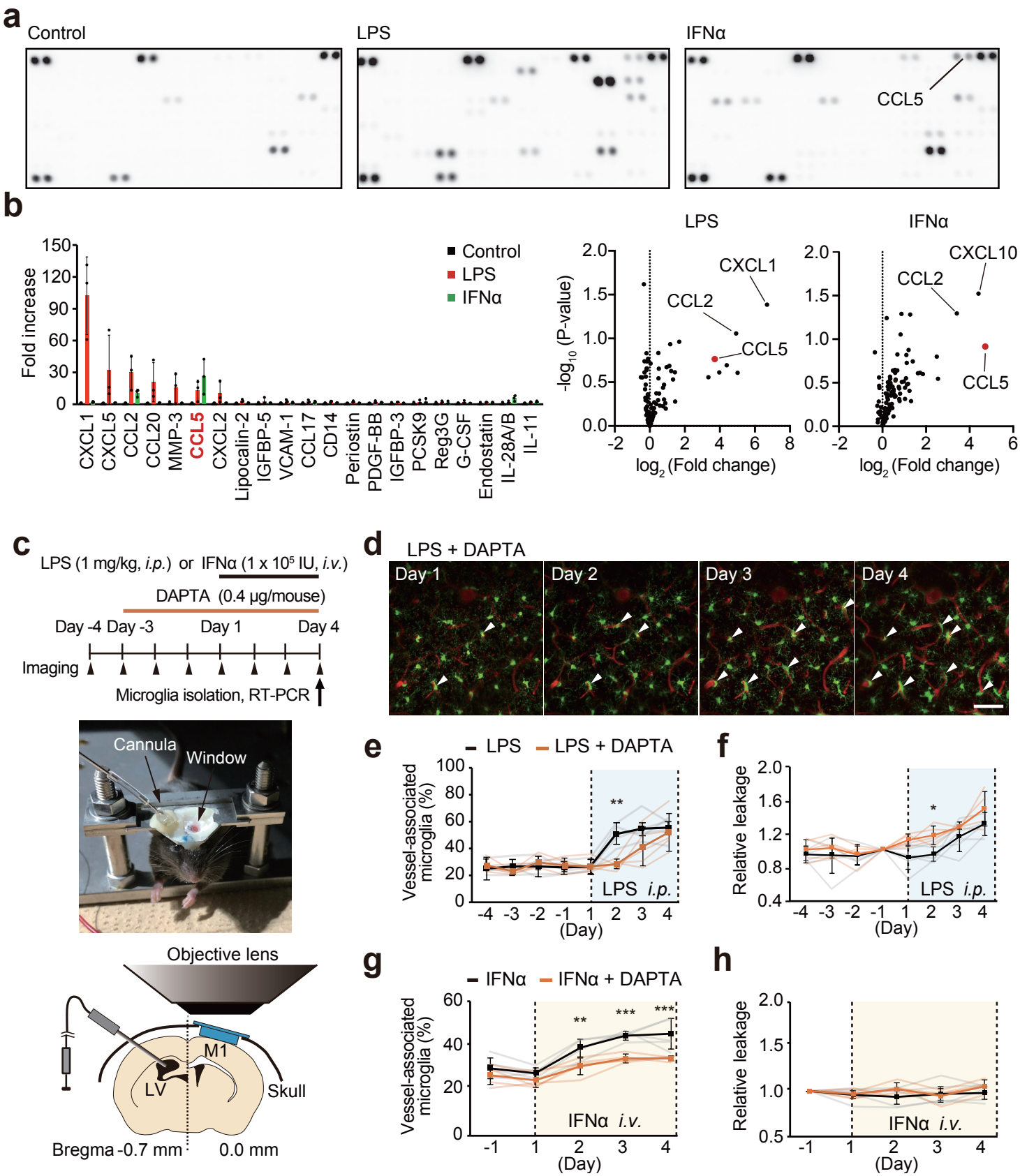
a
Control
LPS
IFNα
CCL5
b
Fold increase
Control
LPS
IFNα
CXCL1
CXCL5
CCL2
CCL20
MMP-3
CCL5
CXCL2
Lipocalin-2
IGFBP-5
VCAM-1
CCL17
CD14
Periostin
PDGF-BB
IGFBP-3
PCSK9
Reg3G
G-CSF
Endostatin
IL-28A/B
IL-11
LPS
IFNα
-log10 (P-value)
log2 (Fold change)
CXCL1
CCL2
CCL5
CXCL10
c
LPS (1 mg/kg, i.p.) or IFNα (1 x 10^5 IU, i.v.)
DAPTA (0.4 μg/mouse)
Day -4 Day -3 Day 1 Day 4
Imaging
Microglia isolation, RT-PCR
Cannula
Window
Objective lens
M1
LV
Skull
Bregma -0.7 mm
0.0 mm
d
LPS + DAPTA
Day 1
Day 2
Day 3
Day 4
e
LPS
LPS + DAPTA
Vessel-associated microglia (%)
LPS i.p.
(Day)
f
Relative leakage
LPS i.p.
(Day)
g
IFNα
IFNα + DAPTA
Vessel-associated microglia (%)
IFNα i.v.
(Day)
h
Relative leakage
IFNα i.v.
(Day)

Figure 12

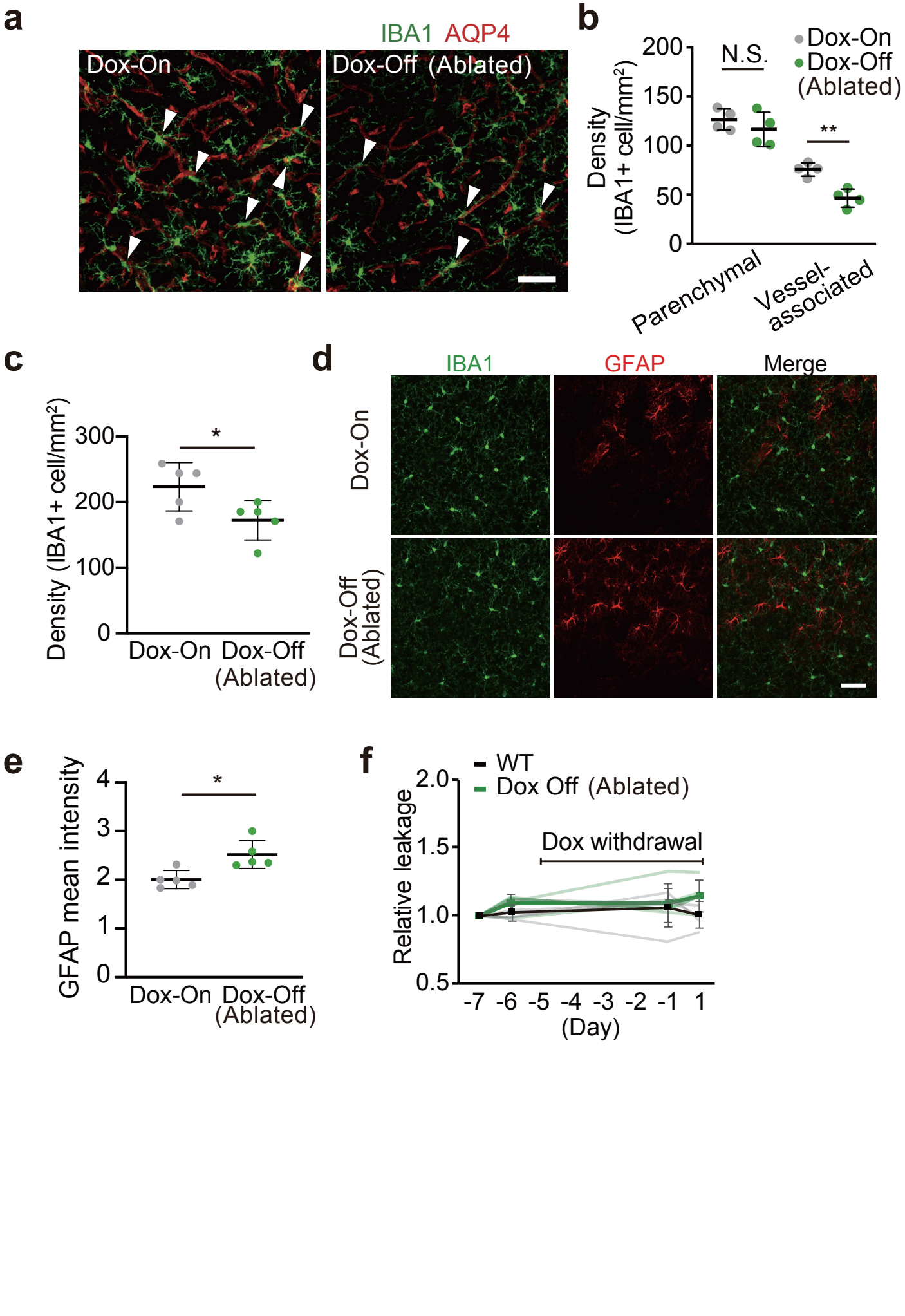
a
IBA1 AQP4
Dox-On
Dox-Off (Ablated)
b
Density (IBA1+ cell/mm²)
200
150
100
50
0
N.S.
**
Dox-On
Dox-Off (Ablated)
Parenchymal
Vessel-associated
c
Density (IBA1+ cell/mm²)
300
200
100
0
*
Dox-On
Dox-Off (Ablated)
d
IBA1
GFAP
Merge
Dox-On
Dox-Off (Ablated)
e
GFAP mean intensity
4
3
2
1
0
*
Dox-On
Dox-Off (Ablated)
f
WT
Dox Off (Ablated)
Dox withdrawal
Relative leakage
2.0
1.5
1.0
0.5
-7 -6 -5 -4 -3 -2 -1 1
(Day)

Figure 13

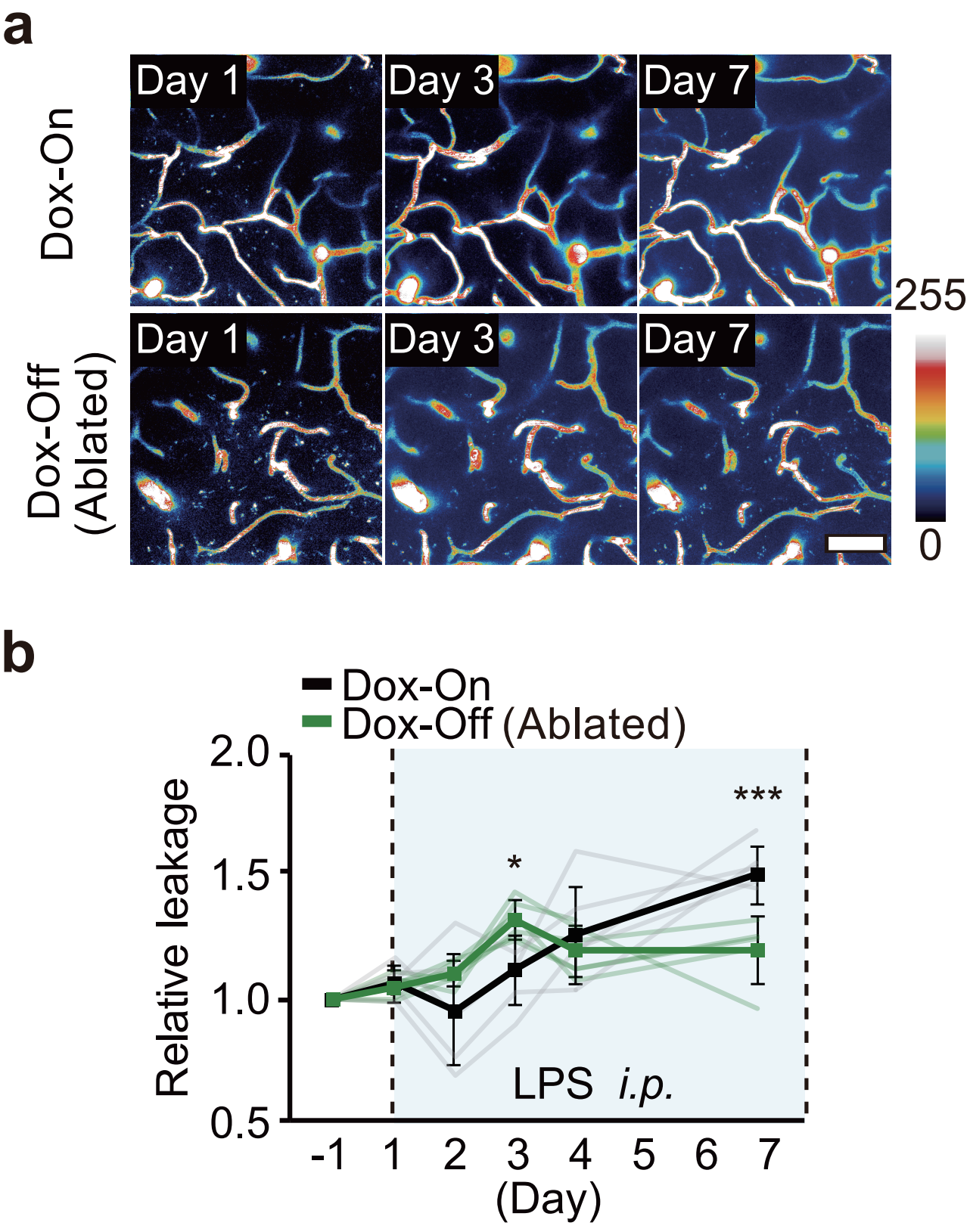
a
Dox-On
Dox-Off (Ablated)
Day 1
Day 3
Day 7
255
0
b
Dox-On
Dox-Off (Ablated)
Relative leakage
2.0
1.5
1.0
0.5
*
***
LPS i.p.
-1 1 2 3 4 5 6 7
(Day)

Figure 14

a

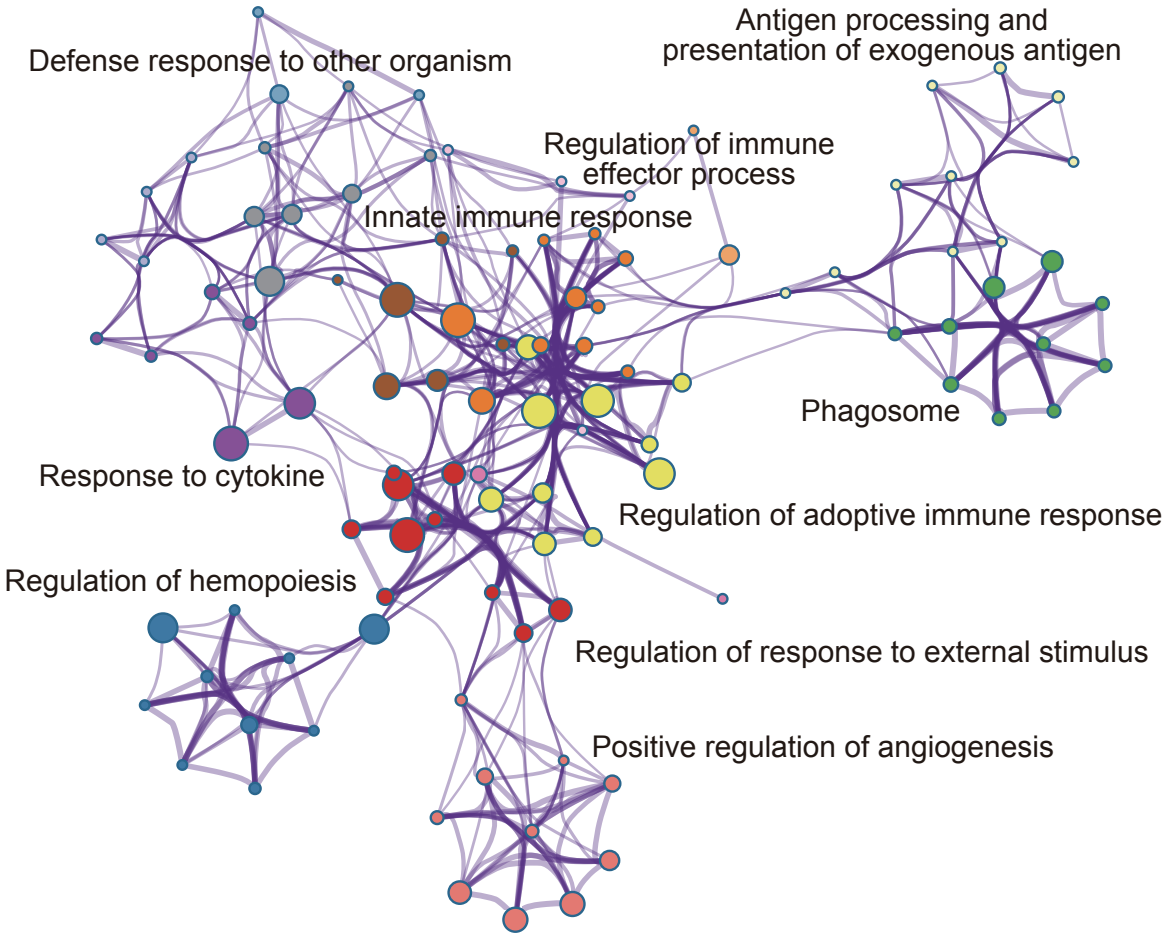

b

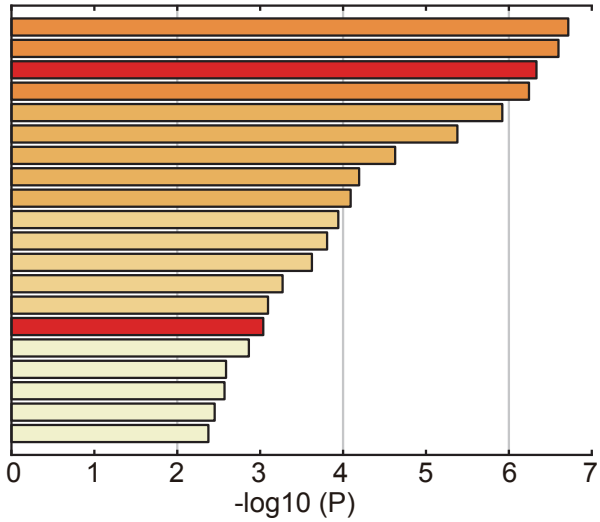

GO:0032101: regulation of response to external stimulus
GO:1903706: regulation of hemopoiesis
ko04145: Phagosome
GO:0034097: response to cytokine
GO:0002697: regulation of immune effector process
GO:0002819: regulation of adaptive immune response
GO:0045087: innate immune response
GO:0002274: myeloid leukocyte activation
GO:0098542: defense response to other organism
GO:0060143: positive regulation of syncytium formation
GO:0019884: antigen processing and presentation of exogenous antigen
GO:0042832: defense response to protozoan
GO:0045766: positive regulation of angiogenesis
GO:0019730: antimicrobial humoral response
R-MMU-198933: Immunoregulatory interactions between a Lymphoid and a non-Lymphoid cell
GO:0007613: memory
GO:0034110: regulation of homotypic cell-cell adhesion
GO:0060419: heart growth
GO:0051346: negative regulation of hydrolase activity
GO:0003333: amino acid transmembrane transport

Figure 15

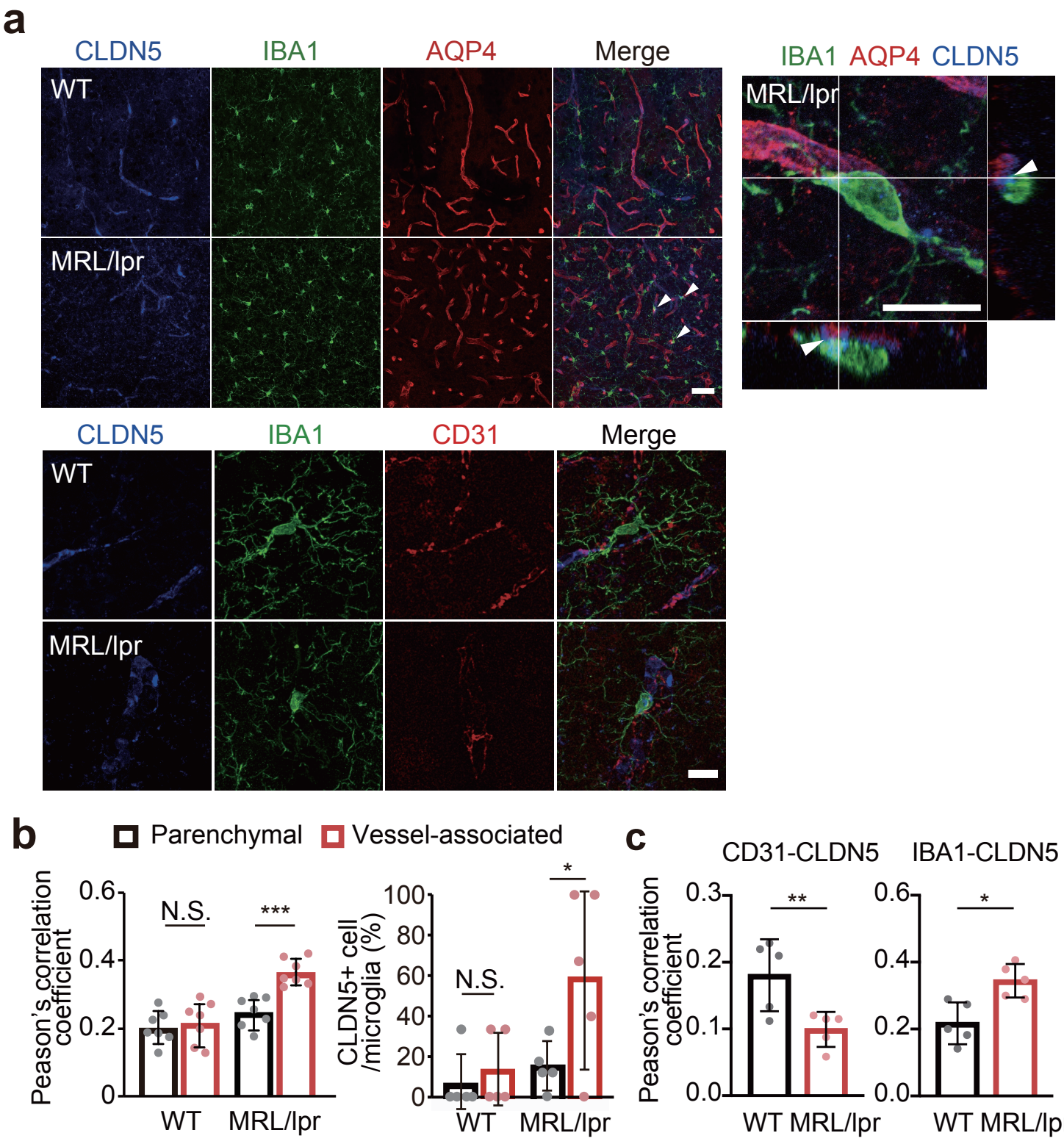
a
CLDN5
IBA1
AQP4
Merge
WT
MRL/lpr
IBA1 AQP4 CLDN5
MRL/lpr
CLDN5
IBA1
CD31
Merge
WT
MRL/lpr
b
Parenchymal
Vessel-associated
Peason's correlation coefficient
0.6
0.4
0.2
0
N.S.
***
WT
MRL/lpr
CLDN5+ cell /microglia (%)
100
80
60
40
20
0
*
N.S.
WT
MRL/lpr
c
CD31-CLDN5
IBA1-CLDN5
Peason's correlation coefficient
0.3
0.2
0.1
0.0
**
WT MRL/lpr
0.6
0.4
0.2
0.0
*
WT MRL/lpr

Figure 16

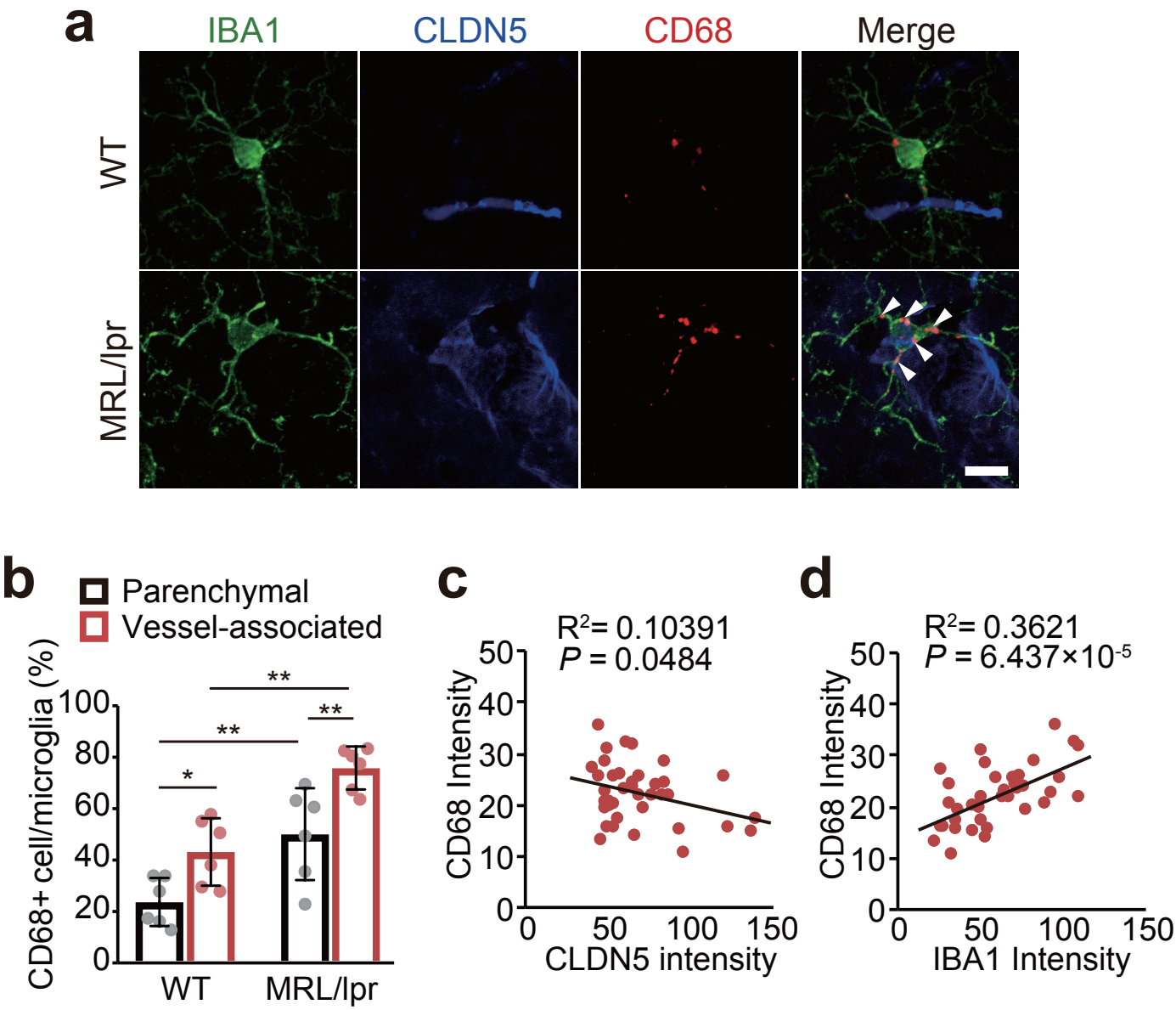
a
IBA1
CLDN5
CD68
Merge
WT
MRL/lpr
b
Parenchymal
Vessel-associated
CD68+ cell/microglia (%)
100
80
60
40
20
0
**
**
**
*
WT
MRL/lpr
c
R²= 0.10391
P = 0.0484
CD68 Intensity
50
40
30
20
10
0
0
50
100
150
CLDN5 intensity
d
R²= 0.3621
P = 6.437×10-5
CD68 Intensity
50
40
30
20
10
0
0
50
100
150
IBA1 Intensity

Figure 17

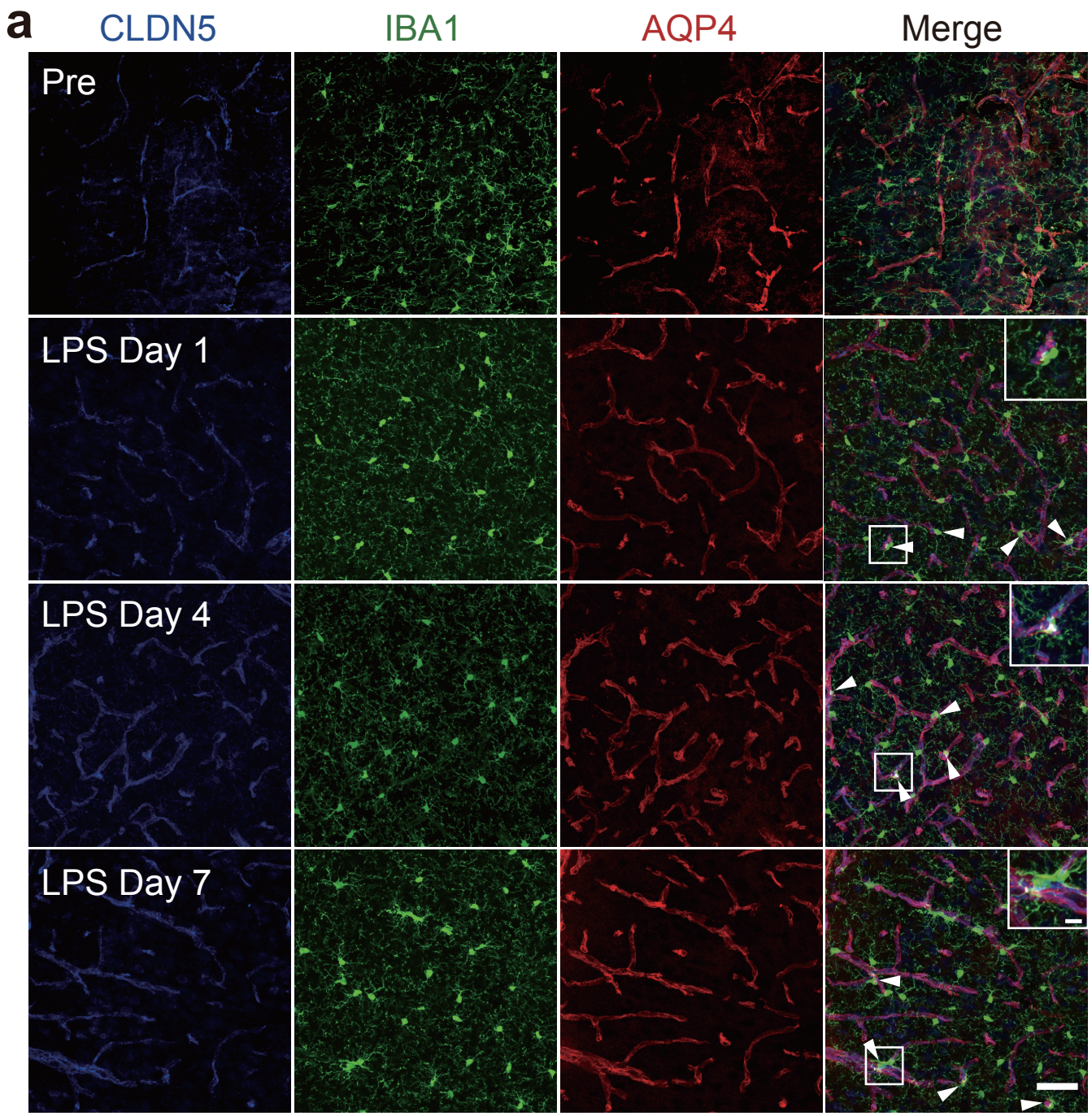
a
CLDN5
IBA1
AQP4
Merge
Pre
LPS Day 1
LPS Day 4
LPS Day 7

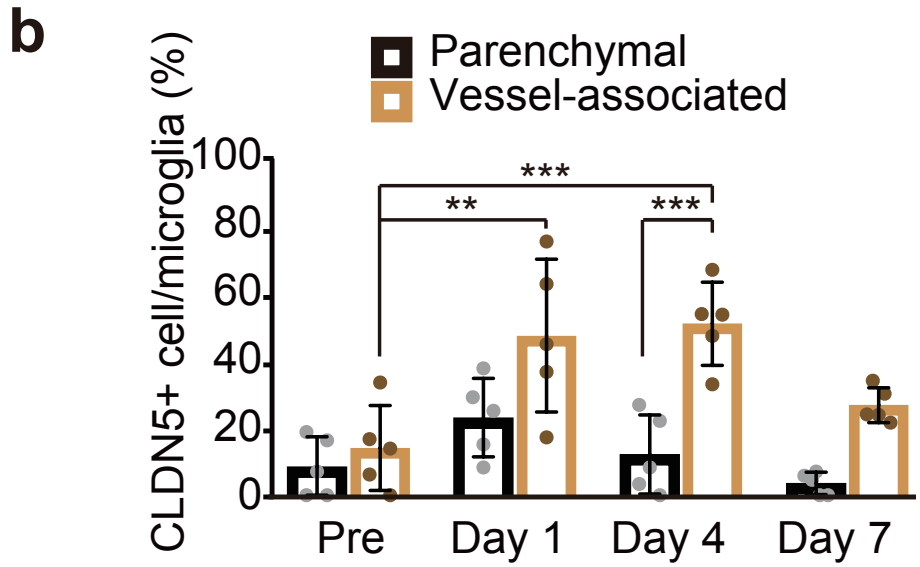
b
Parenchymal
Vessel-associated
CLDN5+ cell/microglia (%)
100
80
60
40
20
0
**
***
***
Pre
Day 1
Day 4
Day 7

Figure 18

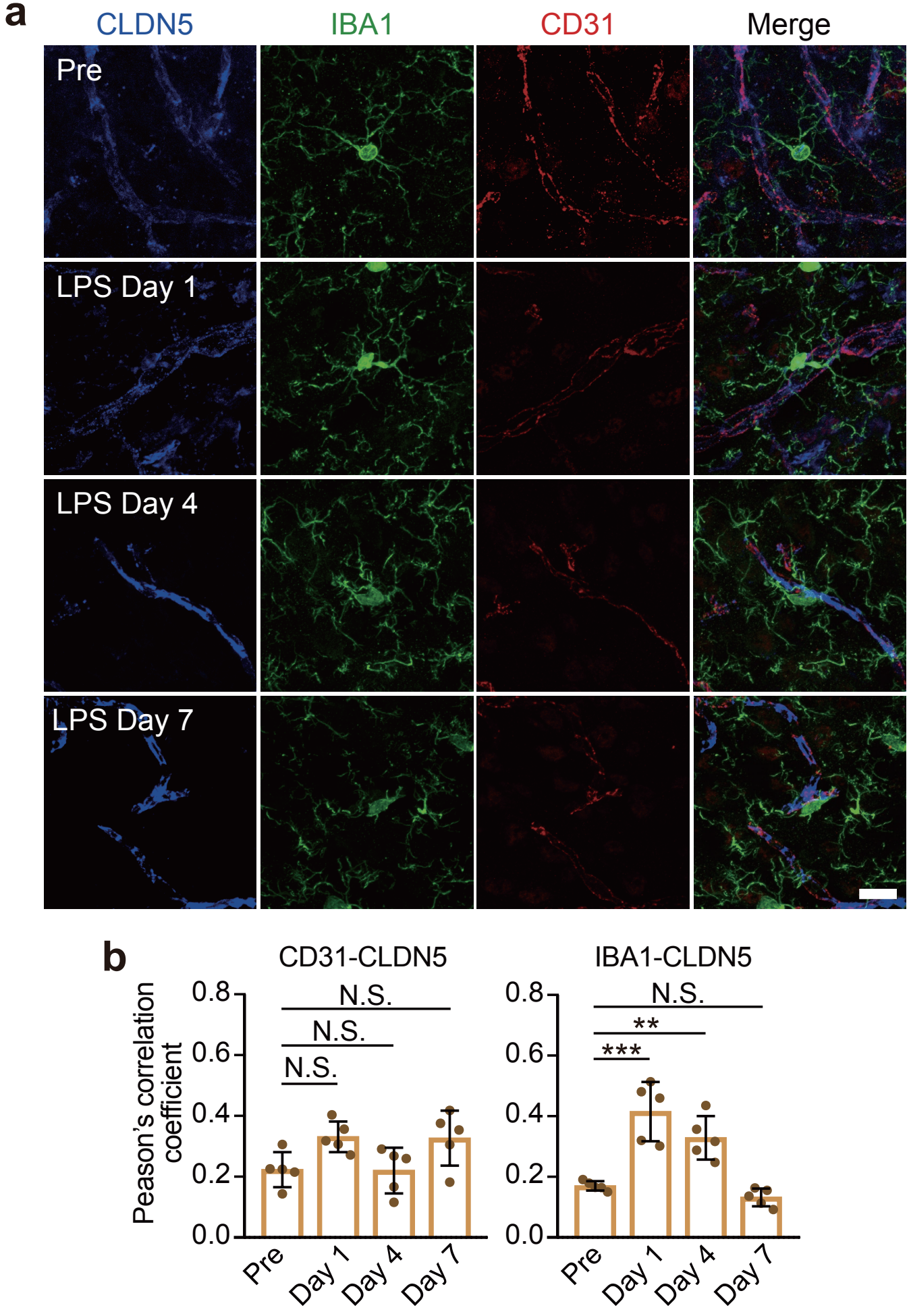
a
CLDN5
IBA1
CD31
Merge
Pre
LPS Day 1
LPS Day 4
LPS Day 7
b
CD31-CLDN5
IBA1-CLDN5
Peason's correlation coefficient
0.8
0.6
0.4
0.2
0.0
N.S.
N.S.
N.S.
**
***
Pre
Day 1
Day 4
Day 7

Figure 19

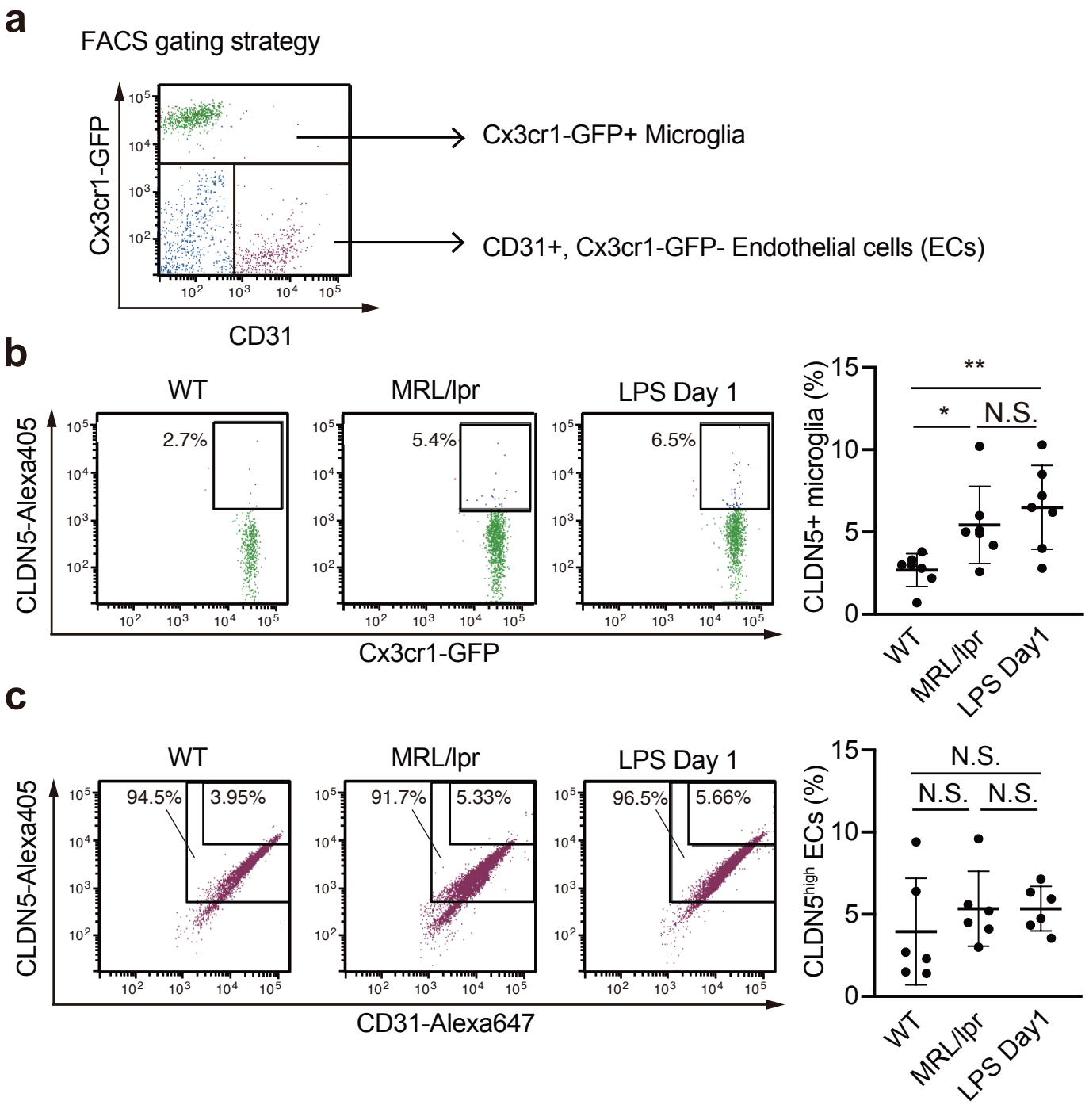
a
FACS gating strategy
Cx3cr1-GFP
CD31
Cx3cr1-GFP+ Microglia
CD31+, Cx3cr1-GFP- Endothelial cells (ECs)
b
WT
MRL/lpr
LPS Day 1
2.7%
5.4%
6.5%
CLDN5-Alexa405
Cx3cr1-GFP
CLDN5+ microglia (%)
**
*
N.S.
c
94.5%
3.95%
91.7%
5.33%
96.5%
5.66%
CD31-Alexa647
CLDN5high ECs (%)
N.S.

Figure 20

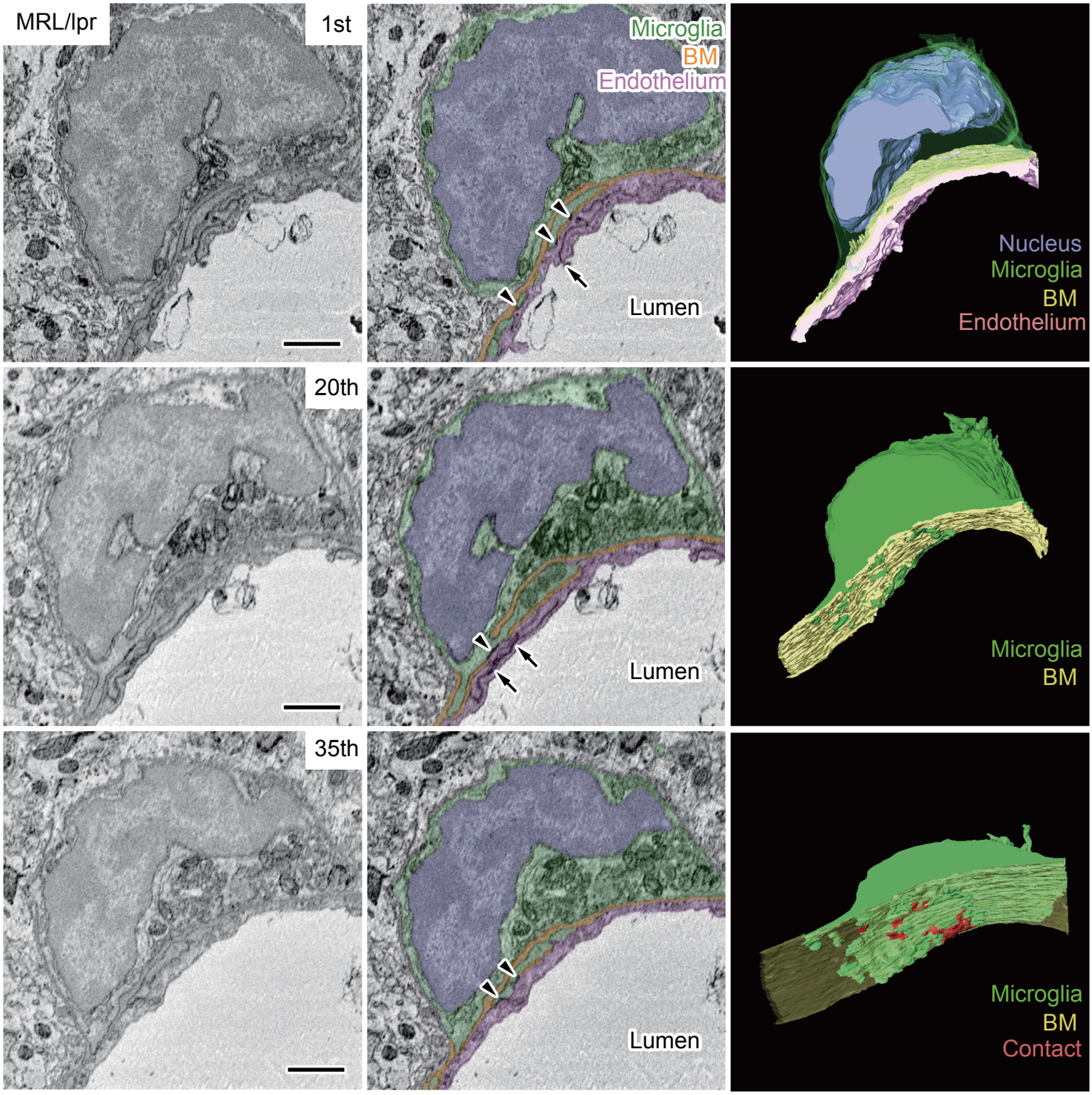
MRL/lpr
1st
Microglia
BM
Endothelium
Lumen
Nucleus
Microglia
BM
Endothelium
20th
Lumen
Microglia
BM
35th
Lumen
Microglia
BM
Contact

Figure 21

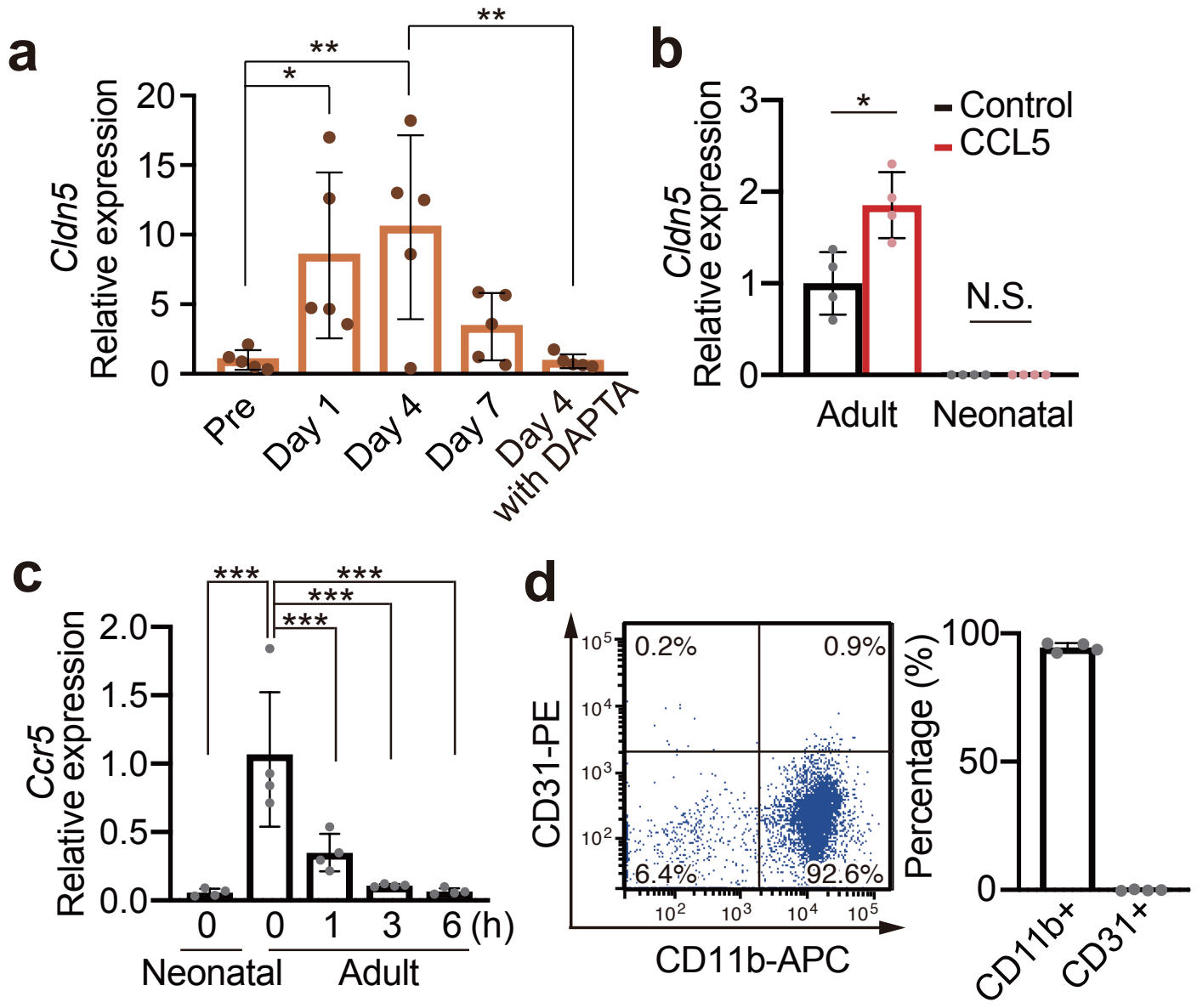
a
Cldn5
Relative expression
20
15
10
5
0
*
**
**
Pre
Day 1
Day 4
Day 7
Day 4
with DAPTA
b
Cldn5
Relative expression
3
2
1
0
*
Control
CCL5
N.S.
Adult
Neonatal
c
Ccr5
Relative expression
2.0
1.5
1.0
0.5
0.0
***
***
***
***
0
0
1
3
6 (h)
Neonatal
Adult
d
CD31-PE
CD11b-APC
0.2%
0.9%
6.4%
92.6%
Percentage (%)
100
50
0
CD11b+
CD31+

Figure 22

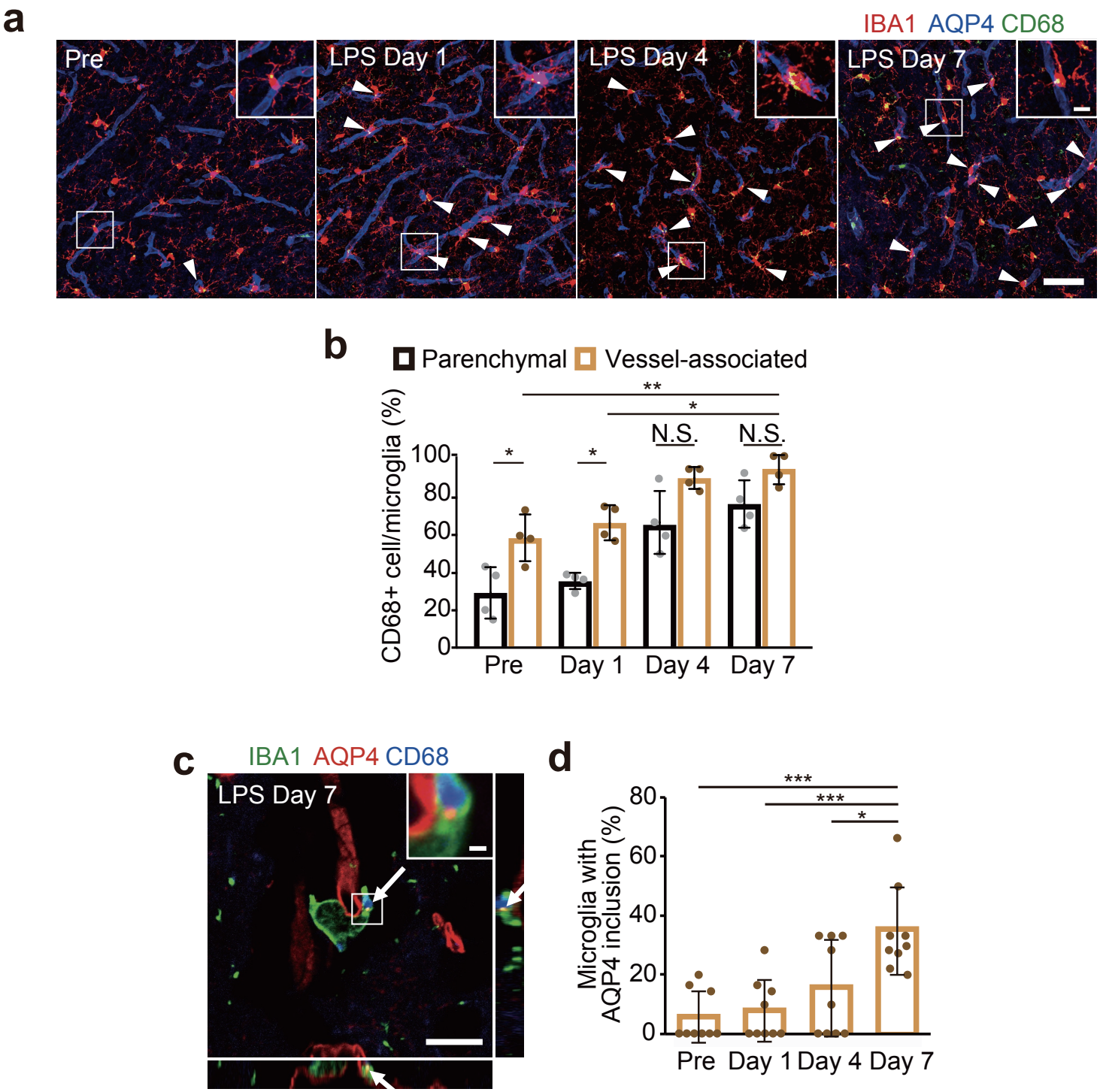
a
IBA1 AQP4 CD68
Pre
LPS Day 1
LPS Day 4
LPS Day 7
b
Parenchymal
Vessel-associated
CD68+ cell/microglia (%)
100
80
60
40
20
0
**
*
N.S.
N.S.
*
*
Pre
Day 1
Day 4
Day 7
c
IBA1 AQP4 CD68
LPS Day 7
d
Microglia with AQP4 inclusion (%)
80
60
40
20
0
***
***
*
Pre
Day 1
Day 4
Day 7

Figure 23

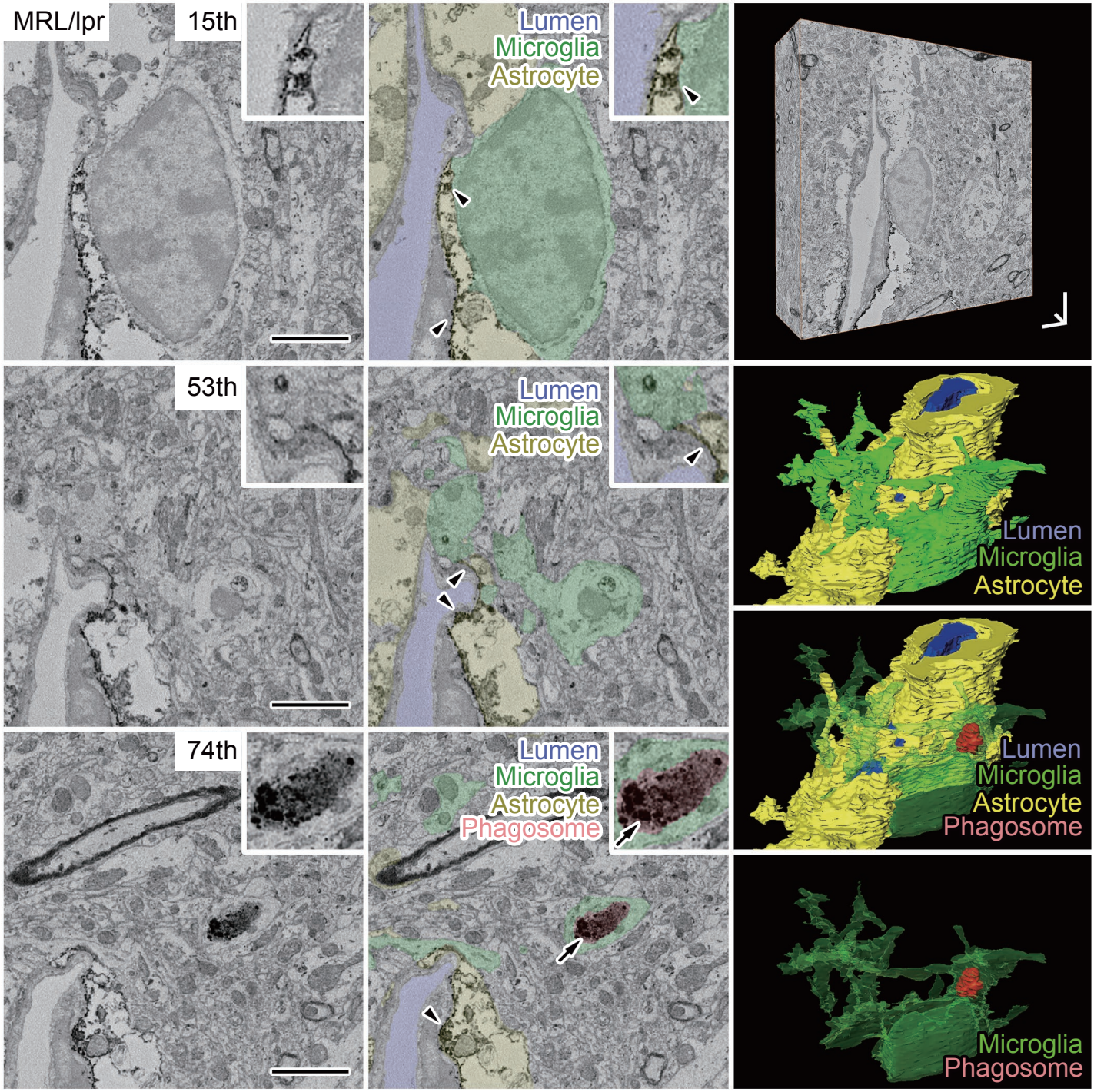
MRL/lpr
15th
Lumen
Microglia
Astrocyte
53th
Lumen
Microglia
Astrocyte
Lumen
Microglia
Astrocyte
74th
Lumen
Microglia
Astrocyte
Phagosome
Lumen
Microglia
Astrocyte
Phagosome
Microglia
Phagosome

Figure 24

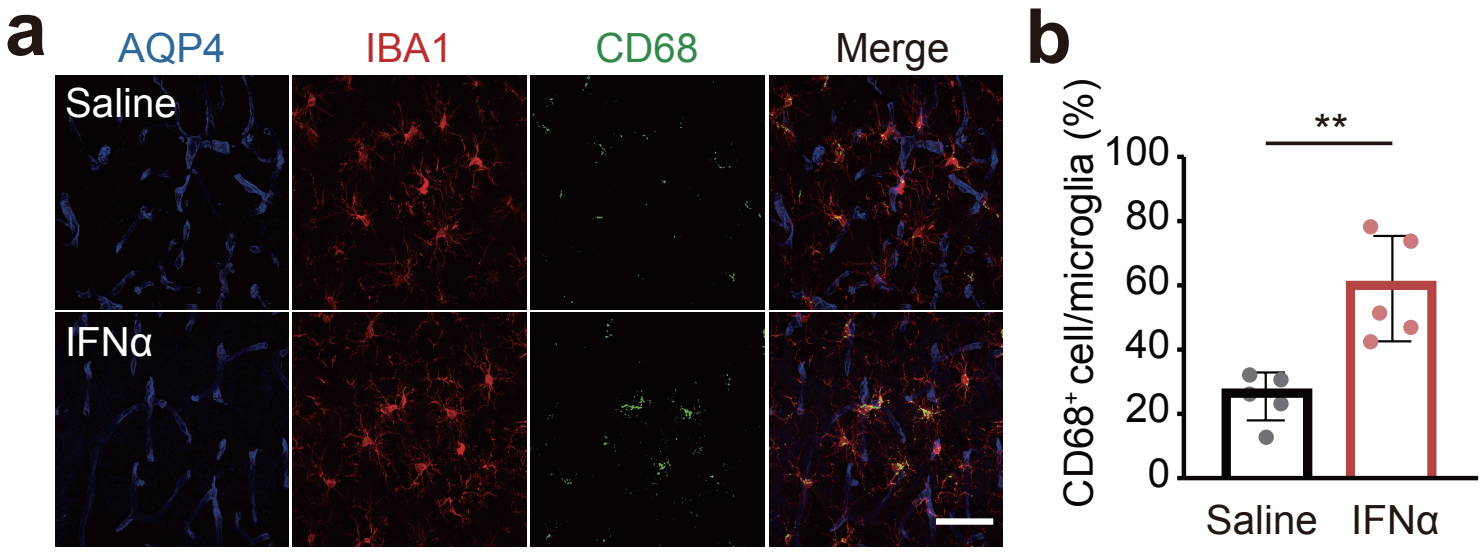
a
AQP4
IBA1
CD68
Merge
Saline
IFNα
b
CD68+ cell/microglia (%)
100
80
60
40
20
0
**
Saline
IFNα

Figure 25

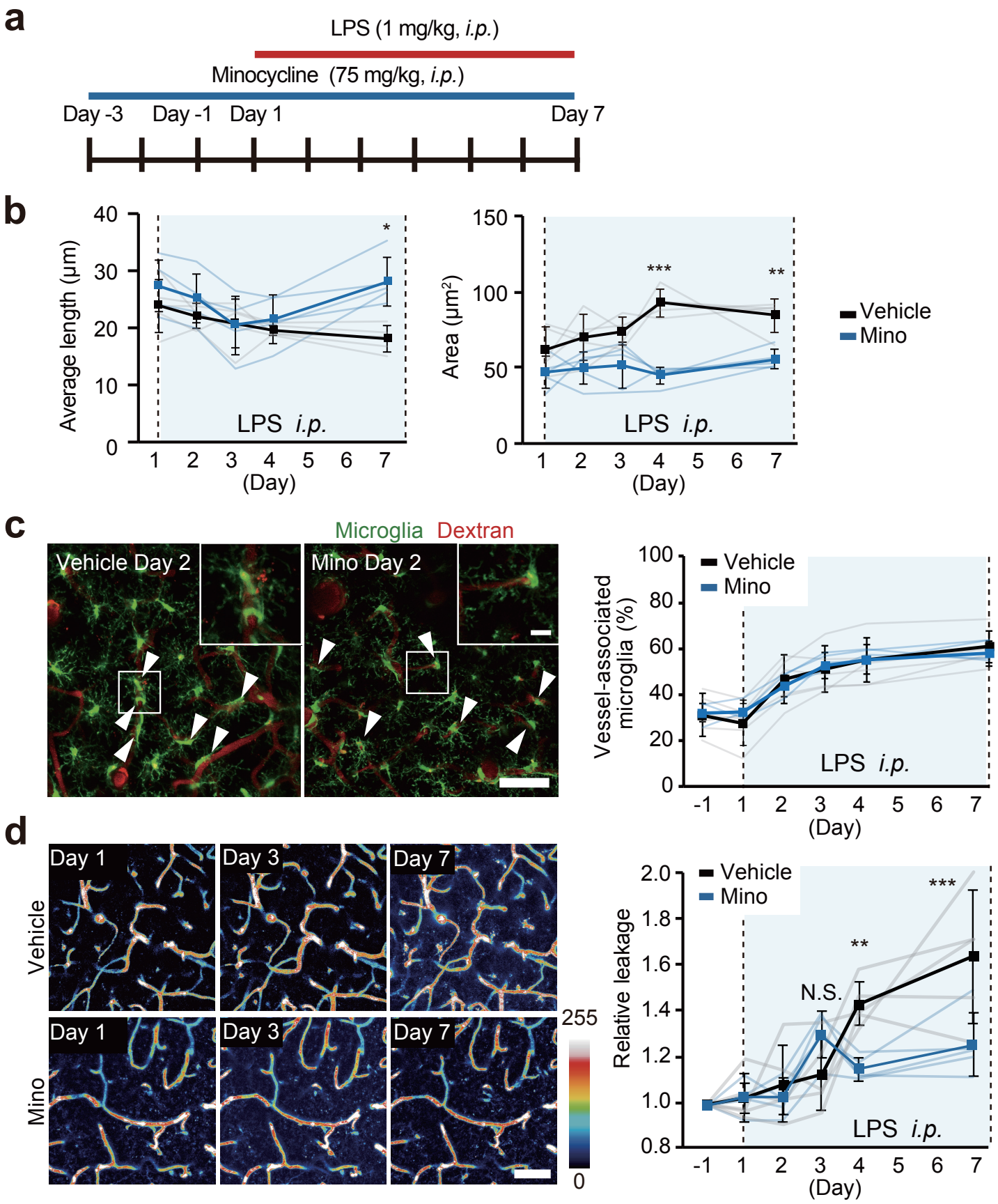
a
LPS (1 mg/kg, i.p.)
Minocycline (75 mg/kg, i.p.)
Day -3
Day -1
Day 1
Day 7
b
Average length (μm)
LPS i.p.
(Day)
Area (μm²)
Vehicle
Mino
c
Microglia Dextran
Vehicle Day 2
Mino Day 2
Vessel-associated microglia (%)
d
Day 1
Day 3
Day 7
Vehicle
Mino
255
0
Relative leakage
N.S.

Figure 26

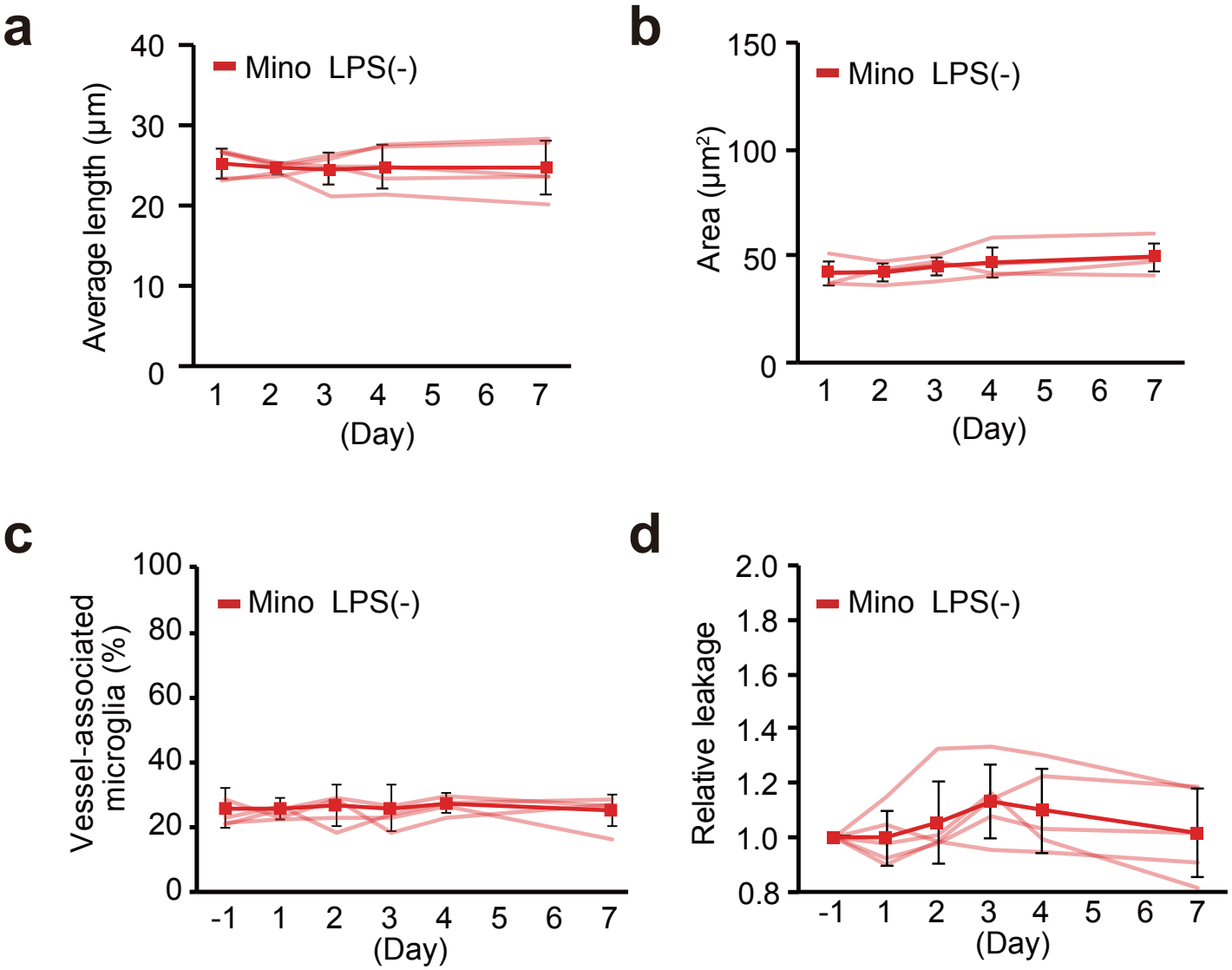
a
Mino LPS(-)
Average length (μm)
40
30
20
10
0
1 2 3 4 5 6 7
(Day)
b
Mino LPS(-)
Area (μm²)
150
100
50
0
1 2 3 4 5 6 7
(Day)
c
Mino LPS(-)
Vessel-associated microglia (%)
100
80
60
40
20
0
-1 1 2 3 4 5 6 7
(Day)
d
Mino LPS(-)
Relative leakage
2.0
1.8
1.6
1.4
1.2
1.0
0.8
-1 1 2 3 4 5 6 7
(Day)